UNIVERSITY OF Southampton

University of Southampton Research Repository

Copyright © and Moral Rights for this thesis and, where applicable, any accompanying data are retained by the author and/or other copyright owners. A copy can be downloaded for personal non-commercial research or study, without prior permission or charge. This thesis and the accompanying data cannot be reproduced or quoted extensively from without first obtaining permission in writing from the copyright holder/s. The content of the thesis and accompanying research data (where applicable) must not be changed in any way or sold commercially in any format or medium without the formal permission of the copyright holder/s.

When referring to this thesis and any accompanying data, full bibliographic details must be given, e.g.

Thesis: Author (Year of Submission) "Full thesis title", University of Southampton, name of the University Faculty or School or Department, PhD Thesis, pagination.

Data: Author (Year) Title. URI [dataset]

University of Southampton
Faculty of Engineering and Physical Sciences
School of Engineering

Realistic Ship Models for Experimental Investigation

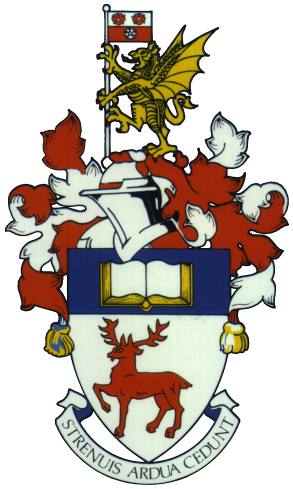

by
Apostolos Grammatikopoulos
ORCID ID 0000-0003-1800-7406

A Thesis submitted for the degree of
Doctor of Philosophy

October 2019

Abstract

After several decades of hydroelastic experiments, scaled ship models are still predominantly constructed with a simplified structure. A rigid vessel is divided into segments and the flexibility is provided by a backbone or a series of flexible joints, usually with a uniform stiffness distribution. Although continuous models have been used, there are no documented cases of a model with an internal structure resembling a ship, a so-called elastic model.

In the present investigation, 3D printing is proposed as a manufacturing method to produce elastic models and the associated advantages and constraints are investigated. Design of a 3D printed elastic ship model is found to be challenging, partly because of the lack of material properties available and the inadequacy of traditional methods, such as 3-point bending tests, to determine the properties relevant to structural vibration. A method based on cellular specimens subjected to modal testing combined with FEA simulations is developed to accurately predict the natural frequencies of the model during the design stage, as well as estimate structural damping.

A 3D printed elastic model of a ship is designed and manufactured and its vibratory performance in air and water is investigated. It is demonstrated that the natural frequencies of the vessel can be accurately predicted using the newly-developed specimen method mentioned above. A step-by-step procedure for the design and production of 3D printed elastic models of ships is developed.

Bending moment measurements on the model in head waves and the corresponding strain distribution within the cross section indicate beam-like behaviour and agree with existing theory and literature, thus verifying the concept of a 3D printed elastic ship model. Additionally, locally increased stiffness due to the tow post attachment demonstrates the capability of the model to capture local responses, which are absent in segmented models.

The methodology developed here will allow investigators to introduce a more accurate representation, in model scale, of a ship's cross-sectional properties, such as torsional stiffness distribution and shear centre location. Results from such investigations are crucial for the improvement of state-of-the-art hydroelastic codes and, consequently, assessment of ship safety.

Contents

List of Figures

List of Tables

Acknowledgements

The present investigation was funded by the Lloyd's Register Foundation University Technology Centre on Ship Design for Enhanced Environmental Performance. Further financial support was provided by the EPSRC Doctoral Training grant.

Throughout my PhD there were a number of people whose support was critical to the success of this project. I would like to start by thanking my supervisors, Professor Pandeli Temarel and Dr Joseph Banks for their continuous and invaluable contribution, both in terms of scientific expertise and general mentoring.

Furthermore, I would like to thank my colleagues from Fluid-structure Interactions research group in the University of Southampton for repeatedly assisting me with experiments, when an additional pair of hands would make a significant difference. A special mention has to be made for Mehmet Cihan, as he would always make himself available when necessary and eventually devoted several hours to my experiments.

As importantly, I would like to thank my colleagues for the great social environment that Fluid-structure interactions has become. This is the result of contributions by current and former members and has resulted in a group that offers immense support during the pursuit of a doctoral degree. This support ranged from interesting discussions during coffee breaks to frequent social activities to form deeper bonds between members and informal seminars to exchange ideas and receive constructive feedback. It surely made the journey much more creative and exciting than it would have been otherwise.

Finally, I would like to thank the late Sir Terry Pratchett. During my PhD candidature I read twenty novels from the *Discworld* series, from *Equal Rites* to The *Last Continent*, having previously read the first two books of the series. It would be no exaggeration to say that the company these books provided was of crucial importance, allowing me to vent overwhelming pressure and to avoid losing too many sanity points in the process.

Chapter 1

Introduction

1.1 Overview and research challenges

Economic developments on a global scale led to the construction of increasingly long and slender container ships. The geometry of these ships resulted in a shift of the lower structural natural frequencies of the hull-girder towards the high energy content part of the wave spectrum. The resulting springing and whipping (the latter also observed in high speed craft) were found to cause significant global loading on the structure. *Springing* is a harmonic structural response caused by waves, whereas *whipping* is a transient structural response caused by slamming. The above phenomena may only be investigated by coupling the hydrodynamic loads with the structural response, either numerically or experimentally, namely hydroelasticity.

It is common practice when designing a model for hydroelastic experiments to produce it in rigid segments, to be joined with use of a flexible backbone [1] or a series of flexible joints [2]. In either case, the bending stiffness and, in few cases, stiffness distribution [3] are scaled. Appropriate scaling of the mass distribution, in conjunction with the above, ensures correct scaling of at least the 2-node vertical bending natural frequency. Scaling of higher-order natural frequencies, even when just examining vertical bending, is not possible without use of a distributed stiffness.

These models are able to provide information concerning the global structural response in a wide range of sea conditions. However, backbones are manufactured with a very simplified cross section (often just a box-shaped extrusion) when compared to that of a ship.As a result, the shear flow and consequential shear stresses are not appropriately scaled. This affects symmetric (vertical bending) responses to some extent, through the calculation of the effective shear area. More importantly, antisymmetric responses are affected significantly by the torsional stiffness distribution and shear centre location (which ensures appropriate coupling between horizon-

tal bending and twisting). Emulating these aspects on a scaled model is particularly challenging, with researchers resorting to overly complicated design and manufacturing procedures for the relevant backbones (despite the simplification of the cross-section). When flexible joints are used, the stiffness is, in fact, entirely artificial and lacks the beam qualities of a backbone, resembling a spring-mass system.

In pursuit of more detailed structural response, some researchers designed continuous models with a structure resembling a ship [4], the so-called *elastic models*. Use of elastic models is essential for the experiments to follow the significant progress of computations and be fully useful for validation. Such models would ensure that the vessel serves its dual role as a hydrodynamic boundary and a load-bearing structure and, in fact, one with an arrangement resembling the full-scale vessel. However, the production cost of such models and the inability to modify them after construction discouraged their extensive use by the scientific community. Among the 27 flexible vessels from past investigations discussed within this report, only 3 were elastic models (Table A.1).

Furthermore, limitations of manufacturing technologies had profound effects in these attempts. The external ship surface would be produced as a single skin and a series of transverse bulkheads would be included to withstand hydrostatic pressure and avoid significant deflections due to local loads. Internal decks, longitudinal stiffeners and other elements of the structure contributing to the bending stiffness and rendering the cross-section more realistic could not be manufactured without overcomplicating the production process and would be omitted [5]. Consequently, the concept has not been explicitly proven.

3D printing is an additive manufacturing technology and is capable of producing complex structures in an efficient manner. Although this technology could potentially facilitate the production of elastic models, such a venture has not been attempted before and there are several challenges to overcome. As will be discussed in more detail later, the bending stiffness requirements for specific cross sections limit the suitable material range significantly. The structure should be watertight although 3D printed parts are by nature porous/cellular and the inherent orthotropic properties of the material should not affect the dynamic response.

The exact properties of most 3D printed materials are uncertain. Manufacturers' specifications often regard pre-fabrication properties and are usually obtained through tensile tests, whereas flexular properties are the ones relevant to this investigation. Extensive tests are necessary to verify the compatibility of a material with a specific model design. Structural damping is also difficult to predict and is usually measured during dynamic tests of the finished structure.

1.2 Research aim and objectives

The aim of this project is to investigate the use of 3D printing for the production of detailed elastic models of ships. The above includes the suitability of the technology for the production of a scaled, detailed model of a ship structure and the potential of this model to emulate the ship's behaviour more appropriately than a backbone model. The project's objectives are outlined below:

1. To investigate the mechanical properties of 3D printed components
2. To combine the above findings with model scaling techniques and a joining procedure to manufacture an elastic model from 3D printed sections.
3. To perform modal testing of the vessel, approximating a free support condition in vacuo and in water and determine its modal properties.
4. To carry out towing tank tests and determine the vessel responses in regular head waves.
5. To compare the towing tank results to 2D hydroelasticity predictions, acting as an equivalent backbone model, for validation purposes.
6. To develop a standardised design procedure for 3D printed hydroelastic models of ships.
7. To assess the suitability of 3D printed elastic ships models for investigation of antisymmetric vibrations.

1.3 Terminology

Due to the various forms of 3D printed components within this project, it is important to define particular terms that will be used throughout the report.

- *Coupon* refers to a 3D printed rectangular block, used for 3-point bending tests and with dimensions as prescribed by the relevant ISO standard (see Chapters 4 and 5)
- *Specimen* refers to a component with a constant, cellular (box-shaped) cross section and with dimensions as decided to suit the purposes of the investigation (see Chapter 5).
- *Model/vessel* is used for the 3D printed elastic ship model, which is the primary focus of the investigation (also referred to as barge or rectangular barge)

- *Section* is used for the pieces in which the model geometry had to be split during design to fit in the 3D printer and subsequently joined to form the model (not to be confused with *segments* of segmented models).

1.4 Novelty

This project introduces the following novel aspects to hydroelastic testing of ships:

- the design and production of the first 3D printed elastic model with a detailed internal structure resembling a ship
- the testing of that model in head waves, demonstrating its global performance according to theory and, consequently, its behaviour as a ship structure and also its ability to capture local responses, unlike a segmented model
- the development of a method, based on specimen modal testing and FEA simulations, to accurately predict the vibratory properties of a 3D printed elastic model
- the compilation of a step-by-step procedure for the design and production of 3D printed elastic ship models
- a demonstration of the potential of such a model to be used for measurement of antisymmetric responses, where its cross-sectional characteristics would become particularly relevant

1.5 Advancements in additive manufacturing

Additive manufacturing has evolved significantly since the beginning of this project. The relevant equipment today allows for smaller thickness and improved dimensional accuracy to be achieved compared to what is described within this document. The above would facilitate the design procedure to achieve the desired cross-sectional characteristics, particularly considering the constantly expanding material range. Consequently, the choices of thickness and material used for the specimens and model should be considered with the then state-of-the-art in mind. However, the present investigation and the design methodology developed herein is structured in a general manner which allows it to remain relevant and useful regardless of such advancements.

1.6 Report structure

Following the introduction to the project given in this chapter, Chapter 2 begins with design considerations for scaled models and then presents techniques used for hydroelastic experiments, from investigations published by pioneers of the practice to current state-of-the-art. A categorisation based on the focus of the investigation is used. Trends on model design and the reasons behind them are also analysed.

In Chapter 3, the reader is introduced to 3D printing and the proposed manufacturing process. A presentation of the parametric dependence of 3D printed parts' mechanical properties is followed by brief discussion of joining techniques.

Chapter 4 refers to the vessels considered for modelling and the relevant challenges, often limiting the available range of options are presented. The material properties uncertainty is addressed by a series of mechanical tests. The final vessel design and production process are presented, including a discussion of geometric uncertainties.

Chapter 5 starts by presenting considerations regarding the under-predicted natural frequency of the vessel. A specimen-scale testing methodology is introduced, to be incorporated and complement the design procedure. Results from quasi-static and dynamic tests are correlated to both beam and shell models. The flexural modulus from dynamic tests is used to calculate the natural frequencies of the vessel and these predictions are compared to experimental measurements. Structural damping of specimens is compared to that of the model.

In Chapter 6, the static loading, dry testing and wet testing of the vessel are presented. The measurements in waves are compared to 2D hydroelasticity results. Structural damping and higher-order harmonic responses are discussed.

Chapter 7 outlines a design procedure, including specimen testing, for elastic models of ships, to be used by future investigators.

Chapter 8 serves as a summary of the findings and discussion of their significance and offers suggestions for future work.

Finally, a number of appendices are included at the end of the thesis, mostly for large tables and figures. The only exception is Appendix G, which includes all the publications produced within this project until thesis submission.

Chapter 2

Background to physical hydroelastic modelling

2.1 Overview

Flexible structural models have been used extensively for the investigation of dynamic responses since the end of World War II [6, 7]. Rigid ship models, used in towing tank tests, have an even longer history, beginning at the time of William Froude. Even though computational techniques were first established in the 1970s and have progressed significantly since then, the concept of model experiments still constitutes an essential part of the scientific method. Despite the uncertainties caused by scaling effects, physical models are often considered the most credible method of investigation and are used for validation of theoretical and numerical models.

2.2 Model design, scaling laws and similarity

When designing a physical model, the scaling laws play a key role by establishing which non-dimensional groups of quantities are relevant to the specific experiment. In the case of flexible models, the aforementioned laws do not only concern the geometry but also extend to the structural properties. As the material of the model may vary significantly from that of the full-scale structure for practical reasons, it is essential that a thorough investigation of the mechanical characteristics of both is performed.

The Buckingham Pi theorem is considered the cornerstone of dimensional analysis and physical modelling. With its help, a set of dimensional parameters describing the original system may be substituted by a set of non-dimensional numbers. The latter set is always smaller in size than the former, reduced by the number of independent dimensions involved. Depending on the problem investigated, either the so-called absolute (mass-

Table 2.1: Dimensionless numbers commonly used in fluid dynamics

Symbol	Full name	Physical meaning	Formula
F_N	Froude number	$\frac{Inertia forces}{Gravity forces}$	$\frac{U}{\sqrt{gL}}$
Re	Reynolds number	$\frac{Inertia forces}{Viscous forces}$	$\frac{UL}{\sqrt{\nu}}$
W_n	Weber number	$\frac{Inertia forces}{Surface tension forces}$	$\frac{U}{\sqrt{\sigma/\rho L}}$
Cy	Cauchy number	$\frac{Inertia forces}{Elastic forces}$	$\frac{\rho U^2}{E}$
St	Strouhal number	Dimensionless vortex-shedding frequency	$\frac{f_v D}{U}$
KC	Keulegan-Carpenter number	Period parameter	$\frac{UT}{D}$
Ur	Ursell number	Depth parameter	$\frac{H_w \lambda^2}{d^3}$

length-time, MLT) or the engineering (force-length-time FLT) system is employed to define the independent dimensions [8]. The set of dimensionless numbers is selected in such way that they may be interpreted physically and, at the same time, their interpretation is relevant to the problem at hand. Consequently, the experimental findings, expressed as functions of the dimensionless quantities, aid in the depiction of potential correlations. Non-dimensionalising the experimental parameters greatly facilitates the scaling process. More detailed description of the Pi theorem procedure may be easily found in the relevant literature [8, 9].

2.2.1 Similarity and fluid-structure interactions

The dimensionless numbers obtained with the Pi theorem are ratios between similar quantities and are used to satisfy the three similarity conditions. Geometrical similarity is achieved by scaling all dimensions of the structure and environment using a common ratio, usually symbolised by λ. Kinematic similarity is satisfied by, similarly, scaling all velocities. Finally, dynamic similarity regards scaling of the forces on the model. As various combinations of force sources may be used to derive the ratio to be common between full-scale and model-scale, the selection depends on the phenomena investigated. A list of numbers commonly used in fluid-structure interactions may be found in Table 2.1.

In the case of experiments in the towing tank, the so-called Froude scaling is used. Froude scaling involves uniform scaling of all model and wave dimensions, thus satisfying geometric similarity. Any part of the structure that may come in contact with the water should be accurately scaled. It should be noted that "dimensions" may include any quantity measured in L^n, where L stands for length units. For example, the longitudinal centre of gravity or the metacentric height would be scaled by λ, whereas the submerged volume of the vessel would then be equal to:

$$\nabla_M = \frac{\nabla_F}{\lambda^3} \tag{2.1}$$

The mass may be consequently calculated as:

$$m_M = \frac{\rho_M}{\rho_F}\frac{m_F}{\lambda^3} \tag{2.2}$$

where ρ_M, ρ_F is the density of water in model-scale and full-scale, respectively. This means that the mass is scaled in proportion to the cube of the similarity ratio only if water in the towing tank has the same density as the one surrounding the full-scale vessel. However, the ρ_M/ρ_F ratio is approximately equal to unity and may be neglected when performing initial scaling estimations. It may be similarly proven that any second moment of area is scaled in proportion to the fourth and the mass moment of inertia in proportion to the fifth power of the similarity ratio.

Waves in the towing tank are considered gravity waves and their frequency may be calculated by the equation:

$$\omega = \sqrt{\frac{2\pi g}{\lambda_w}} \tag{2.3}$$

where λ_w is the wave length. It follows that wave frequency in model scale is increased in proportion to the square root of the similarity ratio, whereas any time quantities are reduced in proportion to the same number.

A constant Froude number between full-scale and model-scale vessel ensures not only kinematic but also dynamic similarity, as the ratio of inertia forces over gravity forces results in a correct scaling of gravity waves. Creating Froude-similar models means that velocity is scaled down in proportion to the square root of the similarity ratio. Although Reynolds similarity (i.e. ratio of inertia forces over viscous forces) would also be desirable, it may be easily proven that satisfying both relationships is impossible [10]. As viscous forces are relatively small in most cases of ship motions, Reynolds similarity may be abandoned and turbulence inducers may be used to simulate turbulence at a pre-calculated transition point instead.

2.2.2 Hydroelastic structural scaling

The beam mathematical model is often used to simulate the behaviour of a ship, where the boundary conditions are selected as free in both ends. As a consequence, the normal stress in a cross-section when the ship is subjected to a combination of vertical bending and axial loads may be expressed as:

$$\sigma \propto \left(\frac{F_x}{A} + \frac{M_{yy}z}{I_{yy}}\right) \tag{2.4}$$

where F_x and A denote the axial force and cross-sectional area and M_{yy}, z and I_{yy} represent the vertical bending moment, distance from the neutral axis and second moment of area, respectively. As discussed earlier, the distance scales linearly, the area scales as λ^2, the force scales as λ^3 and M_{yy} and I_{yy} scale as λ^4. Substituting to 2.4, we obtain:

$$\sigma_F = \lambda \sigma_M \tag{2.5}$$

In order to maintain geometric similarity, all displacements should scale accordingly. As a result, strains should be the same for full-scale and model scale ship. Considering that the fibre stress may be also be expressed as:

$$\sigma \propto E\epsilon \tag{2.6}$$

where E is the modulus of elasticity and ϵ is the relevant strain. Combining 2.5 and 2.6 we obtain:

$$E_F = \lambda E_M \tag{2.7}$$

which means that the elastic modulus of the material used for the model should scale linearly as well.

As the above is very restrictive, complete similarity is rarely achieved in physical modelling and simplifications are often employed. When *first-order similarity* is used, some scaling laws are ignored as not relevant to the condition simulated. They may regard boundary conditions, geometry, or material used. The selection of pertinent scaling laws is based on the characterisation of the loading condition as axial, bending, shear, torsion or any combination of the four [8].

Axial loads on a ship may be considered negligible compared to bending loads and a pure bending approximation may be assumed. Consequently, scaling of the cross-sectional area becomes less important and scaling of the bending stiffness becomes, in turn, essential. It may be easily derived that:

$$\left(\frac{M_{yy}z}{EI_{yy}}\right)_F = \left(\frac{M_{yy}z}{EI_{yy}}\right)_M \tag{2.8}$$

which means that:

$$\Big(EI_{yy}\Big)_F = \lambda^5 \Big(EI_{yy}\Big)_M \tag{2.9}$$

For a uniform Euler beam [11], the rth natural frequency in vertical bending may be calculated as:

$$\omega_r = \frac{(\kappa L)_r^2}{L^2}\sqrt{\frac{EI}{\mu}} \tag{2.10}$$

where μ is the mass per unit length, L is the length of the vessel and $(\kappa L)_r$ for a free-free beam are the solutions of

$$\cosh \kappa L \cos \kappa L = 1 \tag{2.11}$$

For the full scale vessel, 2.10 becomes:

$$(\omega_r)_F = \frac{(\kappa L_M)_r^2}{\lambda^2 L_M^2} \sqrt{\frac{\lambda^5 (EI)_M}{\lambda^2 \mu_M}} \Longleftrightarrow (\omega_r)_F = \lambda^{-\frac{1}{2}} (\omega_r)_M \tag{2.12}$$

which means that uniform strains between model scale and full scale are a necessary and sufficient condition for appropriate scaling of the bending natural frequencies.

Scaling of the dry natural frequencies depending only on the bending stiffness distribution (and mass distribution) means that the elastic modulus and second moment of area distribution do not need to be scaled separately. Based on this principle, the design process is greatly facilitated by depicting the stiffness in a simplified manner, often without the existence of a structural cross-section (flexible joint models).

2.2.3 Material selection for structural models

The design principles for structural models, as the ones traditionally used, for example, by civil engineers, can differ from the ones related to hydroelastic models. The reason is that, for experiments where the excitation does not result from fluid-structure interaction, several design problems are eliminated (e.g. watertight structure, scaling of flow behaviour etc.). Scaling law implementation is thus greatly facilitated, as it mainly involves geometric scaling and segmented models are not necessary - the resultant structure is usually continuous. If the material used to construct the model is different than the one in the full-scale structure, an additional scaling ratio is used for material similarity. The elastic models used in hydroelastic experiments may be considered a special case of these structural models, inheriting a large part of the relevant design methodology.

After the natural frequency similarity is established, the stress-strain curves of the material used should be carefully examined in conjunction with the estimated loads. It should be ensured that responses remain within the elastic region. Linear elastic behaviour is necessary for the principle of superposition to be applicable; hence, results measured in regular waves may be used to derive general conclusions only if the above condition is satisfied. When the elastic deformation limit of the material is exceeded, material similarity should be satisfied instead. The stress-strain curves of the full scale structure and the scaled model should have qualitatively the

same form. The strain hardening phenomena, present in plastic response regions, should depict the scaled behaviour of the structure appropriately.

Poisson's ratio of the two materials should be similar, especially if large deformations are expected. Although its effects on bending moments and reactions are negligible, it significantly affects strains in plane stress condition, such as in simple beam bending. Structural damping should also be similar when dynamic responses are investigated. However, scaling of these properties is often very difficult. The question arising is whether the experiments may be considered reliable in such cases. Going one step further from first order similarity (as mentioned in 2.2.2), the term *distorted models* refers to occasions where parameters pertinent to the experiment are improperly scaled. This practice is only suggested when the effects of the violation may be measured and their consequences identified. Poisson's ratios for most materials are known and may also be measured experimentally. Although there are several semi-empirical methods for estimation of structural damping, the phenomenon is not entirely understood and experimental determination through modal testing [12] is again regarded as the most reliable method.

2.3 Selection of hydroelastic ship model properties

A summary of all the models used in the investigations reviewed may be found in table A.1. Although the table does not cover the full details of the experiments, some trends are easily identified. For example, the fact that many researchers tend to reuse a model as many times as possible to compensate for the expensive nature of the production process [2, 13, 14]. Furthermore, the increased number of models produced as years progressed (accompanied by an increase in publications overall) demonstrates a rising interest in the field of hydroelasticity. A more detailed investigation of the trends in design selections reveals important aspects of the nature of hydroelastic experiments.

The way the ship's stiffness is modelled is one of the most essential aspects of the design process and it is used to categorise models. As mentioned earlier, the stiffness may result from the use of a flexible backbone, a series of flexible joints or the vessel may be a continuous elastic model. As one would guess intuitively, the production cost and the related difficulty associated with elastic models results in them being a very rare choice. In fact, the number of elastic models documented in the literature corresponds less than 10% of flexible models and was more popular in earlier years (see [4, 5]). The use of a flexible backbone is, undoubtedly, the most popular, although flexible joints are also commonly used for specific types of investigations (e.g. [2, 15–18]). Differences between these arrangements are discussed in more detail in Section 2.4.

Whilst the distribution of the stiffness in an elastic model is by default variable, uniform stiffness distribution is more commonly used for other model types. It has been demonstrated repeatedly (e.g in [19]) that the first natural frequency in vertical bending and the relevant responses may be accurately depicted without the complicated processes involved in accurate stiffness distribution modelling. Variable stiffness distribution was employed in cases where either higher order natural frequencies became important [13] or torsional responses were investigated [20].

2.4 Hydroelastic ship model categories

Ship models for hydroelastic experiments should be capable of realistically deforming under fluid excitation. Since uniform scaling is used for both model and environment, realistic deformations involve identical strains in model-scale and full-scale. Flexibility is achieved by either constructing a so-called elastic model or, more easily, by producing the model in rigid segments. In the latter case, the segments are joined by means of either a flexible backbone or a series of flexible joints.

Flexible backbone models are most commonly used. The backbone is usually made of aluminium (steel being a less popular option) and may have a uniform or non-uniform cross section. Use of variable cross section allows for distributed bending stiffness and, consequently, more accurate depiction of the higher-order natural frequencies. Openings are often created on the beam in antisymmetric vibration experiments to emulate deck openings on the actual ship and provide the correct shear centre position and torsional stiffness distribution. This can be quite challenging as the shear centre for full scale container ships is located significantly below keel level. Model deflection is measured by strain gauges along the backbone.

Flexible joint models are quite popular because of the inherently adjustable nature of the joints. The same set of joints may be used to emulate various stiffness levels and uniform or distributed stiffness [21]. They are, consequently, more easily adapted than backbone models and deformations are measured by sensors integrated with the joints (e.g. torsional springs [22]). Despite this advantage, flexible joint models are not usually preferred, as the lack of a continuous structure deprives the model of the effects of cross-sectional characteristics, as described above (e.g. effective shear area, location of shear centre).

Elastic models are the most complicated to produce, as the roles of hydrodynamic boundary and excited structure are not separated and the model

hull should act as both at the same time. As always, lengths corresponding to the external geometry of the hull scale linearly (scaling factor λ). However, the bending stiffness should be decreased in proportion to λ^5 and may only be adjusted by modifying wall thickness and internal structure arrangement. The material used should be capable of generating the complex hull geometry while providing an elastic modulus resulting in the required stiffness. The structure should, of course, be manufactured to be watertight and the internal structure should ideally resemble the full-scale ship. If the latter is not true, the shear flow within the cross-section can change significantly, resulting in a different effective shear area and, more importantly, torsional constant and location of shear centre).

It may be easily deduced that the above criteria limit the range of applicable materials and manufacturing methods significantly. Furthermore, similarity of the internal structure is often restricted to essential features, such as deck openings and bulkheads [23] to satisfy the necessary requirements for a realistic response. Combined with the fact that, unlike their segmented counterparts, elastic models may not be modified after production, very few vessels of this type have been manufactured (e.g. [4, 5]). In the present investigation, 3D printing is proposed as a method to achieve the complexity of a ship's internal geometry with a wide range of materials, hence greatly facilitating the production of elastic models.

2.5 Review of hydroelastic models in literature

Hydroelastic testing can vary both in the way the model is designed and manufactured and the testing conditions (and, as a result, the phenomena of interest). The former will be discussed in subsections 2.5.1 and 2.5.2, that look at the number of segments of the model and uncommon design and experimental techniques, respectively. Looking at testing conditions in the literature, it is clear that most of the data regards head waves and vertical bending responses (e.g. subsection 2.5.3 discussing slamming and whipping, subsection 2.5.5 discussing nonlinear symmetric responses and subsection 2.5.6 discussing use of symmetric response data to assess fatigue and buckling). Antisymmetric responses are treated separately in subsection 2.5.4.

2.5.1 Number of segments

It can be observed from the data summary in table A.1 that the majority of researchers select a number of segments between 3 and 6. Slightly larger or smaller values are less common but researchers have applied them in the past for investigations with more specific aims. For example, 2-segment models are quite common in cases where the experiments focused on the

loads amidships and the modal responses were not important [16, 18, 24]. More segments were used, in some cases, in hope of depicting the vessel modes more accurately [19, 25–27]. Extreme cases include the elastic models, were there is no segmentation at all and few cases with very large number of segments [28, 29]. The advantages of the latter have not been clearly demonstrated.

2.5.2 Model design and technique variations

Many researchers investigate either the use of alternative methods to obtain hydroelastic data or ways to optimise the currently used techniques. Design of flexible models was extensively discussed by Wu et al. [21], who investigated the ways it can be optimised by selecting, for example, the ideal number of segments for the investigation. Marón & Kapsenberg [30] analysed the various aspects of the design process of a hydroelastic model and classified the options a researcher is called to choose from. Interestingly, they argued that hammer tests for the determination of dry modes are insufficient because of the significant amount of noise in the responses and the first mode masking the rest; testing with specialised shakers which apply loads at specific frequencies was suggested instead. The publication focused on the ways to organise the design, construction and experimentation process to achieve accurate results.

Malenica et al. [27] constructed a simplified model of a rectangular barge as part of a benchmark study. The barge did not represent a real vessel but was designed to be very flexible, to the point that its deformations were clearly visible with the naked eye and monitored by optical systems. The barge was subsequently subjected to waves in various headings and the RAOs in vertical bending [27], horizontal bending and torsion [31] were measured. The results were used to validate numerical codes, which were found to agree well.

Chen et al. [5] constructed an elastic model of the S-175 container ship using ABS. The flexible material allowed them to use a sufficiently large scale. However, the model comprised of only the outer shell and a number of bulkheads - further detail in the internal structure would produce an excessively stiff model. The model design process is discussed more extensively in [23]. The experimental results were re-processed by Du et al. [32] to argue the benefits of using wavelet analysis compared to the more "traditional" Fast Fourier Transform (FFT) when post-processing experimental results for springing of a slender hull.

Houtani et al. [33] manufactured an elastic model of a container ship out of urethane foam. Once more, the model consisted of an external shell with large deck openings and a series of transverse bulkheads. The vessel was tested in an ocean basin, allowing to investigate both symmetric and antisymmetric responses. The authors argued that segmented models,

regardless of the backbone complexity and correct scaling of the first few natural frequencies (both symmetric and antisymmetric), cannot depict the behaviour of the full-scale ship. The above is a result primarily of the incorrect location of the shear centre, which should be below the keel, resulting in strong coupling between horizontal bending and torsion and can cause differences in the antisymmetric mode shapes between model and full-scale ship.

Coppotelli et al. [34] used a flexible backbone model to investigate an output-only analysis, suggesting their methodology for the identification of modal parameters of full scale ships at sea, where wave excitation is not measurable. It was demonstrated that, using this method, it is possible to retrieve significant amount of information concerning the ship structure itself [35]. The technique was validated by comparison of model test results and full-scale measurements [36].

2.5.3 Hydroelastic models for investigation of slamming and whipping

Transient hull responses due to slamming have been investigated by many researchers, focusing mainly on high-speed craft, where these responses are more common. Extensive research has been performed concerning the responses of the 112m INCAT wave-piercing catamaran. Lavroff et al. [2] used a flexible joint model featuring a separated centrebow to investigate the effect of displacement variations and forward speed on whipping. The bending loads at two cross sections along the demihulls were derived by torsional spring measurements.

The dry and wet modal characteristics of the vessel were measured and used to evaluate slamming events. The damping ratio was found to significantly increase with forward speed [2]. On the other hand, slamming loads decreased with increasing wave height, due to increased immersion of the centrebow and the relevant added mass [37]. Good agreement was found between model-scale results and full-scale measurements [38]. The effect of the centrebow on ship motions was investigated in more detail by Matsubara et al. [39]. The centrebow was connected to transverse beams equipped with strain gauges to evaluate slamming events.

The same model was later used to investigate extreme slam events [40] and also to determine the relationship between wave characteristics and resulting slamming [41]. The majority of slams were found to occur near the aft end of the centrebow and the general trend identified was that slam load increases with vertical velocity. However, the range of magnitudes observed for the same vertical velocity was not insignificant. Weak correlation was found between the combination of wave height and wave encounter frequency and the position of peak sagging slam load.

The lessons learned from the above studies and their predecessors were summarised by Thomas et al. in the form of guidelines [42]. The influ-

ence of wave height was investigated in more detail and results indicated strong correlation with slam load magnitude [43]. Using the same model, French et al. [44] investigated slamming in a range of irregular seas. It was demonstrated that relative vertical velocity between the ship and the free surface is not sufficient as an indicator for the resulting slamming loads. The effect of ship motion on slam loading was found to be less significant with increasing encounter frequency.

Although the model used in the above experiments offered important insight on the mechanisms related to slamming of high-speed craft, responses could be obtained in limited detail. The joint stiffness ensured an accurate scaling of the first vertical bending natural frequency and the three segments a satisfactory representation of the relevant mode. However, the loads were only measured in two sections and the extent to which the centre-bow deformation may be considered realistic was not demonstrated. Assuming the latter does not affect the flow around the vessel significantly, the measurements may only be used for relative comparison of slamming loads. Indirectly acknowledging the limitations of the model due to lack of a continuous structure, the authors simulate its behaviour using a three-degree-of-freedom spring-mass system [2].

Ge et al. [45] compared the slamming behaviour of a catamaran, as observed in experiments, with predictions of a three-body theoretical dynamic model. A very interesting aspect of this investigation is the extensive error analysis of both the theoretical model and the experimental procedure, including consideration of wave frequency effects and seiching phenomena in the towing tank.

Very detailed work concerning a semi-displacement fast ferry (Fincantieri MDV3000) was presented by Ciappi et al. [13] who investigated both the RAOs of the vessel and its slamming behaviour. Prior to that, the model had been successfully validated using full-scale measurements [46]. The effect of forward speed on hull vibrations was investigated [47] and hydrodynamic damping was found to increase with forward speed (as in [2]), especially after the critical value for the Froude number corresponding to transom flow separation. Due to the behaviour of such monohulls, the research mainly focused on transient responses and structural loads caused by whipping. Numerical schemes were implemented to predict slamming behaviour and were compared to the experimental measurements with good agreement, especially when compared to results by Wagner and von Karman solutions [48]. Slamming was found to occur in clusters [3] where individual slamming events are mutually dependent and thus difficult to predict with statistical models. A criterion for the identification of slamming events based on measurement of whipping was proposed [49].

The backbone model of the MDV3000 featured a variable stiffness distribution, ensuring a more accurate depiction of the bending natural frequen-

cies and modes. Use of six segments longitudinally resulted in satisfactory results for the 2-node, 3-node and 4-node natural modes in vertical bending. It was demonstrated that the rubber strips commonly added between the segments to make the hull waterproof significantly increase modal damping [13]. Although this could be a good intermediate solution (in terms of structural detail) between a standard backbone model and an elastic model, the associated manufacturing complexity and cost would be more similar to the latter than the former.

2.5.4 Hydroelastic models for investigation of antisymmetric vibrations

The term "antisymmetric" regards hull vibrations outside the symmetry plane defined by the longitudinal and the vertical axis of the ship, namely horizontal bending and torsion. These responses are of special interest in the case of ships with large deck openings, such as container ships. The geometry of the cross sections of these ships results in a shear centre well below the level of the keel, causing strong coupling of the aforementioned vibrations.

Sun & Guedes Soares [50] investigated such phenomena on a dry hull steel model of a ship with large deck openings. A relatively small scaling factor was used and the loading was applied directly by mechanical means. This allowed the investigation of very large hull deformations and associated nonlinear responses. It was demonstrated that careful application of boundary conditions is necessary, particularly in regards to warping. Furthermore, it was found that the stiffness contribution of some stiffeners was decreased for high deflections. Iijima et al. [17] compared the ability of a strip theory code and a Rankine source code to predict torsional vibrations responses. A series of experiments were conducted for validation purposes, where the segments were linked by a series of force transducers. The container ship model was subjected to regular waves from directions between 0° and 180° at 30° intervals. Good agreement with the experimental results was observed for the Rankine method, especially for small wave heights. Strip theory produced less satisfactory results, while both methods lacked accuracy for the extreme wave height of 15 m. The latter was attributed to nonlinearities in the bending moments near the bow section (this effect would be later investigated in greater detail by Zhu et al. [29] , see 2.5.5). It was concluded that the worst loading condition results from waves of length equal to 35% of the ship length, approaching at a 120° angle.

A different approach was presented by Iijima et al. [28]; the stiffness distribution was achieved by employing an aluminium backbone with openings along the length. The model consisted of 17 rigid segments made of Divinycell foam and the backbone was located on the main deck. The resulting bending (horizontal and vertical) and torsion natural frequencies demonstrated adequately small error after scaling. The advantages, however, of

a model with a number of segments significantly greater than standard practice indicates were not demonstrated. Furthermore, the correct shear centre location (below the hull) could not be achieved and, consequently, the horizontal bending and twisting modes were not coupled appropriately. An investigation of the higher-order harmonic responses followed [29] and the measurements were used to validate numerical codes [51] with good agreement. A similar model was used by Oka et al. [20]; little information was, however, provided concerning the design of the backbone to achieve the desired distributed stiffness and shear centre location.

The above experiments demonstrate the limitations of segmented models more profoundly. Symmetric vibration experiments mainly rely on the accurate scaling of the two-node vertical bending natural mode and the relevant natural frequency. When investigating antisymmetric responses, however, accurate depiction of the stiffness distribution and the location of the shear centre are crucial. As discussed in Houtani et al. [33], the correct location of the shear centre (and, consequently, appropriate coupling of the antisymmetric modes) is, with very few exceptions, not achieved with non-elastic models. Achieving these design requirements without a continuous model results in a backbone mimicking a ship shape, which overcomplicates the design and defies the main purpose of segmented models: simplicity in design and manufacturing. It can be argued that, with a similar level of design complexity, an elastic model with a more accurate depiction of the cross-section could be produced.

2.5.5 Hydroelastic models for experiments on nonlinear phenomena

Storhaug & Moan [52] extensively investigated the effect of the geometry of the moving ship on the waves encountered. A series of hypotheses concerning the interactions of waves and a blunt wall in motion, such as the bow of the ship, were modelled numerically. Experimental implications were addressed, including the inability to produce, in a towing tank, waves corresponding to an encounter frequency approximating the 2-node natural frequency of a stiff vessel unless a small scaling factor is used.

Takaoka et al. [19] investigated the effect of stiffness distribution on the behaviour of a flexible backbone model for two container ship sizes (5,000 and 13,000 TEU, respectively). Their work, concerning whipping phenomena, concluded that the percentage of increase in bending moment amidships due to whipping was not affected significantly by the stiffness distribution (uniform or variable). Contrary to their expectations, no strong correlation between ship size and slam loads was observed but it was reported that bow flare shape has a significant effect. Previous research had already established the nonlinear contributions of the latter on vertical bending moments (e.g. [53, 54]). Watanabe et al., in particular, produced an elastic model for the S-175 container ship and a modified model of the

same ship with increased flare [4]. Although the double amplitude of the vertical bending moment measured was not significantly different due to the bow modification, peak values of sagging bending moment were found to increase. Similarly, Zhu et al. performed tests in head, oblique and quartering seas [51] and investigated the effect of bow flare shape on torsional vibration of the hull [29]. High-frequency responses were found to be almost dominant in irregular waves with short wave peak periods, an effect which seemed to increase with forward speed [55].

Nonlinearities in wave-induced loads were investigated, both experimentally and numerically, for large [56, 57] and ultra-large [58, 59] container ships. Drummen et al. [56] measured a significant contribution of the 4^{th} and 6^{th} harmonic to the bending moment (up to 50% of that of the 1^{st} harmonic). The results by Zhu & Moan [57] agree with the above; in this case, the underestimation of loads is demonstrated by experiments and calculations for a 8,600-TEU container ship. Experiments for this vessel, as well as one with capacity of 13,000-TEU indicate limited asymmetry between hogging and sagging vertical bending moments, with an increase due to high-frequency vibrations being more significant in the latter [58]. This increase was found to vary with heading angle of the waves, with significant increase under 30° angle and 60° angle for hogging and sagging, respectively [59].

Miyake et al. [26] focused on superharmonic resonance phenomena for a mega-container ship. Their experimental data suggested that irregular seas result in more severe responses than similar regular waves. Fonseca et al. compared numerical results with experimental data [60] and commented on the lack of accuracy of strip theory with increasing vessel forward speed. Experiments using the same model (S-175 container ship with a "rigid" backbone, thus ignoring hydroelastic effects) were performed [61] to shed light on the nonlinear parts of the response, concluding that nonlinear phenomena play an equally important part at low and high speeds. Investigations on a more recent container ship design identified further uncertainties regarding the source of motion nonlinearities, especially when comparing the results of the two designs. Measurements of green water loads were also presented and analysed [62].

The behaviour of a blunt ship (similar to a bulk carrier or a tanker) was investigated by Zhu et al. [16] in extreme wave heights (four wave heights between 6 and 14 meters in full scale). A large number of tests were performed in regular and irregular waves, head, beam, quartering and following seas and in an extensive range of wave heights and lengths. The model comprised of two segments connected with a force transducer and the measurements included hull and green water pressures, as well as horizontal and vertical bending moments. The investigation focused on nonlinearities caused by the increased wave height; no assymmetry in the vertical bending

moment of this ship was observed, whereas significant nonlinear effects were reported in the pressures measured. The results were used to validate a simplified prediction model, designed for use in practical ship design. It was suggested that short-term values of sea states associated with extreme wave heights and resulting in extreme structural loads should be taken into account during ship design.

Denchfield et al. [63] investigated the hydrodynamic behaviour of a Leander-class frigate in abnormal waves and investigated the effects of forward speed. Increased slamming severity was observed in the presence of rogue waves, compared to a statistically equivalent irregular sea. The experimental measurements were compared to numerical results of two models: one derived from two-dimensional strip theory and a partly-nonlinear panel-based method [64]. Subsequent measurements of global structural loads [65] indicated a significant increase in maximum bending moments in both hogging and sagging direction in the presence of abnormal waves, compared to relevant random seas. It was also concluded that bending moments under these conditions may, in some cases, exceed the design rule margins.

Similarly, Kinoshita et al. [25] investigated the behaviour of a container ship in regular and freak waves. The segmented model's stiffness originated from a hollow aluminium cylinder used as a backbone. The 10 segments of a model were not rigid but manufactured from flexible urethane foam. The authors argued that the latter enabled them to capture the flexible responses due to bottom or bow flare slamming. However, the ways in which the material and the design of the structure realistically depicted the behaviour of the full scale ship were not demonstrated.

The responses of an FPSO in abnormal waves, namely a reproduction of the New Year wave, were investigated by Clauss et al. [66]. The measurements from their 3 segment model were compared to results from a range of numerical codes. It was demonstrated that the resulting loading was within classification society rules limits; furthermore, that frequency domain analysis is capable of accurately predicting the relevant bending moments. It was argued that the main advantage of time-domain analysis is the ability to predict local loads (e.g. resulting from green water or slamming). Relevant results agreed reasonably well with the experimental data [53]. Strong correlation was identified between the position of the rogue wave with respect to the vessel (phasing) and the resulting loads. The model was subsequently upgraded by installation of force transducers at two vertical levels (main deck and bottom) to identify vertical bending loads in more detail. By comparison, frequency domain methods were again found to be sufficient to predict maximum bending loads [67].

While tests in abnormal waves mainly depend on the capabilities of the wave maker, most investigations in nonlinear phenomena regard the hydro-

dynamic interactions of complex-shaped hulls and, especially, vessels with increased flare. The manufacturing processes to produce the models can often be quite complicated and expensive. Novel manufacturing technologies, such as additive manufacturing, could be a more appropriate way to achieve these geometries. The additional effort necessary to make an elastic model would not be negligible but the accurate representation of higher order modes could provide increased insight in the nonlinear phenomena.

2.5.6 Hydroelastic experiments used for structural assessment

Although most investigations focus on the structural responses of the hull-girder, the ultimate goal of these studies is to assess the structural integrity of the vessel, both locally and globally. Loading exceeding the classification society rule predictions, especially when applied periodically or as an impact, may result in structural failure incidents, namely fatigue, buckling and plastic collapse. Identifying stress concentration points and calculating the vessel ultimate strength are essential parts of the design process.

Fatigue caused by wave-induced vibrations was investigated using scaled models of large [68] and ultra-large container ships in head [69] and quartering seas [70]. Drummen et al. [68] demonstrated that strip theory may over-predict fatigue damage caused by wave frequency by 15% and caused by high frequencies by 120%, resulting in an overall overestimation of approximately 50% for the midship section. Storhaug et al. suggested that hull vibrations are the dominant cause of fatigue cracking, with the percentage increasing from bow to stern (65% amidships) [69]. It was also found that higher fatigue loads are induced by quartering seas than head seas and that hogging moments under these circumstances may be well above those predicted by IACS [70]. Storhaug presented a review of a series of relevant experiments [71], summarising the findings and suggesting that current guidelines leave room for improvement.

Dudson et al. [15] performed experiments with a pentamaran container ship model which was self-propelled using four water jets and an automated pilot. The 4-segment model was tested in a variety of irregular and regular waves in an ocean basin with a forward speed of 41 knots (full scale). Forces and moments were measured in all three directions and both seakeeping and manoeuvring tests were performed. The addition of rudders improved manoeuvrability and reduced horizontal bending moment in the fore part of the vessel. Further calculations demonstrated increased fatigue damage in head and quartering head seas and a significantly reduced fatigue life due to the increased flexibility of the vessel.

Sun & Guedes Soares [50] investigated the ultimate torsional strength of ships with large deck openings by subjecting a scaled steel model to torsional loads. The vessel was not excited by waves but by a directly applied torque to identify the ultimate load bearing capacity and the relevant fail-

ure mechanism. Limited correlation was found between initial geometrical imperfection and ultimate torque, as it was demonstrated that the model fails because of plastic collapse.

The fatigue results above could not be directly measured on the models. The backbone measurements were used to extrapolate the global behaviour of the ship to local load concentrations and identification of "hot spots". Use of an elastic model with accurate internal structure would have eliminated some of the assumptions as the loads would have been measured directly on the structural components.

2.6 Summary and discussion

Hydroelastic experiments have evolved greatly during the past decades. Researchers have come to investigate highly nonlinear phenomena including significant changes in the submerged geometry [57], abnormal waves [64] and higher-order resonance [56]. The measurements have been used to assess the structural integrity of the vessel and, in some cases, the responses after damage were modelled [18, 24, 72]. The effects of whipping [2] and torsional loads [28] have also been investigated. More detailed load measurements were, in some cases, achieved by use of elastic models [5, 32]. It has been clearly demonstrated that the hydroelastic contributions to the loads are, in many cases, quite significant and should be considered in design. Furthermore, that our understanding of dynamic loading on the ship hull is still incomplete and experiments are necessary to validate the constantly improving computational models.

However, the extensive production of elastic models still appears as a distant prospect and had not been attempted for many years [4, 5]. The only exception was a recent investigation by Houtani et al. [33] who, nevertheless, manufactured their model in a very similar manner as previously. Despite the advancements in manufacturing technologies, even the production of a segmented model is, in many cases, considered overly expensive and the same models are used in long series of investigations (e.g. [14,64,72] and [2, 40, 44]). However, as was demonstrated above, the absence of elastic models in current research is not due to lack of motivation rather than lack of an efficient concept. The current investigation aims to overcome these difficulties by using 3D printing to produce, in a cost-effective manner, models with the cross-section of a ship, to accurately represent shear deformation effects.

Chapter 3

Background to additive manufacturing of structural components

3.1 Overview

3D printing is an additive manufacturing technology, initially introduced as a quick and inexpensive way to create prototypes. Since its first steps in the early 1980s, additive manufacturing has come to include a large number of production methods and a wide variety of materials, rendering it highly adaptable to one's needs. Its current applications involve a wide range of disciplines [73–75]. Structural characteristics, geometric precision and production cost are interrelated aspects of the process and a direct result of method-material combination; the above are evaluated on a case-by-case basis.

3.2 Project requirements

Within this investigation, 3D printing is used to produce models with predefined performance. The most important parameters to be controlled during the process are material characteristics, model accuracy, feature detail resolution and build volume [76]. In this case, the material needs to have a predictable modulus of elasticity and the relevant behaviour should be sufficiently close to isotropic or at least orthotropic in a way affecting the responses in a limited and predictable manner. Although ship models cannot be as detailed as their full-scale counterparts, all structural details to be included in the final design should be accurately described and, mainly, able to withstand the imposed loading without deterioration. The build volume is important; only part of the model may be constructed at a time,

larger print volumes, however, ensure greater model scale flexibility and faster production rate.

3.3 Categories of additive manufacturing

"3D printing" is commonly and mistakenly used for all additive manufacturing processes without differentiating between them. However, the truth is this group of techniques have very distinct characteristics, with some resembling a printing process more than others. Depending on the technology, the nature and initial form of the material also vary. The number of technologies is impressive and constantly growing; for the sake of conciseness, only methods deemed as popular within the 3D printing community and/or compatible with the project at hand will be analysed below.

Table 3.1: Materials & procedures of additive manufacturing methods. Full names of methods: stereolithography, digital light processing,selective laser sintering, inkjet, freeform filament fabrication.

Method	Material form	Material range	Production method
SLA	Liquid	Resins	Laser beam
DLP	Liquid	Photopolymers	UV light
SLS	Powder	Plastic, metal, composites	Laser beam
Inkjet	Liquid, powder'	Plastic, rubber	UV light, binder
FFF	Filament	Plastic, rubber, nylon, composites	Hot extrusion

Stereolithography (SLA) and digital light processing (DLP) have many similarities, as both use material in liquid form contained in a tank (resins and photopolymers, respectively) to be selectively solidified by use of a light source. The former method, which was the pioneer of additive manufacturing technologies, uses a laser beam to produce the print in a layer-by-layer fashion. The latter's light source is a more conventional arc lamp and the method is applied in a single pass, rendering it much faster than SLA. Elongation to break was recently found to be higher for parts produced using SLA, compared to ones produced with selective laser sintering when top quality of material was used for the former [77]. Although the geometric accuracy and resolution of both these methods are among the highest in their field, produced parts need post-processing to achieve acceptable mechanical properties. It should also be noted that these printers are more

expensive than others and the build space is quite limited, with Pegasus Touch Laser SLA's 177 x 177 x 228 mm being on the high end of the range. SLA 3D printers with a cost below $4000 are considered relatively inexpensive.

Table 3.2: 3D printing methods advantages & disadvantages

Method	Advantages	Disadvantages	Project compatibility
SLA	Accuracy	Build space Post-processing	✗
DLP	Accuracy Speed	Build space Post-processing	✗
SLS	Strong parts Accuracy	Porosity	✗
Inkjet	Accuracy	Cost	✗
FFF	Material range Adaptive Predictable	Extensive calibration Non-isotropic results	✓

Selective laser sintering (SLS), also known as selective laser melting, is one of the few methods using powdered material. A layer of material is spread evenly on the bed and the printer selectively interacts with the material and fuses the particles. The bed then drops incrementally and a new layer is formed. This method requires isothermal conditions and a sealed build chamber is necessary. Resulting parts are very strong but often porous and although this problem has been significantly reduced in newer printers, this process is not complete. Consequently, this method may not be advisable when a fully dense part is required [78].

The inkjet method includes two sub-methods and may use powdered or liquid material. In the former case, similarly to the SLS method, a layer of material is spread evenly on the bed and the printer selectively sprays binder material. The bed then drops incrementally and a new layer is formed. The latter technology selectively sprays material in liquid form on a heated bed, to be subsequently solidified by use of UV light. Contrary to expectations, it has been suggested that printing multi-material objects with this method does not result in reduced fatigue life despite the interface created [79]. The main disadvantage of this method is the increased cost of relevant equipment and materials.

Finally, the most popular and recognisable additive manufacturing method is filament deposition modelling (FDM) or freeform fabrication (FFF). In this case, the material comes in solid filament form and is usually either ABS or PLA, although a number of FDM printers are also able to use nylon and/or elastic material. The filament is subjected to hot extrusion through a specially designed head and the three-dimensional motion to create the

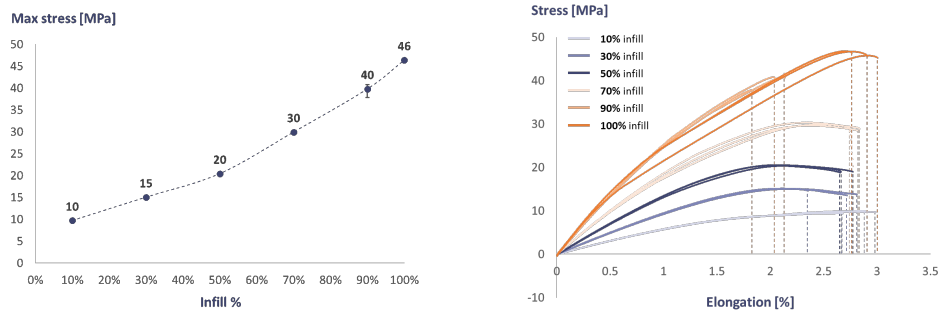

(a) Strength (b) Elastic modulus & elongation

Figure 3.1: Effect of infill ratio on strength, elastic modulus and elongation on PLA 3D-printed coupons under tensile loading [80].

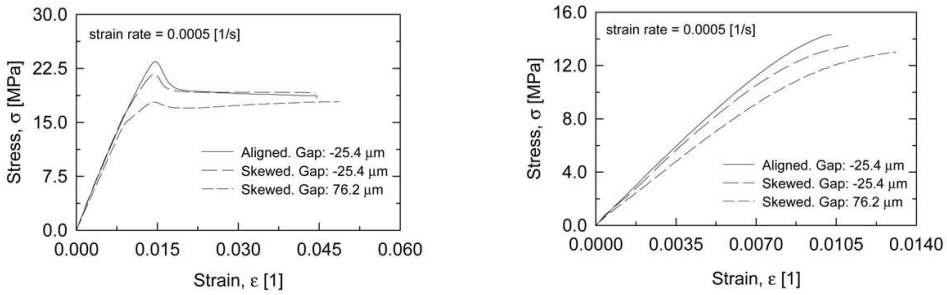

(a) Longitudinal (b) Transverse

Figure 3.2: Effect of mesostructure (void density) on the stress strain-relationship of ABS 3D-printed coupons under tensile loading in the longitudinal and transverse direction [81]

layers is either performed by the head, the platform, or both. Produced results by FDM (patented by Stratasys) are more accurate and reliable than similar FFF ones, but the latter are gradually evolving as well [78]. The process should be carefully designed and well monitored as implications during printing may result in poor layer-to-layer adhesion.

All the above methods, with the exception of those using powdered material, need support to build complex structures with overhangs. This is fortunately a relatively easy process as the support material is created by the 3D printer during the printing process and may be removed after product completion. Among these methods, the ones mostly used for components with mechanical performance requirements are the filament-based ones. For this reason, only materials, process parameters and printers relevant to these methods will be further analysed.

Mechanical properties of the product are significantly affected by the manufacturing process. Apart from influences from the material (ideal me-

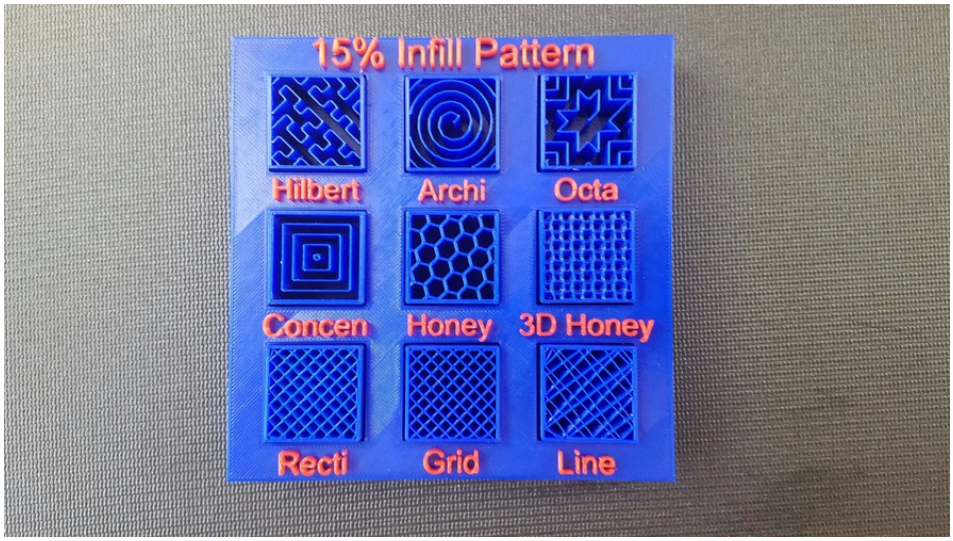

Figure 3.3: Pattern examples produced with fused deposition modelling (Source: Kronr / Pinshape)

chanical properties) and the 3D printer specifications (maximum precision, surface quality, material compatibility), extrusion temperature and speed should also be carefully considered. These parameters are calibrated according to the material used. Required temperature between each layer deposition varies as well, with ABS operating better with relatively small temperature differences between each layer and the previous and PLA necessitating cooling. Cooling speed of the finished part is also important, as materials with large thermal expansion rate (e.g. ABS) tend to deform significantly without controlled cooling or mechanical restrain (often both are necessary). Furthermore, the resulting volumetric difference should always be considered during the design phase as it can cause inconsistencies where geometrical accuracy is required. The effects of the various parameters on print quality are analysed in later sections.

3.4 Available 3D printing materials

Polylactic acid (PLA) is a polyesteric material with an elastic modulus of up to 3.5 MPa and glass transition temperature of 60° C. Acrylonitrile Butadiene Styrene (ABS), on the other hand, is a styrenic plastic with an elastic modulus of 1.7 to 2.8 GPa and a glass transition temperature of 100° C. It is an amorphous material so it has no true melting point. The higher glass transition temperature of ABS results in more significant shrinkage during cooling and possibly deformation when printing larger areas if no preventive measures are taken as discussed above.

Elastic filaments are becoming increasingly popular, although more difficult to print with than ABS and PLA. Nylon 618 has an elastic modulus of 0.15 GPa and glass transition temperature of 48° C. Ninjaflex is a polyurethane with the same elastic modulus and a glass transition temperature of 66° C but suffers degradation if submerged in water for a prolonged period and is thus incompatible with the project. Flexible materials aren't compatible with all 3D printers as they often require significantly different extrusion temperature, lower printing speed and possibly different nozzle (e.g. nickel-coated nozzles).

3.5 Effects of infill ratio, layer height and infill pattern

Due to the nature of fused deposition modelling, produced parts do not have the same density as the parent material but include a smaller or larger number of gaps. One way to describe a print is probably a solid external shell around a cellular core. When the aim mainly relates to the external appearance, infill ratios as low as 5% may be used without undermining the quality. Many printers can achieve infill ratios close to 100% resulting in a dense product with (homogenised) mechanical properties closer to the parent material. Layer height may affect not only the production speed but also the final quality, depending on the behaviour of the material and the available means of temperature regulation.

It can be easily deduced that a low infill ratio and high layer thickness accelerates the printing process and vice versa. Similarly, maximum tensile strength and production cost both increase with infill ratio. Print quality (referring to surface precision) is strongly correlated with layer height, with thinner layers producing a smoother and more detailed end product. Figure 3.1a depicts the effect on maximum strength, whereas the resulting stress-strain relationship may be observed in figure 3.1b. Both figure correspond to PLA coupons under tensile loading. It is also clear from 3.1b that the elastic modulus was found to increase with infill ratio. Lantern Robotics [82] suggested producing of parts with zero infill ratio and subsequently filling them with hot melt adhesive (HMA) to improve mechanical properties while reducing the cost. This method, although proven to be effective, is incompatible with the nature of the present investigation.

A wide variety of printing patterns may be used (see figure 3.3, affecting both the appearance and the mechanical properties of the product. Some patterns are used to create good surface finish (e.g. hilbert curve, concentric), whereas others to contribute to the structure (e.g. linear, diagonal, grid, honeycomb). Infill angle can matter for some infill patterns too: the rectilinear pattern has been found to produce slightly higher values of maximum strength for PLA [80] and ABS [83] coupons when printed at 45° (as seen in figure 3.3). Investigators used not only experimental methods [84]

but also FEM software and optimisation methods to identify the optimum layer orientation [85] but the significance of pattern selection seemed to be decreasing with infill ratio [80].

Finally, it should be noted that regardless of the infill ratio and infill pattern selected when designing the process, there are always small air gaps between the printed lines, even in cases where the product is considered completely solid. The size of the air gaps can significantly affect tensile strength [85]. Using a negative air gap (slight overlap) can improve both strength and stiffness [83]. The latter was also made clear by Rodríguez et al. [81] and is depicted in figure 3.2. The elastic modulus in this case was found to be uniform in both directions (1733 and 1714 MPa, respectively).

Printing speed and temperature

Printing speed and temperature were found to be unrelated to mechanical properties when printing with PLA [86] but there is serious doubt about the generality of this statement [87]. An extrusion temperature and speed combination incompatible with the filament used may result in implications during printing, such as filament jamming. As the exact position of the temperature measuring sensor (relative to the extruder heating element and nozzle) varies from printer to printer, relevant guidelines from the material manufacturing companies should only be treated as such and a calibration is necessary on a case-by-case basis to achieve high quality prints [87].

3.6 Effects of layering

Anisotropy cannot be avoided in layer-based methods and a reduction by 20%-30% of the maximum strength in the direction perpendicular to the layers, compared to the in-layer magnitude, was measured, regardless of printing pattern [80]. In earlier investigations, measurements revealed a maximum in-plane load up to two times the cross-plane one [88]. Less significant anisotropy was observed in compressive loading [88, 89]. Models produced with a series of open-source, self-assembled 3D printers (RepRap models), had consistent mechanical properties, especially when ABS was used [87]. The properties measured were, on average, better than those produced by commercial printers [83].

3.7 Available joining techniques

As discussed earlier, the currently available 3D printing technology would not allow for the whole vessel to be printed at once. The model should thus be printed in sections and a joining technology to be employed to obtain a continuous model. As materials used in fused filament fabrication are thermoplastics, this can be fulfilled either by glueing or welding the

segments. Glueing, in turn, may be achieved by use of either adhesives or solvents, depending on the material used.

3.8 Summary and discussion

Additive manufacturing is a rapidly evolving group of technologies, each with its own advantages and intricacies. From a comparison between the different members of this group, 3D printing was found to be clearly the most compatible with the current project. It combines cost-effective manufacturing with relatively large build space (for an additive manufacturing technology) and predictable levels of void density. The relevant material range is by far the widest among additive manufacturing technologies and there is number of relatively easy joining techniques available for the finished components.

As the technology is relatively young, particularly so for use on structural components, the literature on mechanical properties of 3D printed components is still limited. Some general principles regarding the effects of printing parameters on the mechanical properties are understood but case-by-case experimental characterisation is still advisable for projects where the precise identification of these properties is crucial.

Chapter 4

Model design & production

4.1 Overview

As demonstrated in the previous chapter, the process of designing an elastic model with a geometry similar to that of the full-scale vessel is challenging. A ship may be represented at a specific scale using a very narrow range of materials, if any. These materials, in turn, may or may not be compatible with the available 3D printers. In this chapter, a number of different vessels are investigated and the design options available for each of them are presented. The calculations in sections 4.2.1 to 4.2.3 are based on the moduli provided by the material manufacturers.

The calculation of the 2^{nd} moment of area was based on the assumption that a solid wall of each of the materials would be constructed, i.e. 100% infill ratio. The 2^{nd} moment of area regards the midship section, and its distribution was not calculated at this stage for a number of reasons. Firstly, it has been demonstrated that natural frequencies in vertical bending are influenced predominantly by the stiffness amidships [19]. Additionally, it was assumed that accurate depiction of the bending stiffness amidships almost ensures a sufficiently accurate depiction of the bending stiffness distribution, should the same thickness be used for the entire vessel. Detailed calculation of the latter was only performed for the S-175 container ship and is presented in the relevant section.

Not all structural detail can be included in an elastic model; doing so would, in most cases, prove unnecessarily time-consuming. Due to the nature of tests in head seas, only the structural entities actively affecting vertical bending stiffness need to be included. Consequently, stiffeners relevant to local responses (e.g. local bending of panels due to hydrostatic loads) can be omitted for design simplicity. More extensive consideration is necessary in the case of investigations in antisymmetric vibration, as the geometry of the cross section can significantly affect the shear flow. Even then, not all structural elements can be included and “gray zone” cases

should be expected. Final decision depends on the designer and limitations of available manufacturing methods.

A number of vessels were considered for use within this project. The final selection was based on the ability of the vessel to explore the concept of a true elastic model through the complexity of its cross-section. Some designs had to be abandoned as not complex enough or not realistic enough; constant re-evaluation of the target was necessary, keeping in mind that the criteria should focus almost entirely on the structural aspects. The final selection clearly illustrates the above.

A summary of the design attempts based on theoretical values for the mechanical properties is discussed in sections 4.2.1, 4.2.2 and 4.2.3. The actual values from mechanical testing in section 4.3 are then used in sections 4.4 and 4.5 to produce a final design for the vessel.

4.2 Design iteration for elastic model selection

4.2.1 Iteration 1: Rectangular barge

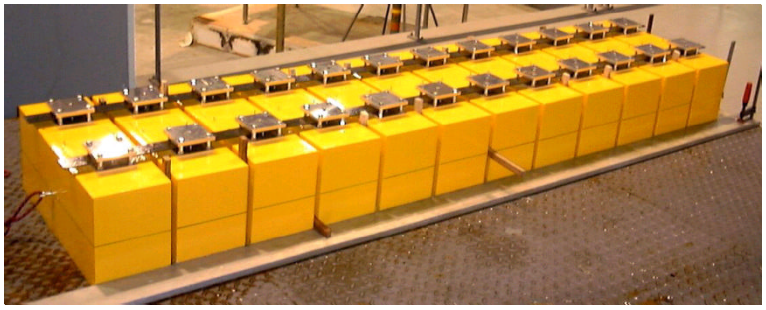

Figure 4.1: Barge consisting of 12 rectangular floaters connected by two steel backbones [27]

The first model considered for investigation was the rectangular barge manufactured by Malenica et al. [27]. The barge consisted of 12 floaters connected by a set of two backbone plates. The simple geometry of the vessel combined with the abundance of experimental and numerical results available were the main motivations behind this selection. Furthermore, the design is sufficiently flexible for its deformations to be clearly visible with a naked eye, rendering measurements potentially easier.

The vessel's stiffness was found to be quite low for an elastic model of the size (0.6 m width by 0.25 m height). It was consequently significantly difficult to find a material compatible with it. Ninjaflex was proposed, as it is the most flexible material currently available, with an elastic modulus of $11.89 \times 10^6 N/m^2$ for 100% infill. Despite the material's poor behaviour in water, it was the only potentially feasible option due to the high flexibility

of the barge - water absorption issues could potentially be resolved with appropriate coating. The required thickness was then approximately 4.4 mm for a U-shaped section and less than 1.5 if a deck with large deck openings was constructed instead.

The deflection RAOs of the barge were calculated using the strip theory linear hydroelastic code MARS. The magnitude amidships and at the aft quarter length of the vessel was used as comparison to assess hydrostatic deflections (Figure B.2). The barge was then modelled in ANSYS using a symmetry condition along the x and y axes and a pin joint support at the corner (free condition would not create sufficient support for static test). The thickness was found to be too small, even for the U-shaped version, as the hydrostatic pressure resulted in large deformations on the bottom plate.

Installation of transverse bulkheads was implemented to reduce the free length of the plate but the magnitude of the deformation could not be sufficiently reduced. The significant amount of ballast mass required to achieve the desired draft of 0.12 m partially compensated for the hydrostatic load but the deflections were still at unacceptable levels (five times the plate thickness), as may be seen in Figure B.1. Furthermore, the ballasting procedure would have to be very carefully designed so as not to damage the model either during its transportation or after placed in the water. As a result, the barge was considered to be less relevant to realistic ship structures.

4.2.2 Iteration 2: Leander-class frigate

The investigation regarding the design of the rectangular barge model clearly demonstrated that simplicity of the external geometry is irrelevant to the manufacturing feasibility of the vessel as an elastic model. A Leander-class frigate, for which experimental and numerical results have been produced in the University of Southampton (e.g [14]) was introduced as a potential candidate.

The material investigation included a wide range of materials, as shown in Figure B.3 (Appendix B). The midship section (Figure 4.2a) was simplified by including only 13 stiffeners, whereas the smaller stiffeners were substituted by an appropriate increase of plate thickness.

A number of materials on the high end of the stiffness range (PLA, ABS) resulted in cross sections which couldn't be manufactured and were eliminated early in the process. Elastomers were also considered incompatible, as the required wall thickness resulted in an unrealistic cross-section geometry (thickness of external shell comparable to stiffener breadth, see Figure 4.2b). Although a cross-section with T-glase (Figure 4.2d) would be quite realistic, the required thickness could not be achieved with the available printers. A nylon cross-section (e.g. Bridge, see Figure 4.2c) would

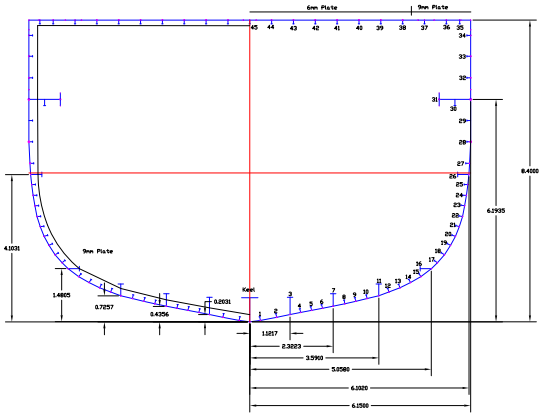

(a) Full-scale

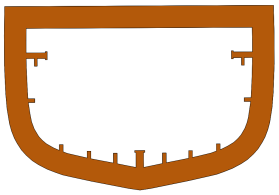

(b) FlexSolid

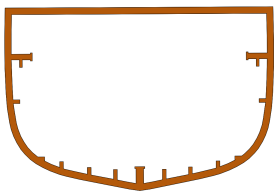

(c) Bridge

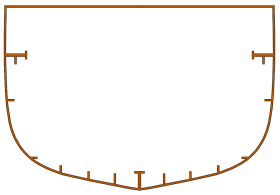

(d) T-glase

Figure 4.2: The midship section of the frigate in full-scale and in model-scale manufactured using three different materials

have an ideal thickness for 3D printing. However, nylon materials are prone to water absorption and their mechanical properties would soon be altered. The Leander-class frigate could not be printed with the available printers with a cross-section that would help prove the concept.

4.2.3 Iteration 3: S-175 containership

Model dimensions and stiffness

As the materials corresponding to the optimal wall thickness for the Leander-class frigate were susceptible to water absorption, a model with decreased flexibility was considered. The S-175 containership not only is much stiffer than the frigate but also an elastic model has been produced in the past [5].

The dimensions of the vessel, in full-scale and model-scale, are summarised in Table 4.1. Coincidentally, the original model was produced using sheets of ABS, the use of which is very widespread in 3D printing. Although the 2 mm wall thickness produced a stiffness 21% higher than the one required by the scaling process, the significant amount of numerical and

Table 4.1: Dimensions of the S-175 containership

Vessel	Dimension	Value	Units
Full scale	L_{BP}	175.00	m
	B	25.40	m
	D	15.40	m
	T	9.50	m
	EI	22.37×10^{12}	Nm^2
Model scale	L_{BP}	3.60	m
	B	0.523	m
	D	0.317	m
	T	0.195	m
	EI	100000*	Nm^2

* Scaled stiffness should have been 82500 Nm^2

experimental results for this vessel renders the precise correspondence to a full-scale vessel unimportant.

Material selection

3D printing of the vessel using the material (ABS) and thickness (2 mm) of the original model was investigated. The relevant cross-section consisted of a simple shell structure without any stiffeners(see Figure 4.3a). The stiffness distribution was calculated with hatch openings in all sections except the fore castle and the accommodation at the aft part of the vessel. It was found to agree well, after rescaling, with that of the full-scale vessel [5] (Figure B.4).

Although the thickness could potentially be achieved by a 3D printer, the apparent simplicity of the geometry was, once more, an obstacle. As ABS has a very high thermal expansion rate, it shrinks significantly as temperature is reduced. Large flat and unsupported areas are discouraged when 3D printing and particularly when using ABS, as they often result in severe warping of the component being printed.

The use of a cellular structure, common in containerships, was proposed. Materials with en elastic modulus equal to or lower than the one of Nylon645 were found to require overly high thickness. The only material capable of producing a cellular structure for this geometry was t-glase, with a wall thickness of 7 mmm, considered ideal to be produced using 3D printing (Figure 4.3b).

The mechanical properties currently available for the various 3D printing materials are provided by the manufacturers and usually correspond to the material before 3D printing. During the printing process, not only do these properties potentially change but also the end product is orthotropic

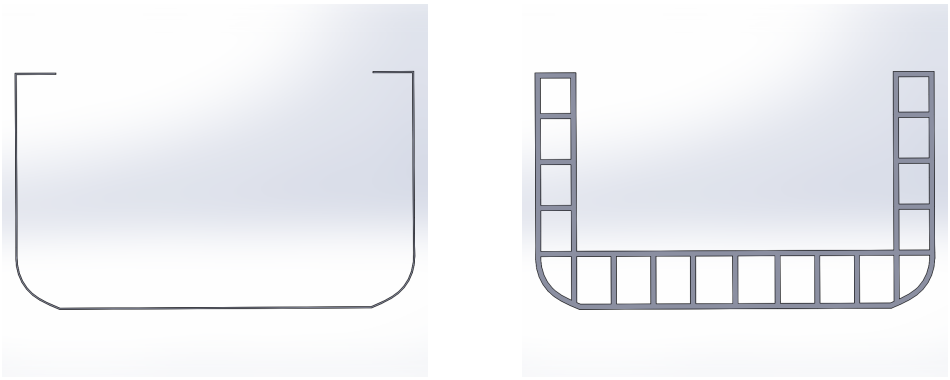

(a) Original [5] (b) Proposed

Figure 4.3: The midship section of the S-175 containership, as manufactured originally and in a variation that would be both easier to print and more representative of the ship structure.

by nature. The directionality of properties is, to some extent, addressed in the literature (e.g. [85]). However, both these publications and the manufacturers' datasheets are based on tensile testing. As the flexural modulus (relevant to bending and, consequently, the current investigation) of thermoplastics can be significantly larger than the tensile modulus, a series of bending tests of 3D printed coupons were carried out.

4.3 Material testing

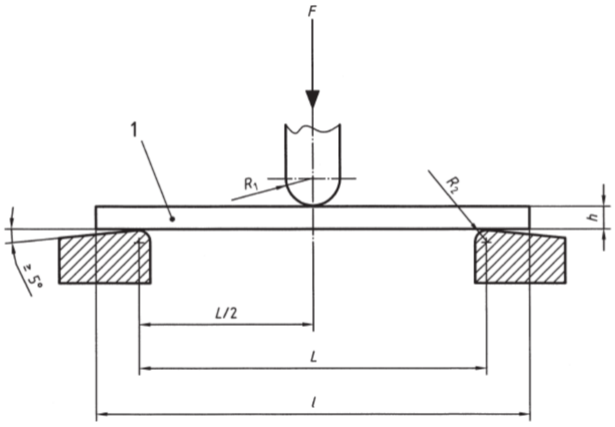

Figure 4.4: 3-point bending test arrangement

4.3.1 Coupon production and measurements

The coupons were designed based on EN ISO 178-2003: Plastics - Determination of flexural properties. A rectangular block geometry was used, with the preferred dimensions equal to 80 mm× 10 mm× 4 mm.

The coupons were produced using two materials and two printers: ABS and T-glase, printing at 260-270° C in an UP box printer and 245-255° C in an UP! Plus 3D printer, respectively. The infill pattern used was cross-hatch at an angle of +45/-45 degrees and a layer thickness of 0.2 mm was selected. Eight different designs were investigated per material. The first four corresponded to the four infill ratios available in the printer's software (not quantified) and were printed with the layers along the thickness. The other four designs only used the two higher infill ratios while layering along the width and the length, respectively. The design numbering was performed in ascending order of infill ratio (1 corresponding to the least dense and 4 to the most dense design). Numbers 5 & 6 and 7 & 8 corresponded to y-axis and x-axis layering, respectively. Six coupons were produced for each design. Table 4.2 summarises the differences between designs.

Table 4.2: Comparison of coupon designs. Layering direction represents the vector that is perpendicular to each of the printing layers: x corresponds to the longitudinal axis of the coupon, y to the transverse and z to the vertical (along the thickness). The design numbers apply to ABS and T-glase alike.

Design	Direction	Infill %
1	z	15
2	z	20
3	z	65
4	z	99
5	y	65
6	y	99
7	x	65
8	x	99

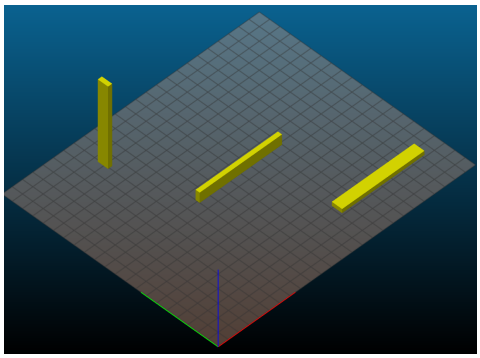

Table 4.3: Orientation of the coupon designs. X, Y and Z axes depicted in red, green and blue, respectively. Layering direction, from left to right: x, y, z.

The dimensions of the coupons were measured using a Mitutoyo Absolute Digimatic caliper with an accuracy of ±0.02 mm. For each coupon, one measurement was taken for the length and three measurements for the width and thickness (along the length). The measurements may be found

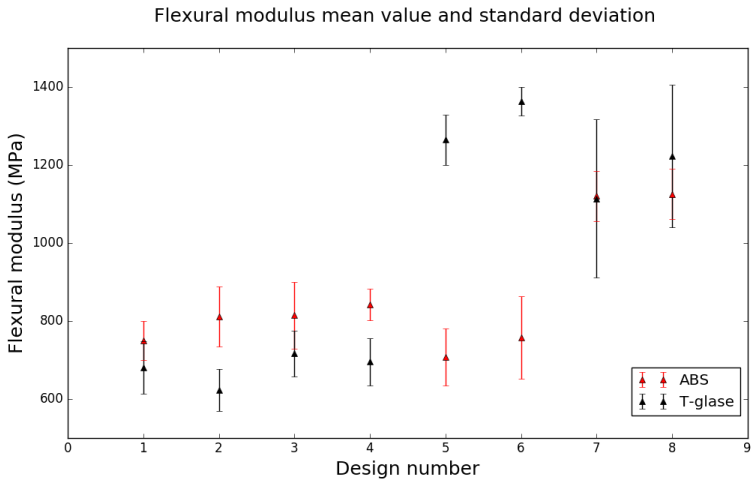

Figure 4.5: Summary of elastic moduli measured, with the respective standard deviation (see also Table 4.2)

in Tables C.1,C.2,C.3,C.4 in Appendix C. The associated errors were, in all cases, within the limits prescribed by the standard.

4.3.2 Test procedure and post-processing of results

The tests were carried out using an INSTRON servo-mechanical testing machine equipped with a bending rig. The radii shown in Figure 4.4 were all equal to 5 mm. The nominal distance between the two centres was equal to 64 mm and the actual distance was measured using the same caliper as for the coupons and was found to be within the prescribed limits (Tables C.1,C.2,C.3,C.4). Measurements of the extension (vertical motion of the central cylinder and load were taken every 0.002 seconds. The testing speed was equal to 5 mm/min.

The noise from the raw output was filtered using a Savitzky-Gaulais filter with a window length of 2001, using 2^{nd} order polynomials. The stress and strain were calculated as for bending of a uniform rectangular beam. The elastic modulus for each test case was calculated as the slope of the stress-strain curve between strains equal to 0.0005 and 0.0025. For each of the designs, the mean value of the elastic modulus and the standard deviation were calculated. Coupons were removed from consideration only when obvious problems or errors occurred during testing.

4.3.3 Results and discussion

Figures C.1,C.2,C.3,C.4 and C.5,C.6,C.7,C.8 depict the Load-extension relationship measured in the experiments for ABS and T-glase, respectively.

The mean values and standard deviation results for all designs are summarised in Figure 4.5. As previously shown for PLA coupons (3.1b), the elastic modulus for ABS increases with infill ratio. T-glase coupons did not produce a clear trend, which can be attributed, among others, to the use of different printers or the fact that the printers are not optimised for it. Ultimate strength was not tested as most coupons did not break for the extension prescribed in the standard.

The coupons may be idealised as a sandwich structure composed of a solid external shell and a honeycomb core. For a layering direction along the z-axis of the coupon, the honeycomb structure's constant section is parallel to to the xy plane. When the coupon is subjected to bending, half of the honeycomb structure is under tension and the other half under compression. At a micro-scale level, it may be assumed that the individual walls of the honeycomb behave as beams in bending as may be seen in Figure 4.6a. It can then be derived [90] that the elastic modulus of the honeycomb should be equal to:

$$E_{honeycomb} = E_{material}\left(\frac{t}{l}\right)^3 \frac{\cos\theta}{(h/l + \sin\theta)\sin^2\theta} \tag{4.1}$$

The geometric parameters the above symbols correspond to may be found in Figure 4.6a. By modelling the external shell as solid with the appropriate thickness and normalising the total stiffness over the stiffness of the external shell alone, we may evaluate the contribution of the core. The results vary for different core densities and they can be expressed as a function of the number of honeycomb cells within the breadth of the coupon (10 mm). The findings are summarised in Figure 4.6b. The approximate integer values for the four levels of infill ratio the UP box printers can produce are depicted with square markers on the curve.

It is evident that, for all four cases, the stiffness of the coupons originates primarily from that of the external shell and changes in infill make a small contribution (less than 10%). In Figure 4.5, the large differences for coupons with a layering direction along the x-axis may be attributed to a) the fact that the honeycomb is then subjected to out-of-plane loading with a completely different behaviour and b) the internal part of the coupon for such a thin layer section results in a much fuller core than would normally be expected. As will be seen later, for a reduced thickness of 2.5 mm, the core of the print is practically 100% full (Figure 5.1).

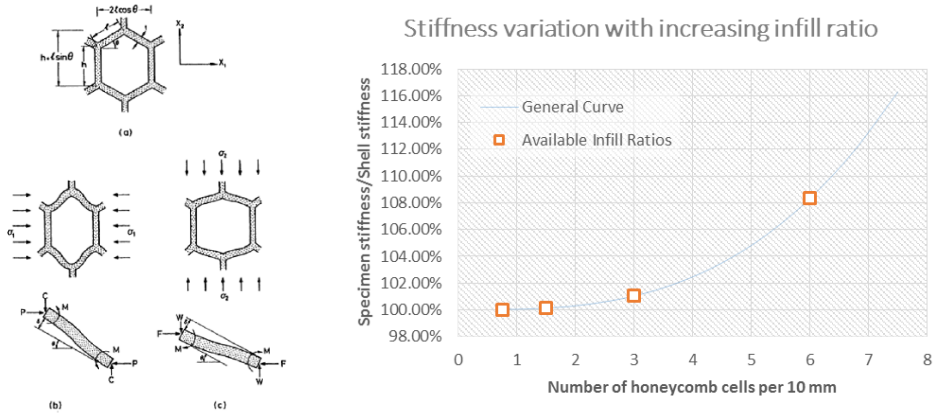

(a) Cell deformation [90]

(b) Stiffness variation

Figure 4.6: The coupons were modelled as a sandwich structure with a solid external shell and honeycomb core (Equation 4.1). The curve depicts the stiffness of the coupon with increasing infill ratio. The orange box markers correspond to coupon types 1, 2, 3 and 4 (Table 4.2).

4.4 Manufacturing challenges and design reiteration

The mechanical tests for T-glase indicated much higher properties than anticipated. Furthermore, it was found that the UP box printers struggled to produce large print with this material, being optimised for use with either ABS or PLA. The above resulted in the S-175 concept being abandoned until a more flexible material became available.

It was concluded that the depiction of a real vessel was, at this point, beyond the scope of the investigation, which is proof-of-concept. It was decided to combine the best traits of the Malenica barge and the S-175 container ship into a new model. A rectangular barge with a constant cross-section inspired by a container ship is a model allowing hydroelastic testing of a complex 3D printed section while minimising design complexity. The bending stiffness of the vessel does not need to be realistic as long as it is measurable and its effects can be evaluated.

4.5 Final design: Container ship-inspired cellular barge

4.5.1 Vessel design

The volumetric capabilities of the printer largely determined the scale used for the vessel. A minimal number of sections was desired due to the uncertain effects of section joining on the dynamic properties of the model. For the same reasons, it was decided that the cross-section should fit in the build volume of the printer without any transverse division. The resulting

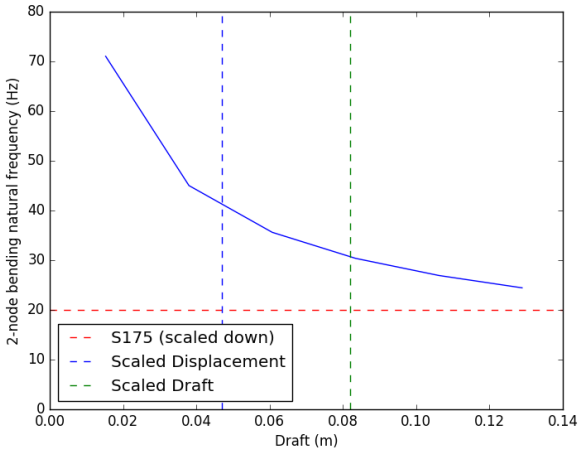

Figure 4.7: Predicted natural frequency as a function of the draft. The two vertical lines correspond to Froude scaling of the displacement or the draft of the vessel (different due to change in block coefficient). Natural frequency calculation is based on the flexural modulus derived from the 3-point bending tests.

maximum breadth of 22 cm was used to define the ratio λ_m between the S-175 model [5] and the barge (for general particulars). All dimensions were then derived by Froude scaling, with the exceptions of the draft and, of course, the stiffness.

A draft directly scaled by λ_m would not produce the appropriately scaled displacement due to the significant increase in block coefficient moving from a slender ship to the barge. The required draft was instead derived by scaling the displacement of the model by λ_m^3. It should be emphasised that λ_m is the scaling factor between the two models and not between the model and the full-scale vessel. As may be seen in Figure 4.7, even if the draft was scaled linearly it would not be feasible to achieve the natural frequency of the S-175. The only alternative would be to produce a longer vessel to reduce the natural frequency, but that would mean that the principal particulars of the vessel would not be Froude scaled. Furthermore, the necessary increase in length would significantly increase manufacturing time. Since the natural frequency of the vessel would be too high to become directly excited in the towing tank either way, it was decided that Froude scaling of the main particulars of the vessel and scaling of the displacement was the best option.

The principal particulars for the vessel may be found in Table 4.4.

Table 4.4: Principal particulars of the cellular barge.

Dimension	S-175	Cellular barge	Units
L (Length between perpendiculars)	3.600	1.520	m
B (Beam)	0.523	0.220	m
D (Depth)	0.317	0.130	m
T (Draft)	0.195	0.047	m
Δ (Displacement)	215.40	16.21	kg
C_B (Block Coefficient)	0.5787	1.0000	-
λ (Scale factor)	48.6	115.1	-
f_{2n} (expected nat. freq. in air)	8.57	41	Hz

4.5.2 Vessel production

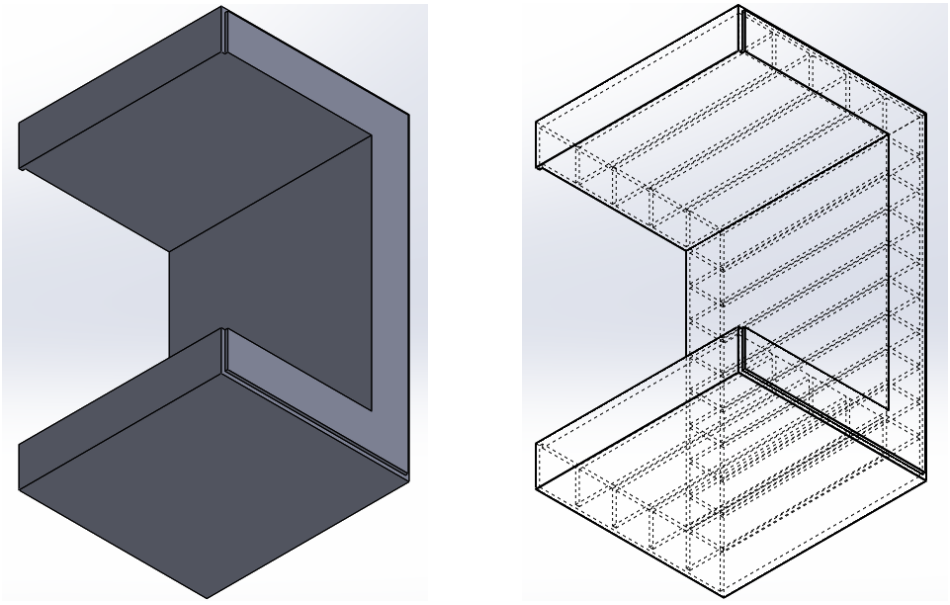

(a) Section (shaded) (b) Section (X-ray)

Figure 4.8: CAD representation of one of the sections of the model. The deep frame (including a slot to allow easy assembly) is clearly visible in (a), whereas the internal cellular geomery is shown in (b).

The vessel was produced using an UP box printer. A uniform thickness of 2.5 mm was used for all longitudinal parts of the structure, which was considered to be very close the minimum thickness the UP box could print with reasonable accuracy. The size of the deck openings was based on the S-175 container ship and the cellular arrangement was inspired by real container ships. Each section (total of 11) was built with the longitu-

dinal axis of the vessel coinciding with the z-axis (the layering direction) of the printer. A 4 mm deep frame marked the start of each section, and appropriate slots at the beginning and end of each section ensured that this thickness was shared equally between two subsequent sections (Figure 4.8). The remaining middle part of the section was prismatic. It was found that at the thickness of 2.5 mm and for walls perpendicular to the printed bed, the resulting infill of the section was practically 100% and the top layer was almost identical to the internal layers (see also Figure 5.1). 10 of the sections were printed with a length of 140 mm whereas the fore section had a length of 120 mm to achieve the required length of 1.52 m.

Figure 4.9: The sections would peel off the print bed and their bottom surface would be distorted, resulting in gaps in the connections.

The sections were joined using an ABS paste made with scrap pieces of the parent material dissolved in acetone. The large size of the prints combined with the high thermal expansion rate of ABS resulted in slight peeling of the corners of the section off the print bed and subsequent curving of the bottom of the print. This was resolved by application of the aforementioned paste to fill the gaps during the joining process. As the longitudinal parts of the cross section were practically 100% full of material and the paste solidifies into ABS after acetone evaporates, this practice intended to produce similar properties and ensure longitudinal continuity. The vessel was sanded and spray-painted to further improve smoothness and watertight behaviour. A series of bulkheads were added at the same locations as the deep frames, excluding three deep frames around sections 10 and 12, where their installation was impossible because of the presence of the tow post and the midship section strain gauges.

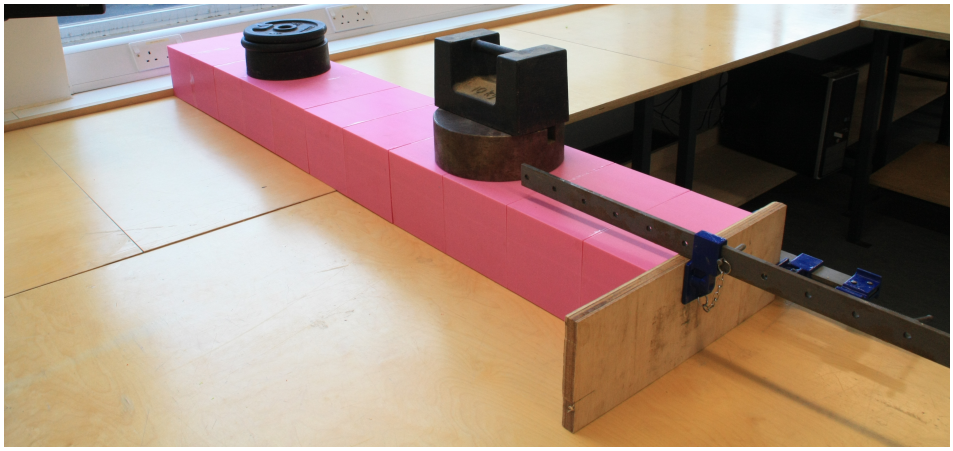

Figure 4.10: Long sash clamps were used for the joining of the model and masses were applied to minimise buckling

4.6 Estimation of uncertainty of cross-sectional properties

Measurements of the dimensions and wall thickness of each of the sections comprising the model may be found in Figure D.1. It was observed that uncertainties were much more pronounced for thickness as opposed to larger dimensions. In most cases, thickness average was found to be ± 10-20% different from the nominal but with a standard deviation of 1.6-4.3% of the average value based on a normal distribution. The maximum values for error and standard deviation for the larger dimensions were 1.08% and 0.38%, respectively. It was concluded that the second moment of area should not deviate significantly from nominal, depending primarily on the distance of the various sections from the neutral axis rather than the relevant thickness (main contribution comes from $A \times \delta z_{NA}^2$, i.e. length×thickness×length^2). The final length of the vessel was found to be 1.525 m, which results in an error of 0.3% compared to the nominal length.

The mean values and standard deviation of various dimensional measurements of the cross section were used as an input to a Monte-Carlo simulation to evaluate the uncertainty over cross-sectional properties. A population of 10000 randomly-generated cross sections was used and results were found to converge after approximately 1000 sections. A summary of the results can be found in Table 4.5. It was concluded that the variation of cross-sectional properties is not large enough to affect the estimation of vibratory properties of the vessel.

Table 4.5: Statistical predictions for the cross-sectional properties of the vessel, based on dimensional measurements and use of a Monte-Carlo simulation.

Property	Symbol	Mean	SD
Cross-sectional Area (m^2)	A	3.72E-03	3.70E-05
2^{nd} Moment of Area (m^4)	I_{yy}	6.10E-06	6.16E-08
Transverse location of centroid(m)	y_c	8.10E-4	4.94E-05
Vertical location of centroid(m)	z_c	4.59E-02	3.33E-04

4.7 Summary and discussion

Initial ideas regarding potential vessels to be modelled as elastic focused on vessels for which experimental and numerical data can be found in abundance. Evaluation of the various options revealed several constraints. Some were related to the manufacturing technology (e.g. maximum build volume, minimum thickness) but others were more relevant to the nature of the concept: the structure needs to be sufficiently detailed, resembling a ship and featuring consistent dimensions (unlike the thickness of the frigate wall, which was similar to stiffener breadth, see Figure 4.2b).

It was decided that the cross-section could be constant, as the hydrodynamic properties of the model were not the focus of this project, resulting in a rectangular barge geometry. The general particulars of the S-175 container ship were used, at a smaller scale than previous investigations. Due to material an thickness constraints, the bending stiffness of the model would be higher than that of the original vessel but that was not considered an issue as the 2-node bending natural frequency was too high to be directly excited by waves anyway.

The vessel was manufactured in sections along the length, using ABS as the material. The thickness of longitudinal elements was found quite increased compared to design, although the deviation between different locations was relatively small. This was attributed to the printer operating very close to its minimum thickness limits. The sections were joined using ABS dissolved in acetone. An acrylic coating was applied to improve watertight behaviour.

Chapter 5

Methods for improved prediction of 3D printed model properties

5.1 Natural frequency discrepancies and need for improved design procedure

Preliminary hammer tests in air were performed to determine the vibratory properties of the vessel, which was suspended to emulate free-free boundary condition. The set-up consisted of an accelerometer, which was installed on the model at a non-nodal location and an instrumented hammer. Point impact excitation was applied on the model using the hammer and the levels of both excitation and response were measured. The frequency response functions, natural frequencies and mode shapes of the model were calculated through this process. Further details on the relevant set-up and procedure are presented in the following two chapters, where the results of these tests are discussed in more detail.

The measured dry 2-node bending natural frequency was 53 Hz, whereas it was expected to be 44 Hz, resulting in a difference of approximately 20%. Estimation of the natural frequency was based on the average value derived by the 3-point bending tests (Design 8 from Figure 4.5) combined with geometric measurements throughout the vessel (to determine the actual sectional properties) and Timoshenko beam approximation. As discussed in Chapter 3, scaling of the natural frequencies is an essential part of the general scaling process and large discrepancies can render the results irrelevant to the full-scale vessel. Although no real vessel was used for the purposes of this investigation, it stands to reason that accurate prediction of the vibratory properties of the model is absolutely necessary for the concept to be useful. In this chapter, a specimen-scale testing procedure is developed to ensure that the design process satisfies the above criteria.

5.2 Possible sources of natural frequency prediction errors

As the mass distribution of the model was easily measurable, the difference would necessarily originate from the bending stiffness. However, the rigorous measurements of the various dimensions of the cross sections, discussed in the previous chapter, left little room for error regarding the cross-sectional area or the second moment of area. The differences were, consequently, attributed to the methods used to identify the flexural modulus.

Part of the issue certainly originated from the dissimilarity between the thickness of the previously used bending coupons and that of the model's walls (see relevant calculations in 4.3.3). As print thickness becomes smaller and approaches the operational limits of the printer, deposition of the infill between the external shells becomes increasingly challenging and may result in a virtually solid print (see Figure 5.1). Further to that, however, the coupon geometry and/or the loading conditions could have affected the accuracy of the results. Firstly, the solid rectangular cross section of the coupons did not resemble, in any way, the cellular shape of the cross section of the model. Additionally, due the viscoelastic nature of polymers, even when considering "rigid" plastics, the dynamic flexural modulus can be different from the static one. It is generally recommended that the nature of the tests to identify material properties is determined based on the loads on the structure (i.e. dynamic tests for vibrating structures, static tests for statically-loaded structures) [8].

The accurate prediction of at least the 2-node bending natural frequency of the model is essential for this concept to be useful. It was, thus, imperative to develop a testing procedure, to be used during the design of the model, which is capable of accurately predicting the dynamic properties of such structures. To identify the extent to which the aforementioned error sources actually contribute to the encountered discrepancies in the natural frequency, a series of tests had to be performed. For this purpose, specimens with a cellular (box-shaped) cross section would be tested, both in dynamic and static conditions.

A range of different specimen types, combined with a series of modelling techniques, was selected to allow a thorough understanding of their dynamic behaviour through the following process:

- establish (by comparing to shell modelling predictions) whether the vibrating specimens may be modelled using a beam approximation to derive the dynamic flexural modulus of the material from the 2-node bending natural frequency
- assess the suitability of the Euler beam method (as opposed to Timoshenko beam theory) depending on the length of the specimens and the importance of shear effects when calculating the aforementioned frequency

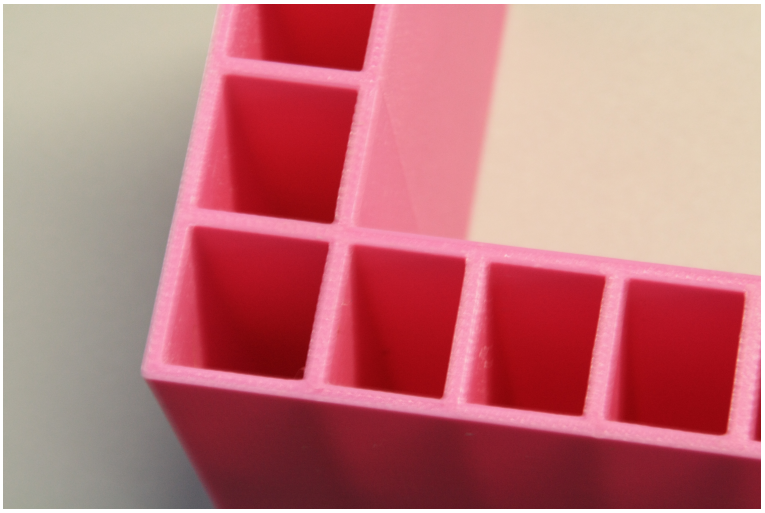

Figure 5.1: Photo of a half-printed section demonstrates how the inside of the walls is virtually solid.

- investigate whether the inclusion of transverse bulkheads alters, in any way, the accuracy of these approximations.
- compare the produced values for the flexural modulus, from measured responses in quasi-static and dynamic conditions.
- use the produced values for flexural modulus and shear modulus (or Poisson's ratio) in the vessel modelling (see 5.5.2).
- compare the resulting predictions for the vessel dry frequencies to the experimentally measured values.

The resulting data was used to assess the capabilities of the specimen-scale experimental procedure to predict the vibration properties of the elastic model. To simplify the modelling and reduce the level of uncertainty, the properties of the unballasted hull in vacuo were used for the assessment.

It should be emphasised that, as will be seen later in this chapter in more detail, a number of assumptions and approximations were taken to simplify the process. For example, the material was in all cases modelled as isotropic, despite the layered nature of the printing process. Furthermore, the joining between different sections of the specimens/vessel was not modelled - that is, they were modelled as continuous. Finally, the storage and loss moduli of the material were not calculated and an "effective" value for the dynamic modulus was calculated instead.

The reasoning behind all the aforementioned assumptions was that doing otherwise would significantly increase the complexity of the modelling and the number of different tests needed to acquire all the relevant material properties (flexural moduli in three directions, storage and loss mod-

uli). The above would be a full material characterisation which, although it would provide precise information about the material behaviour, would not necessarily be relevant to the design of a scaled model for the investigation of structural vibrations. Consequently, this chapter explores the extent of assumptions that can be taken to create the simplest possible process for future investigators without making compromises on the accuracy of properties relevant to structural vibrations, namely the natural frequencies and damping ratios.

5.3 Cellular specimen production

For the purposes of this investigation, specimens of a constant, hollow rectangular cross section were manufactured using 3D printing. ABS was printed with an infill ratio of 99%, resulting in almost entirely solid structure. The layering direction was the same for all specimens and parallel to their longitudinal axis, so that the layer planes were parallel to the cross section. Specimens of four different lengths were manufactured, namely 180 mm, 260 mm, 390 mm and 520 mm. Details regarding the cross section are summarised in Table 5.1.

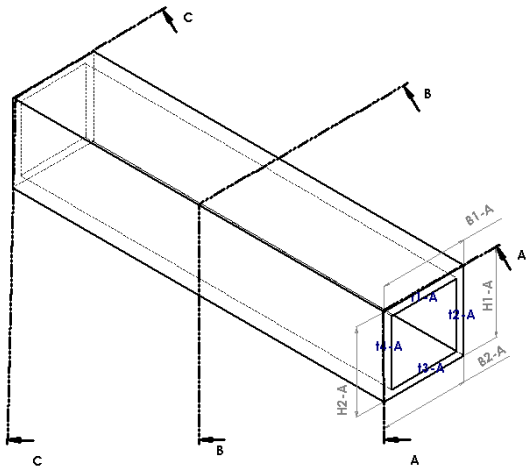

Figure 5.2: Depiction of the measurement points for each specimen segment. A, B and C denote the 3 sections where measurements were obtained. H, B and t represent measurements of height, breadth and thickness, respectively. No thickness measurements were obtained at the midpoint.

In the case of 180 mm specimens, both a continuous version and a version of two equal segments joined in the middle were produced. The remaining specimens were all produced in segments of 130 mm. In all cases, the segments were joined together using a solution of ABS (the same as the

one used for printing) in acetone. The segments were constrained together using sash clamps while the acetone was evaporating to leave just ABS in the area of connection. An alternative version of the 260 mm specimens, including bulkheads at the ends and the middle of the specimen, was also produced. A summary of all specimen designs is presented in Table 5.2.

Extensive measurements were taken on each specimen segment prior to joining. Four thickness measurements, two breadth measurements and two height measurements were taken on each end of the segment. Two additional breadth and height measurements were taken at the midpoint of each specimen. The measurement points are depicted in Figure 5.2. The measurements were used to calculate the cross-sectional area and second moment of area at different points of each specimen. An average value was then used for each of the specimens.

Table 5.1: Specimen cross section details, with mean and standard deviation calculated for the entire population of specimens, rather than each specimen type separately (see Table 5.2).

Dimension	Symbol	Mean	SD
Breadth (m)	B	0.0280	9.88E-05
Height (m)	H	0.0273	7.62E-05
Thickness (m)	t	2.67E-03	6.31E-05
Cross-sectional Area (m^2)	A	2.68E-04	1.40E-06
2^{nd} Moment of Area (m^4)	I_{yy}	2.76E-08	1.52E-10
Mass/ Unit Length (kg/m)	μ	0.2622	0.0067

Table 5.2: Specimen type length, number of segments, number of specimens tested and number of test points used per specimen.

Specimen Type	L (m)		Number of Segments	Number of Specimens	Test Points
	Mean	SD			
A*	0.180		1	5	3
B	0.180	1.21E-04	2	5	3
C	0.256	1.00E-04	2	6	5
D†	0.260	9.77E-05	2	5	5
E	0.390	4.41E-04	3	5	8
F	0.520	1.45E-04	4	3	11

* Only nominal length available
† Including transverse bulkheads

Table 5.3: Specimen type measured 2-node bending natural frequency (dynamic tests) and measured difference in load values corresponding to strains of 0.0025 and 0.0005 (3-point bending tests).

Specimen Type	f_{2-node} (Hz)		$\Delta F_{\epsilon=0.0005,0.0025}$ (N)	
	Mean	SD	Mean	SD
A	1372.47	22.43	124.82	6.75
B	1381.53	9.52	93.51	17.67
C	737.17	7.72	99.90	21.71
D†	678.60	3.33	109.65	5.58
E	340.46	2.93		
F	194.33	0.90		

† Including transverse bulkheads

5.4 Experiments

5.4.1 Specimen dry vibration

The specimens were subjected to modal testing with both ends treated as free supports. They were tethered using flexible bands at the nodal locations of the 2-node bending mode, to minimise the influence of support on the aforementioned mode [91], which was the main focus of the investigation. The roving hammer setup used a PCB-086E80 instrumented hammer (sensitivity: (±20%) 22.5 mV/N) for the excitation measurement and a PCB-352C22 accelerometer (sensitivity: (±15%) 1.014 mV/(m/s^2), frequency range: (±5%) 1.0 to 10000 Hz), located at one of the free ends of the specimen, for the response measurement. Both measurements were obtained using a DataPhysics Quattro Dynamic Signal Analyzer and SignalCalc software and the latter was also used for the calculation of the relevant frequency response functions.

5 specimens were tested for most specimen types (with two exceptions) and the number of test points increased with the length of the specimen. Details about numbers of specimens and test points,which were approximately evenly distributed along the length, are found in Table 5.2. For each test point, the test was repeated thrice, the frequency response function was calculated for each repetition and an average was produced. The measured frequency range was between 0 and 2000 Hz (at a 0.5 Hz step), thus including the 2-node bending natural frequency for all lengths (see Table 5.2), and higher natural frequencies for the longer specimens.

3 specimens of specimen type B (390 mm long) were also tested in torsion to identify the shear modulus. For the purposes of this investigation, two accelerometers were used, installed on the top and side wall of the specimen. Both accelerometers were installed at one of the two-node bending mode nodes, to minimise the effects of 2-node bending on the response (see Figure 5.3). A vertical impact excitation was applied, this time at points off the centreline and at the opposite side (transversely) from the accelerometers. The same test points along the length of the specimen as in vertical excitation cases were used.

5.4.2 Specimen 3-point bending

The shorter specimen types (A, B, C, D) were also subjected to 3-point bending tests. A servo-mechanical INSTRON testing machine was used for this purpose. Specimen types E and F were not subjected to this type of testing due to maximum length restrictions. The specimens were supported by two circular rollers at 10% of the length from either end. Both rollers had a diameter of 10 mm. A third roller of the same size applied a displacement at the midpoint of the specimen, descending at a speed of 2 mm/min. All

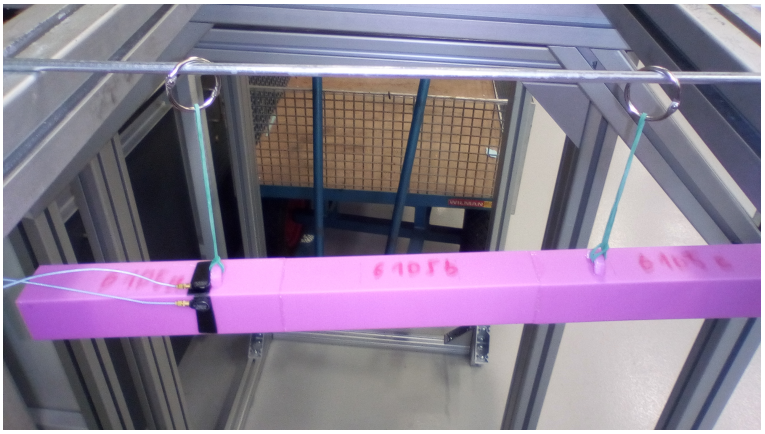

Figure 5.3: Specimens were tested in antisymmetric vibration using two accelerometers, in the transverse and vertical direction, respectively.

the above parameters were based on the standard for the determination of flexural properties of plastics [92].

5.4.3 Comparison to standardised procedures

Both the experimental procedure and the post-processing method described for dynamic tests follow the relevant ASTM standard [93], with an increased number of measurement points. For static tests, this method was substituted by the procedure described in the relevant ISO Standard [92]. In this procedure, an Euler-Bernoulli beam approximation is assumed to calculate the modulus using the measurement points corresponding to strains of 0.0005 and 0.0025. In both types of tests, minor adjustments were made in the post-processing of results to account for differences in the specimen geometry compared to what is prescribed.

5.4.4 Unballasted model dry vibration

The model was also subjected to modal testing at a free support condition. It was tethered using bungee cords at stations 6 and 14, as due to spacial constraints in the experimental setup it was not possible to tether it exactly at the 2-node vertical bending mode nodes (namely stations 5 and 15). The roving hammer setup used a PCB-086C03 instrumented hammer (sensitivity: ($\pm$15%) 11.2 mV/N) with a hard plastic tip (white) for the excitation measurement and three PCB-352C22 accelerometers (sensitivity: ($\pm$15%) 1.019 mV/(m/s^2), 0.998 mV/(m/s^2) and 1.003 mV/(m/s^2), respectively) for the response measurement.

The accelerometers were located at station 19 of the model on the starboard side. Two of them were installed on the inner side to measure along

the Y-axis. This setup was selected so that further post-processing of the measurements would allow the calculation of translational and rotational acceleration at the midpoint [12]. The vertical locations of these accelerometers (z=0.031 and 0.059 from the keel, respectively) were selected so that the midpoint coincides with the vertical location of the centroid of the cross-section. The third accelerometer was placed on the main deck to measure along the Z-axis.

All measurements were obtained using a DataPhysics Quattro acquisition system and SignalCalc software and the latter was also used for the calculation of the relevant frequency response functions. For each measurement point, the test was repeated thrice, the frequency response function was calculated for each repetition and an average was produced. The measured frequency range was between 0 and 400 Hz (at a 0.5 Hz step).

The model testing was split into two phases. In the first one, the model was excited horizontally. The excitation points were located at each station (so every 5% of the model length), starting at station 1 and ending at station 19. For all stations, the excitation point was located at the side wall of the model and exactly below the main deck. Measurements were obtained on both the port and the starboard side.

In the second phase, the model was excited vertically. The excitation points were located at the midpoint of the main deck, both for port and starboard side. In this case, not all stations could be excited due to the presence of strain gauges in some of them. Namely, stations 1, 2, 3, 6, 8, 11, 13, 14, 16, 17 and 19 were excited on both sides of the vessel.

5.5 Mathematical modelling

5.5.1 Specimen modelling

The specimen structure was then modelled using a number of different methods to investigate their validity for each specimen type. All values, including geometrical aspects, mass and experimental measurements (natural frequency, quasi-static extension & load) were averaged per specimen type for the purposes of these calculations.

As all the specimens, with the exception of specimen type D which included bulkheads, featured a uniform cross section and uniform mass distribution, the dynamic flexural modulus may be calculated with an Euler beam approximation, namely:

$$\omega_{2-node} = \frac{4.73^2}{L^2}\sqrt{\frac{EI}{\mu}} \tag{5.1}$$

where L is the specimen length, E the flexural modulus, I the 2$^{\text{nd}}$ moment of area and μ the mass per unit length.

The second modelling method used a Timoshenko beam approach (element BEAM188 in ANSYS), whereas the third method employed a fully 3D FEA approach with shell elements including both membrane and bending loads (element SHELL181 in ANSYS). In all cases, an iterative process was followed to identify the flexural modulus E that resulted in the natural frequencies measured during the experiments. In all cases, lines were meshed with a maximum element length of 0.0009 m; that is to say, an element size of 0.0009 was used along all axes. Convergence for this mesh is demonstrated in Figure E.1 in the appendices. The eigenvalue problem of the specimen with free-free boundary conditions was solved to compare to dynamic tests. The specimens were also modelled with roller support and a single applied deflection and the results were compared to the 3-point bending tests.

5.5.2 Vessel modelling

The vessel was modelled using element SHELL181.The cross section was designed in 2D and extruded, and the transverse bulkheads and deep frames were also included. In all cases, lines were meshed with a maximum element length of 0.01 m. Convergence for this mesh is demonstrated in Figure E.1 in the appendices.

5.6 Results

5.6.1 Specimen modal tests

The average 2-node vertical bending (or 1-node twisting, where appropriate) natural frequencies for the various specimen types are given in Table **??**. Differences in natural frequencies between specimen types A and B, which only differ in terms of presence or absence of joining, were limited. More significant difference was observed between specimen types C and D, which have the same length but transverse bulkheads were included in the latter. Although the bulkheads don't affect the longitudinal stiffness, they act as point masses at the local extrema of the 2-node bending mode shape (free ends and midpoint).

A summary of the dynamic flexural modulus required to match the measured natural frequency for each structural model is shown in Figure 5.4. It was observed that the shell element model provides a consistent estimation of the dynamic flexural modulus (2.155 MPa with a standard deviation of 0.8%) over all specimen types. As this model includes both shear deformation effects in bending and section warping, it was considered the most general model and was used as a baseline.

Estimations using the Timoshenko beam model were fairly close to the shell estimations (maximum difference of 3.5%) for most specimens, with

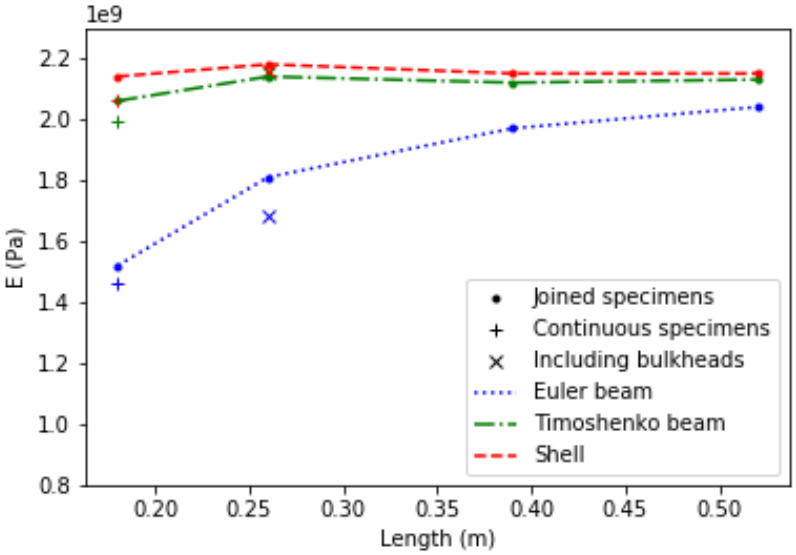

Figure 5.4: Dynamic flexural modulus of the specimens, derived from the 2-node bending natural frequency using three different structural models, as a function of specimen length. Lines (dot markers) depict specimens with no bulkheads, produced by joining a number of segments (see Table 5.2). + markers depict specimens without any joining, whereas x markers depict specimens including bulkheads.

the difference between the two increasing as specimens became shorter. This difference was attributed to warping of the cross section. Warping became less apparent in longer specimens and from type C onwards the dynamic flexural modulus calculated using the Timoshenko beam approximation was different from the one produced with shell modelling by only 0.9%.

Estimations based on the Euler-Bernoulli beam approximation diverged much more significantly for shorter specimens. For the more slender specimens with a length of 520 mm the difference in calculated modulus from the shell element estimation was of the order of 5%. However, the difference rapidly increased with decreasing length, reaching 40% for the 180 mm specimens. It was evident that, for this scale of specimens, the 2-node bending natural frequency was significantly affected by shear deformation effects. Use of the Euler-Bernoulli beam approximation would only be recommended for the 520 mm specimens. This corresponded to a length/height ratio of 19, which was close to the ratio of 20 recommended by the standards (for beams with a rectangular rather than box-shaped cross section) [93] to use the Euler beam approximation.

The continuous specimens (i.e. specimen type A) showed similar trends to the joined beams regarding the accuracy of the various approximations. When compared to specimen type B, comprising two segments, a slight increase in stiffness was observed, the magnitude of which was, however, comparable to the standard deviation of the measurement. As a result, there was no clear evidence of joining having any effects on the dynamic responses. The presence of bulkheads in specimen type D had two distinct effects. Firstly, the difference of the Euler beam results when compared to specimen type C signified the importance of the mass distribution when calculating the natural frequency of these structures. Secondly, being the only specimen type where the Timoshenko beam and shell models coincided, it was emphasised that bulkheads prevent any deflection of the cross section and result in a structure that can be described just as well using a beam approximation.

Measurements from antisymmetric testing of type E specimens produced an average 1-node twisting natural frequency of 1067.17 Hz with a standard deviation of 7.97 Hz. Using the same iterative method as before, BEAM188 and SHELL181 elements produced a shear modulus of 841 MPa and 881 MPa and a Poisson's ratio of 0.26 and 0.22, respectively.

5.6.2 Specimen 3-point bending tests

Results from the 3-point bending tests are shown in Figure 5.5. It can be observed that the trends for these quasi-static tests resembles the one previously discussed for the dynamic tests. The shell model suggests more consistent results for all specimen types tested, with the Timoshenko beam approximation slightly closer to these values for longer specimens and the Euler beam approximation having significantly larger differences. It is also demonstrated that the quasi-static flexural modulus is approximately 35% lower than its dynamic counterpart. It may be concluded that identification of the quasi-static modulus would not be sufficient for the modelling of 3D printed structures which are subjected to dynamic loads.

The presence of bulkheads was found once more to restrict warping of the cross section and result in a specimen behaving more in a beam-like manner. As can be seen in Figure 5.5 the Timoshenko beam and shell approximations produced almost identical results (x-shaped markers). On the other hand, continuous specimens were found to produce responses indicating higher stiffness than the joined ones, contrary to what was found in vibration tests. Differences between the measured static and dynamic elastic modulus may be partly attributed to the viscoelastic nature of ABS. Furthermore, the experimental uncertainties associated with quasi-static and dynamic tests can be quite different, as illustrated by the mean and standard deviation values in Table 5.2, due to both the way the measurements are obtained and the nature of the physical problem investigated

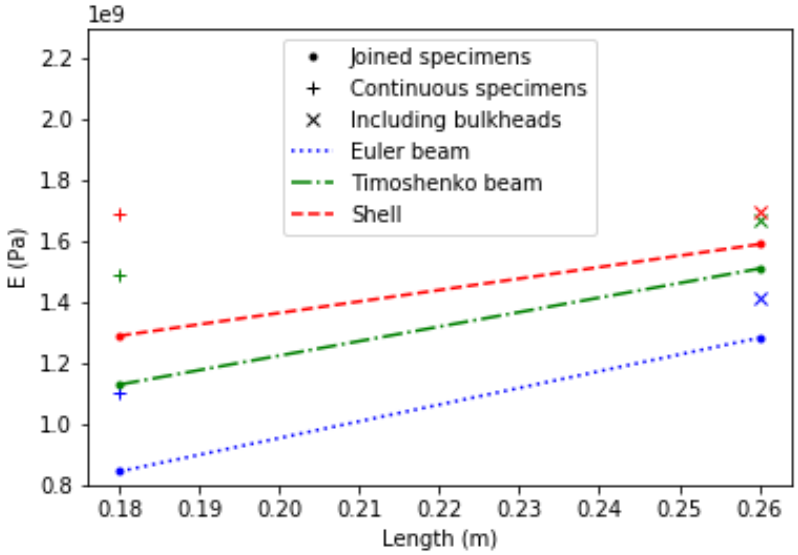

Figure 5.5: Quasi-static flexural modulus of the specimens, derived from the load-displacement curves using three different structural models, as a function of specimen length. Lines (dot markers) depict specimens with no bulkheads, produced by joining a number of segments (see Table 5.2). + markers depict specimens without any joining, whereas x markers depict specimens including bulkheads.

(load-deflection relationship or structural eigenvalue problem).

5.6.3 Vessel modal tests

The values for the dynamic flexural modulus (specimen type F) and dynamic shear modulus (specimen type E) obtained from the specimen tests were used as input for the ANSYS simulations of the vessel. As the shear modulus and corresponding Poisson's ratio were found to be different for beam modelling and shell modelling for the specimens, values obtained from shell modelling were used. A comparison between the vessel's natural frequencies, as predicted by ANSYS and as measured experimentally is presented in Table 5.4.

The mode shapes calculated in ANSYS can be found in Figures 5.6, 5.8, 5.10, 5.12, 5.13, 5.15 and 5.16. The corresponding operating deflections shapes (ODS) measured in the experiments can be found in Figures 5.7, 5.9, 5.11, 5.14 and 5.17. The ODS were not normalised and the values on the vertical axis of the graphs correspond to the imaginary part of the acceleration frequency response function, thus they are measured in $(m/s^2)/N$ (translation) or $(rad/s^2)/N$ (rotation).

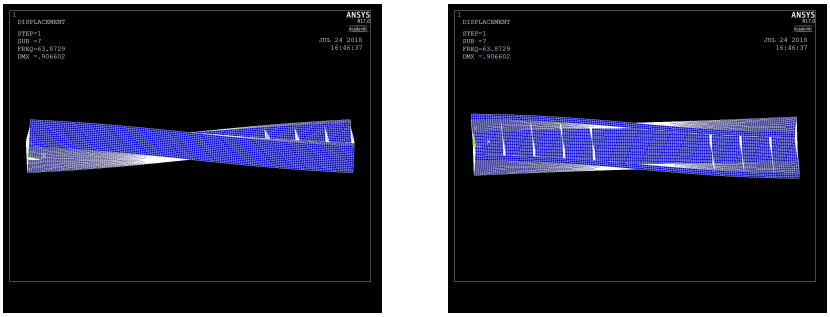

(a) Side (b) Top

Figure 5.6: 1-node horizontal bending - 1 node twisting mode, as predicted by shell modelling (natural frequency of 63.9 Hz)

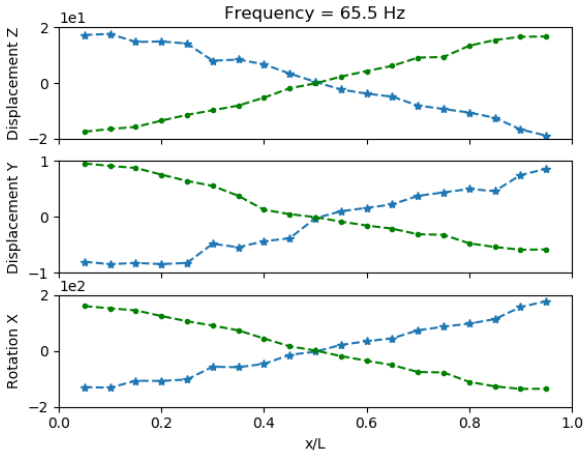

Figure 5.7: The measured ODS corresponding to the 1-node horizontal bending - 1-node twisting mode. Green point markers and blue star markers indicate port and starboard excitation, respectively.

Mode shapes beyond the 4-node horizontal bending - 4 node twisting mode, although calculated in ANSYS, were not included here for a number of reasons. Firstly, because no modes further than that could be identified from the modal tests. Secondly, because the "global" mode shapes get increasingly contaminated by "local" mode shapes including, for example, bulkhead deflection. bottom deflection or deflection of the (unsupported by bulkheads) section around the tow post. Some of these localised responses are already visible in the 3-node vertical bending mode (Figure 5.13) but become more pronounced with increasing mode order. Finally, higher order twisting modes are unlikely to get excited during ship operation and, as a result, would not be relevant for this application.

As shown in Figures 5.7, 5.9, 5.11, 5.14 and 5.17, the operating de-

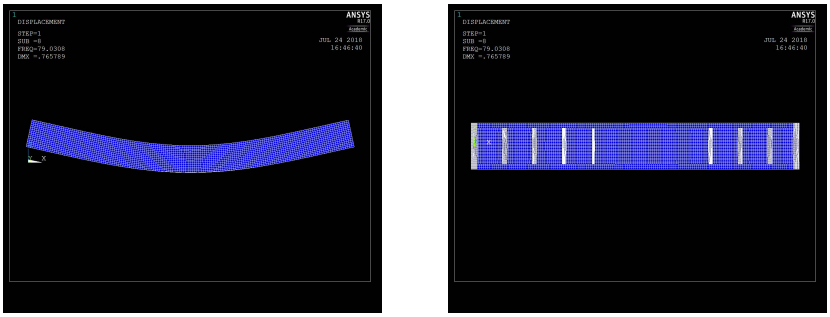

(a) Side (b) Top

Figure 5.8: 2-node vertical bending mode, as predicted by shell modelling (natural frequency of 79.0 Hz)

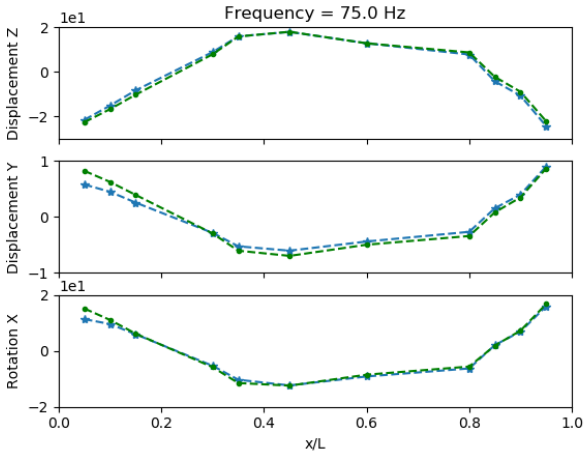

Figure 5.9: The measured ODS corresponding to the 2-node vertical bending. Green point markers and blue star markers indicate port and starboard excitation, respectively.

flection shapes (ODS) corresponding to the various mode shapes were calculated separately for port and starboard excitation. In most cases, the operating deflection shapes resulting from the two excitation sides have opposite phase. In the case of horizontal excitation, this resulted from the fact that the impact was applied with a direction from the side wall towards the centreline, resulting in opposite excitation directions. The results from vertical excitation are not presented as they were almost identical; in this case, opposite phases are explained based on the the antisymmetric nature of this modes. The only occasion where the port and starboard side were in phase was the 2-node vertical bending ODS (Figure 5.9). The second symmetric mode (3-node vertical bending) is located very close to the 3-node horizontal bending - 3-node twisting mode, resulting in an operating

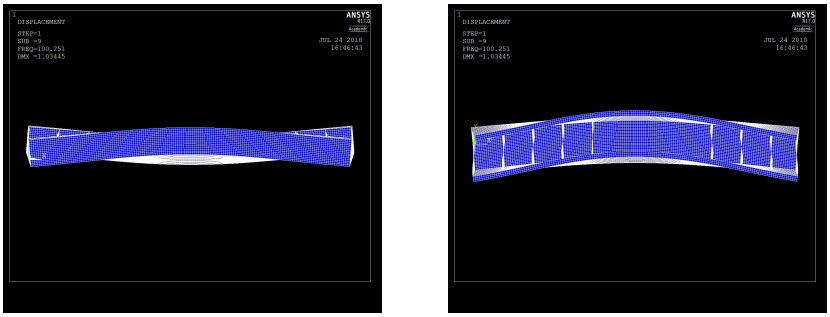

(a) Side (b) Top

Figure 5.10: 2-node horizontal bending - 2 node twisting mode, as predicted by shell modelling (natural frequency of 100.2 Hz)

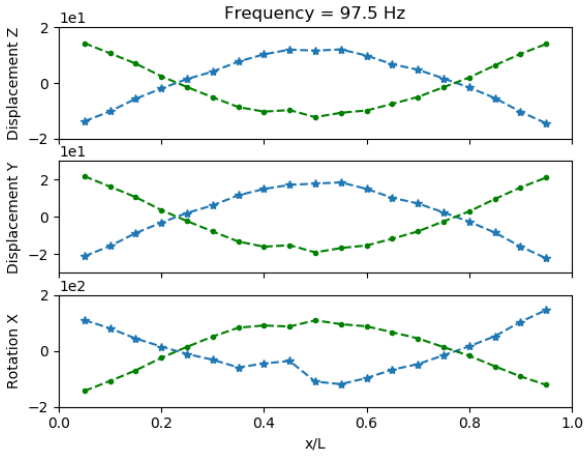

Figure 5.11: The measured ODS corresponding to the 2-node horizontal bending - 2-node twisting mode. Green point markers and blue star markers indicate port and starboard excitation, respectively.

deflection shape combining both modes (Figure 5.14).

The fact that all operating deflection shapes seem to excite horizontal displacement, vertical displacement and rotation might seem confusing at first but there are a number of reasons why this is the case. Firstly, as the accelerometer measuring vertical acceleration was located on the Main deck, it would actually detect torsional modes and measure values of similar magnitude to the horizontal acceleration for antisymmetric vibration. In the sole case of pure symmetric vibration, i.e. the 2-node vertical bending (Figure 5.9), the horizontal acceleration was measured as 20 times smaller than the vertical acceleration and rotational acceleration was an order of magnitude smaller than in any other case. The 2-node vertical bending peak is not visible in the horizontal or rotational acceleration when the

Table 5.4: Unballasted vessel natural frequencies, as predicted by ANSYS in vacuo and as measured experimentally in air.

Mode	Predicted Frequency (Hz)	Measured Frequency (Hz)	Difference %
1-node HB, 1-node T	63.9	65.7	-2.44
2-node VB	79.0	75.1	5.33
2-node HB, 2-node T	100.2	97.5	2.77
3-node HB, 3-node T	193.1	191.1	1.10
3-node VB	196.1	191.1	2.67
2-node HB, 2-node T	206.8	200.2*	
4-node HB, 4-node T	303.8	299.4	1.44

vessel was excited horizontally (Figure F.1) and is only slightly visible in the vertical acceleration, probably excited due to its proximity to the 1-node twisting natural frequency.

The maximum difference between predictions and measurements was just over 5% (Table 5.4). As noted earlier, the 3-node horizontal bending - 3-node twisting mode and 3-node vertical bending modes appear to coexist in the operating deflection shape in Figure 5.14. Looking at the frequency response functions under horizontal and vertical excitation (Figures F.1, F.1, respectively), it may be observed that, apart from the peak at 191 Hz there is a second one at 200 Hz, which is much more prominent under vertical excitation. The latter observation combined with the expectations from the simulations, indicate that the peak at 200 Hz probably corresponds to the 3-node vertical bending mode or to the (otherwise absent in the experiments) second 2-node horizontal bending - 2-node twisting mode. However, the operating deflection shape for that frequency provided inconclusive information.

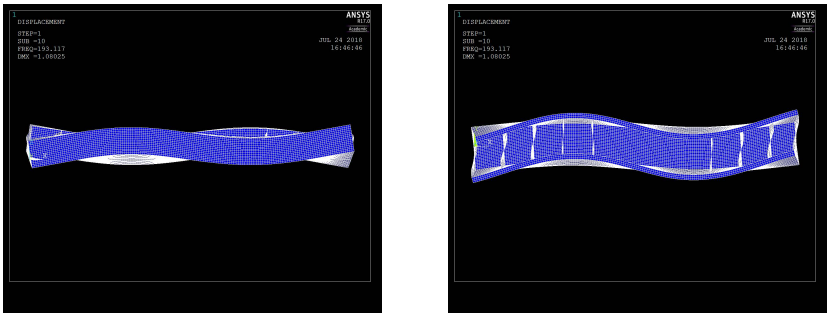

(a) Side (b) Top

Figure 5.12: 3-node horizontal bending - 3 node twisting mode, as predicted by shell modelling (natural frequency of 193.1 Hz)

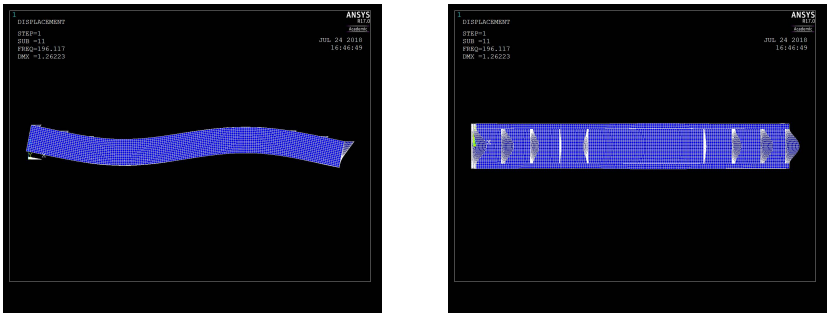

(a) Side (b) Top

Figure 5.13: 3-node vertical bending mode, as predicted by shell modelling (natural frequency of 196.1 Hz)

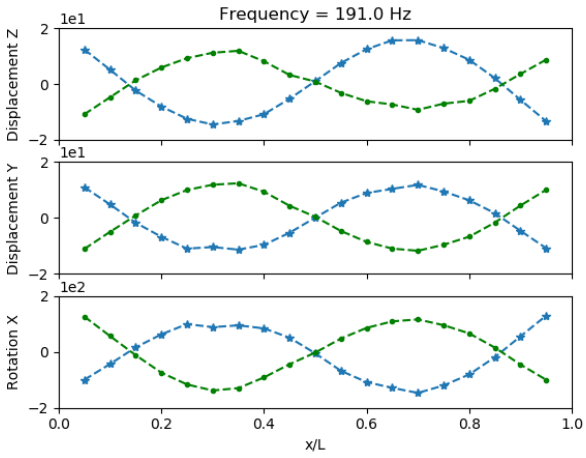

Figure 5.14: The measured ODS corresponding to the 3-node vertical bending and 3-node horizontal bending - 3-node twisting modes. Green point markers and blue star markers indicate port and starboard excitation, respectively.

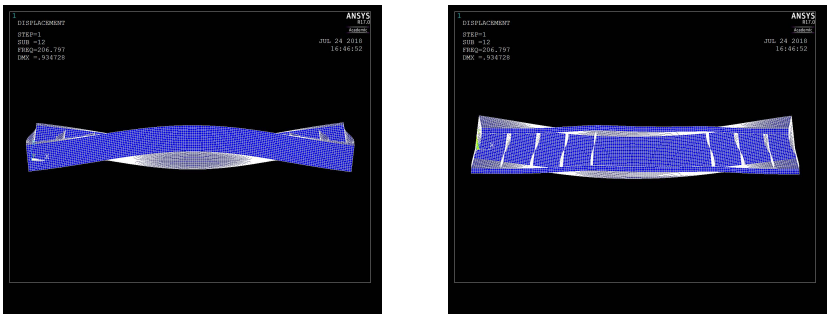

(a) Side (b) Top

Figure 5.15: Second 2-node horizontal bending - 2 node twisting mode, as predicted by shell modelling (natural frequency of 206.8 Hz)

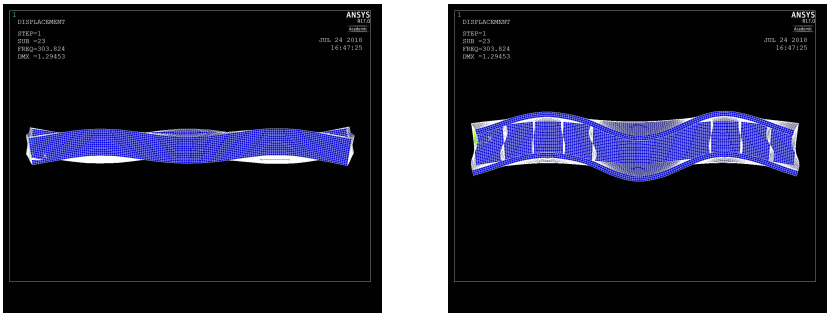

(a) Side (b) Top

Figure 5.16: 4-node horizontal bending - 4 node twisting mode, as predicted by shell modelling (natural frequency of 303.8 Hz)

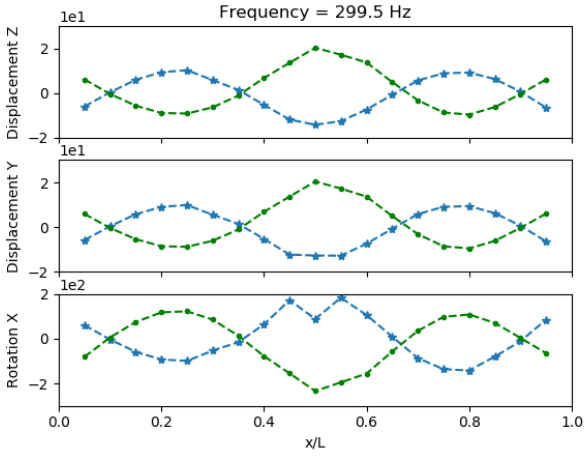

Figure 5.17: The measured ODS corresponding to the 4-node horizontal bending - 4-node twisting mode. Green point markers and blue star markers indicate port and starboard excitation, respectively.

5.7 Measured structural damping

In order to calculate the modal damping, MATLAB function *modalfit* was used. This function takes a frequency response function (or series of frequency response functions) as an input and uses curve-fitting techniques to translate that to a series of natural frequencies and the corresponding damping ratios and mode shapes. Use of this technique ensured that the whole frequency response function, rather than isolated peaks, was taken into account when calculating damping.

The full post-processing procedure comprised the following steps:

1. The excitation and response time signals would be measured using SingalCalc and three repetitions would be performed at each test point.

2. SignalCalc would calculate and export an average frequency response function for the acceleration, generated by averaging the frequency response functions for each repetition.

3. The average frequency response function for each of the test points would be imported in MATLAB, where *modalfit* would be used to fit a curve through it and thus estimate the modal parameters.

4. For each peak in the frequency response function, the natural frequency and damping ratio would be exported by *modalfit*.

Damping was calculated for each specimen type, for the first one, two or three modes. The accuracy of the method decreased significantly for higher-order modes, as well as natural frequencies higher than 1000 Hz. Consequently, these results had to be ignored - their importance not being particularly significant, as these measurements would be at quite different frequencies from what was measured on the vessel.

Table 5.5: Damping ratios for the unballasted model.

Mode	Frequency (Hz)		Damping ratio	
	Mean	SD	Mean	SD
1-node HB, 1-node T	65.7	0.1	0.0067	0.0003
2-node VB	75.1	0.3	0.0071	0.0011
2-node HB, 2-node T	97.5	0.3	0.0078	0.0010
3-node HB, 3-node T	191.1	1.5	0.0091	0.0004
2-node HB, 2-node T	200.2	0.5	0.0089	0.0011
4-node HB, 4-node T	299.4	0.4	0.0086	0.0012

A summary of the calculated damping ratios can be found in Figure 5.18 and Table 5.5. A number of observations can be made. Firstly, the spread

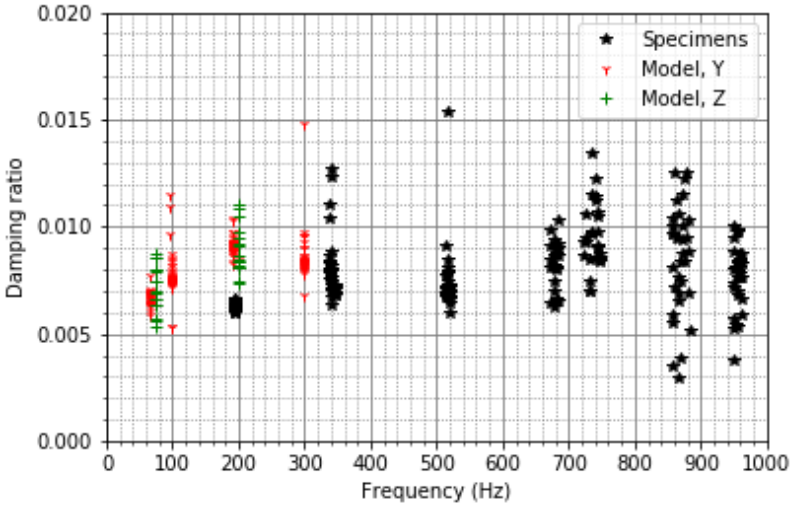

Figure 5.18: The damping ratios for various natural frequencies. Black star-shaped, red Y-shaped and green cross-shaped markers correspond to specimen testing, model excited from the side (antisymmetric modes) and model excited from top (symmetric modes), respectively.

of measurements per frequency seems to be smaller for longer specimens and lower frequencies. Secondly, the damping ratio for the 2-node vertical bending and 1 node horizontal bending-1 node twisting modes of the vessel are quite similar to the damping ratio corresponding to the 2-node vertical bending mode for the longer specimens (520 mm).

It can be concluded that measurements of structural damping from (box-shaped) specimen testing can provide a good estimation of the relevant values on a more complicated cellular structure, when both are produced using additive manufacturing and the same material. These values can serve as indicators during the design stage but experimental measurement of damping in the final structure is necessary.

5.8 Summary of findings

In this chapter, specimen-scale experiments were designed and carried out, with cellular specimens (box-shaped cross-section) subjected to both static and dynamic excitation. The specimens were designed with the same thickness as the walls of the vessel. It was demonstrated that the flexural modulus can be quite different if calculated from static responses and if calculated from dynamic responses. Furthermore, the dynamic flexural modulus was successfully used to predict the natural frequencies of the vessel, to the

extents that hammer testing allowed to observe. Nevertheless, the modes already identified in this chapter would be more than sufficient to describe the dynamic responses of ship models. Furthermore, the accuracy of the natural frequency predictions, compared to those based on 3-point bending tests of coupons, improved exceptionally. Finally, the damping ratios for the various operating deflection shapes were found to be comparable to the ones measured for the longer specimens, indicating that an estimation of these based on specimen testing is possible.

Chapter 6

Model hydroelastic testing

6.1 Overview

In the two previous chapters, the design and manufacturing procedures for the model were presented and complemented by a specimen-scale method to accurately predict the model's dynamic properties during the design stage. In this chapter, the model is instrumented with all the necessary sensors for the experiments to follow. It is then subjected to a series of tests and its responses are measured and analysed. These tests include measurement of the static responses to calibrate the sensors, the dry & wet free vibration responses (while ballasted), to identify the vibratory properties and, finally, the hydroelastic responses in waves. Particular focus will be given on the latter, while the results from free vibration will be utilised, among others, to explain the frequency content of the hydroelastic response.

6.2 Instrumentation

The model was instrumented with 16 strain gauges and an accelerometer. Measurements in both static and towing tank tests were obtained using a National Instruments cDAQ-9135 Data Logger. Two National Instruments NI-9236 strain gauge modules were used for the strains and a NI-9234 sound and vibration input module for the accelerations. During towing tank tests, measurements for heave and pitch were transferred from the locally used amplifying unit to a NI-9205 Voltage module. All the above measurements were obtained using LabVIEW software. The wave probe measurements during the tank tests were obtained through the Lasso software, developed by the Wolfson Unit.

The strain gauges used were Micro-Measurements C2A-06-250LW-350 linear quarter-bridge strain gauges with a resistance of 350 Ω and a gauge factor of 2.150$\pm$0.5%. Half of the gauges were placed on the main deck, port and starboard. Seven gauges were placed on the inner bottom and the

last one was placed on the inner side of the vessel. All strain gauges were placed parallel to the longitudinal axis of the vessel. Detailed positioning of the gauges is presented in Table 6.1. The accelerometer used was a PCB-352C33 and was installed on station 0.5, on the centreline.

Table 6.1: Positioning of strain gauges. X refers to stations, Y to port, starboard or centreline and Z to main deck, inner bottom or inner side

#	X	Y	Z
0	5.0	P	MD
1	7.5	P	MD
2	10.0	P	MD
3	12.5	P	MD
4	15.0	P	MD
5	5.0	S	MD
6	10.0	S	MD
7	12.5	S	MD
8	5.0	C	IB
9	7.5	C	IB
10	10.0	C	IB
11	12.5	C	IB
12	15.0	C	IB
13	10.0	P	IS
14	10.0	P	IS
15	10.0	S	IS

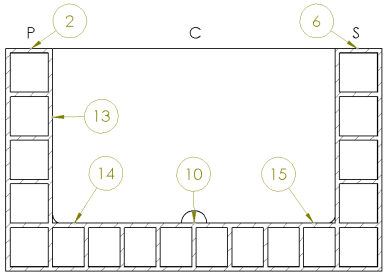

Figure 6.1: Locations of strain gauges amidships (i.e. station 10.0). Main deck and inner bottom locations same for other stations (See also Table 6.1).

6.3 Static responses

The model was subjected to static tests with no ballast for strain gauge calibration. Two angled bars were used to emulate pinned support on either end. The test started with the model only loaded by its own weight. All masses were then placed on station 8, on the tow post position. The incremental loading started with 0.5 kg, moving to 1.0 kg, 2.0 kg, 3.0 kg, 5.0 kg, 10.0 kg, 15.0 kg and 20.0 kg. The results (Figure 6.2) reveal an almost linear behaviour near the origin, uniform for all sensors. The sudden change in slope after 15 kg is not of interest to us as the loading from waves causes bending moments much lower than that point load. The inner side strain gauge measured negative strains as it is located above the neutral axis.

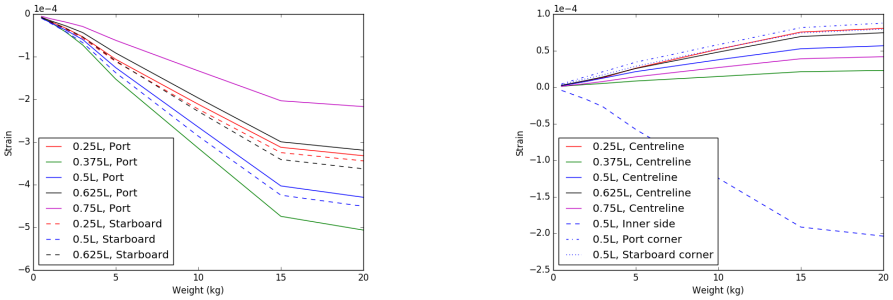

(a) Main deck

(b) Inner bottom & Inner side

Figure 6.2: Results from the static tests reveal an almost linear behaviour.

6.4 Measurement of modal properties

The model was subjected to modal testing at a free support condition. The model was ballasted using the same mass distribution as for the towing tank. Additional ballast masses were used to substitute the mass of the tow post. The model was tethered using bungee cords at stations 6 and 14, as due to spacial constraints in the experimental setup it was not possible to tether it exactly at the 2-node vertical bending mode nodes (namely stations 5 and 15). The roving hammer setup used a PCB-086C03 instrumented hammer (sensitivity: (±15%) 11.2 mV/N) with a hard plastic tip (white) for the excitation measurement and three PCB-352C22 accelerometers (sensitivity: (±15%) 1.019 mV/(m/s^2), 0.998 mV/(m/s^2) and 1.003 mV/(m/s^2), respectively) for the response measurement.

The accelerometers were located at station 19 of the vessel on the starboard side. Two of them were installed on the inner side to measure along the Y-axis. This setup was selected so that further post-processing of the measurements would allow the calculation of translational and rotational acceleration at the midpoint [12]. The vertical locations of these accelerometers (z=0.031 and 0.059 from the keel, respectively) were selected so that the midpoint coincides with the vertical location of the centroid of the cross-section. The third accelerometer was placed on the main deck to measure along the Z-axis.

All measurements were obtained using a DataPhysics Quattro acquisition system and SignalCalc software and the latter was also used for the calculation of the relevant frequency response functions. For each measurement point, the test was repeated thrice, the frequency response function was calculated for each repetition and an average was produced. The measured frequency range was between 0 and 400 Hz (at a 0.5 Hz step).

The vessel testing was split into two phases. In the first one, the vessel was excited horizontally. The excitation points were located at each station

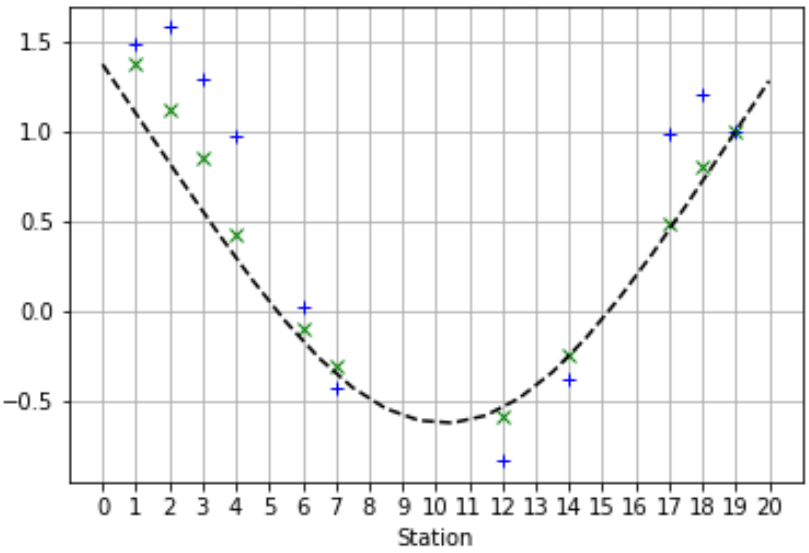

Figure 6.3: 2-node bending operating deflection shape, measured by exciting the main deck on the port (blue) and starboard (green) side of the vessel. The prediction from linear beam theory is depicted with a dashed line.

(so every 5% of the vessel length), starting at station 1 and ending at station 19. For all stations, the excitation point was located at the side wall of the vessel and exactly below the main deck. Measurements were obtained on both the port and the starboard side.

In the second phase, the vessel was excited vertically. The excitation points were located at the midpoint of the main deck, both for port and starboard side. In this case, not all stations could be excited due to the presence of strain gauges in some of them. Namely, stations 1, 2, 3, 6, 8, 11, 13, 14, 16, 17 and 19 were excited on both sides of the vessel.

The test procedure was repeated with the vessel placed in the towing tank rather than supported by bungee cords, to measure the modal responses in water. Structural damping was calculated by curve-fitting the frequency response function, as described in the previous chapter.

6.5 Natural frequencies and damping of ballasted model

The measured dry & wet natural frequencies of the ballasted vessel and the corresponding wet damping ratios are summarised in Table 6.2. Statistical values for both were calculated from the different excitation points. As far

as the damping ratios are concerned, only results with sufficiently small standard deviation (less than 50%) from the average are presented.

Table 6.2: Measured natural frequencies and damping ratio for the ballasted vessel. Damping ratio values correspond to the vessel in water. Higher-order natural frequencies in vacuo are missing as they could not be accurately identified (see text).

Mode	Dry f_n (Hz)		Wet f_n (Hz)		Damping ratio	
	Mean	SD	Mean	SD	Mean	SD
2-node VB	51.8	0.7	30.0	0.3	0.0146	0.0025
1-node HB, 1-node T	66.8	1.3	46.4	0.3	0.0113	0.0023
2-node HB, 2-node T	-	-	54.8	0.7	0.0240	0.0092
3-node VB	-	-	78.2	0.8	-	-

Ballasting the vessel increased its mass and reduced the natural frequencies, particularly those corresponding to symmetric responses. It also appeared to increase the modal damping significantly, resulting in quite wide peaks in the frequency response function. The latter rendered identification of the higher-order natural frequencies quite challenging and also led to poor performance of the curve-fitting techniques in general. This can be observed, for example, in the fact that only the first symmetric and first antisymmetric mode in vacuo could be clearly identified.

Some increase in the damping due to ballast masses could be caused by dry friction between the masses and the structure, similar to cargo damping described by Betts et al. [94]. The absence of this phenomenon when testing with backbone models can be explained by the fact that, in those cases, the ballast masses are not in direct contact with the load-bearing, vibrating structure. Still, the damping appeared to have almost doubled when compared to the case of the unballasted model, which was an unreasonably large increase.

The frequency response functions of the model in water were found to have more pronounced peaks and higher-order modes could be identified. The wet natural frequencies were further reduced due to the effects of added mass. Uncertainty over the damping ratios increased with mode order, with the standard deviation corresponding to the second antisymmetric mode being almost 40% of the average. Curve-fitting techniques around the 3-node vertical bending natural frequency and beyond performed too poorly to draw any conclusions.

As the presence of fluid around the vessel could not possibly have reduced structural damping, it was concluded that part of the increase compared to the unballasted vessel reported earlier in this section was probably a result of friction between the bungee cords and the model (for tests in vacuo), due to them being tighter around a now heavier model. Measured

damping ratios for the dry hull are thus omitted here as interference from the support is almost certain. The magnitude of damping ratios in calm water was comparable to previous measurements from container ship backbone models (e.g [21, 59]).

6.6 Experiments in head waves

The model was tested in head waves in the Solent University towing tank, for which the particulars may be found in Table 6.3.The tow post was placed at station 12, i.e. 10% fore of the midship section. A piece of plywood 250 mm long and 150 mm wide, connected to the model using captive nuts and threaded bars served as the base for the tow post (Figure 6.4a). It was found that the resulting tow post position was not entirely level, resulting in a small heel angle of the model while testing, as seen in Figure 6.5a.

(a) tow post attachment

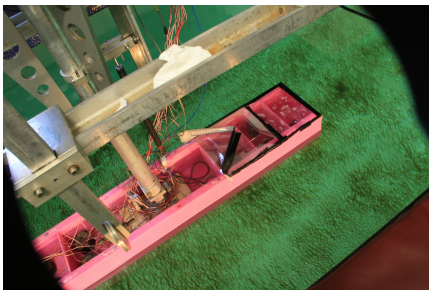

(b) Forward deck & wave breaker

Figure 6.4: A tow post, forward deck and wavebreaker were attached to the vessel.

The positions of the ballast masses may be found in Table 6.4. The mass at station 12 is the mass of the tow post arm. The mass of the model alone, including the tow post, was found to be 8 kg. The above resulted in a displacement of 15.60 kg and zero trim.

Table 6.3: Solent University towing tank size and capabilities

Length	60.0	m
Width	3.7	m
Depth	1.8	m
Maximum velocity	4.0	m/s
Maximum model length	2.0	m

The model was tested without forward speed at a range of frequencies and with a constant wave height of 0.05 m which corresponds to H_{wave}/L_{BP} of 1/30. The wave frequencies were selected based on the λ/L used in [5, 23]

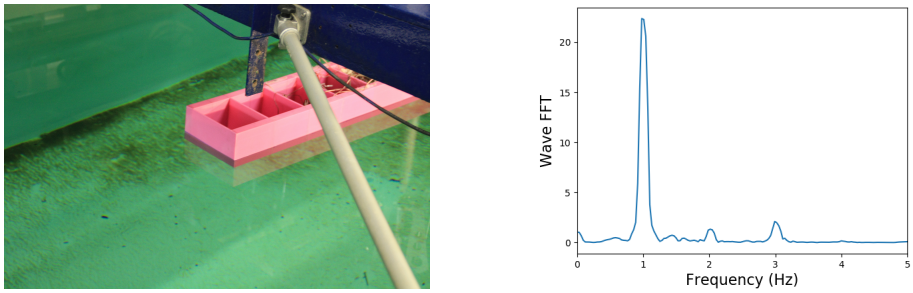

(a) Model heel (b) Wave FFT

Figure 6.5: Uncertainties in the experimental process included a small heel angle of the model (small enough to not be easily discernible in the picture) as well as frequencies other than the nominal contaminating the regular waves produced.

Table 6.4: Positions of ballast masses along the centreline.

station	Mass (kg)
1.0	0.50
2.5	0.50
4.5	0.50
6.5	1.00
8.0	2.00
15.5	1.00
17.5	1.00

for the relevant wave height ratio. Some of the frequencies were then also tested with a forward speed of 0.49 m/s. The Froude number used in [5, 23], corresponding to a forward speed of 1.06 m/s was found to result in excessive amounts of green water, even in still water, due to the blunt shape of the bow. The full test matrix may be found in Table 6.5. An irregular sea state with T_m=0.99 sec and H_s=0.039 m was also tested at no forward speed. The tests were repeated three times for each case.

A deck structure and wave breaker were fitted to avoid water ingress (Figure 6.4b). The model was weighed before and after the testing each day to ensure no water ingress was present. After three days of testing, the mass had increased from 14.8 kg to 14.85 kg using a scale with an accuracy of $\pm$0.025 kg.

The measurements were processed using a windowed Fast Fourier Transform (FFT). The flat top window was used as it was found to produce the most accurate results as far as signal amplitude is concerned, although it creates more spectral leakage than other windows. The response amplitude

Table 6.5: Wave length ratios and frequencies for the tests in regular waves. A wave height of 0.05 m was used in all cases.

λ/L	ω (rad/s)	f (Hz)	v=0 m/s	v=0.49 m/s
0.6	8.22	1.31	✓	✗
0.8	7.12	1.13	✓	✓
0.9	6.71	1.07	✓	✗
1.0	6.37	1.01	✓	✓
1.1	6.07	0.97	✓	✗
1.2	5.81	0.93	✓	✓
1.3	5.59	0.89	✓	✗
2.0	4.50	0.72	✓	✗

operators (RAOs) were calculated for each run and all runs were plotted as point cloud.

The strains were converted to bending moments using the bending moment/strain coefficients obtained from the static tests. The bending moments from the strain measurements and the 2D hydroelasticity predictions were then non-dimensionalised using the following equation:

$$C_M = \frac{M}{\rho g L^2 B A_{wave}} \tag{6.1}$$

The responses of the vessel were compared to results from a linear 2D hydroelastic code, based on strip theory and Timoshenko beam theory [11]. The ship was modelled as 20 strips, where the actual mass distribution was used and the flexural modulus was selected to produce, in conjunction with the known second moment of area, the correct 2-node bending natural frequency. Apart from the dry natural frequencies and mode shapes, the code was used to produce the heave, pitch and bending moment RAOs of the vessel.

The FFT of a typical regular wave reveals two smaller peaks following the primary peak of the desired frequency (Figure 6.5b). This could be attributed to interference by the beaches on the side of the towing tank, which were interacting with the waves although raised.

The blunt bow of the vessel resulted in significant green water at forward speed. The same phenomenon was observed when a wave length of 0.6L was tested, as the vessel would crush into the waves rather than riding on them. As the wave probe was located at the same x as the bow of the vessel, the wave measurements in these cases were significantly affected. In the case of testing with no forward speed, however, the responses would be, to some extent, affected by tank wall effect.

6.7 RAOs in head waves

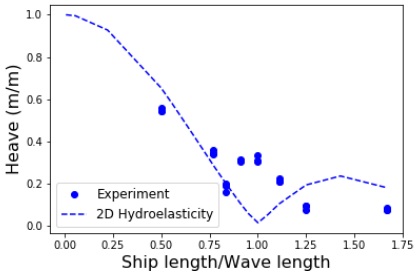

(a) Heave

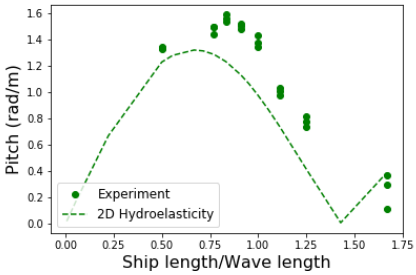

(b) Pitch

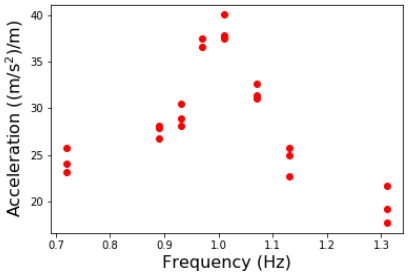

(c) Acceleration

Figure 6.6: Heave, pitch and acceleration RAOs at no forward speed, comparison between experiments and linear strip theory (where available).

Heave and pitch responses showed relatively good agreement with strip theory results, although the code used failed to identify a peak in the heave responses at the area of wave-ship matching (Figure 6.6a). Discrepancies between measured & predicted rigid body motion responses were attributed to the use of Lewis sections for a vessel with rectangular cross sections and vertical bow and stern walls. Although no data for the acceleration were provided by the code, the shape of the relevant RAO curve was reasonable, peaking around the ship-wave matching area (Figure 6.6c).

Bending moment measurements were found agree better with 2D hydroelasticity for the aft half of the vessel (stations 5.0, 7.5 and 10.0). Measurements were found to be less consistent between runs for shorter wave lengths and differences between measurements and predictions also increased for these cases. Green water was observed on the deck of the vessel for these higher frequencies, particularly for λ/L=0.6. The bluff bow of the vessel would crash into these shorter waves and part of the wave would run over the fore deck. Overall, looking at the non-dimensionalised vertical bending moment coefficients, it was observed that the first harmonic component had similar values as the ones measured by Chen [5] for the S-175

container ship.

Measurements in regular head waves with forward speed did not provide any further information regarding the model's responses, with the main difference being the change of wave encounter frequency. Similarly, no further insight was gained from the tests in irregular waves.

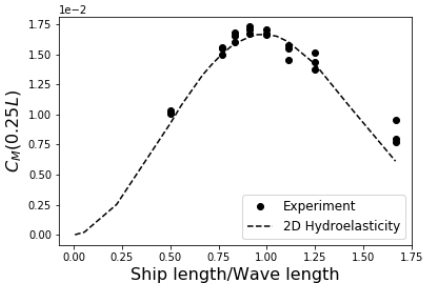

(a) 0.25L

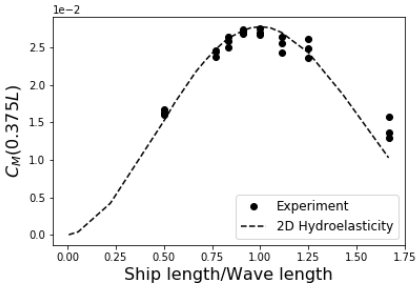

(b) 0.375L

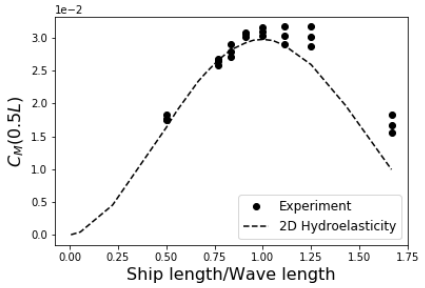

(c) 0.5L

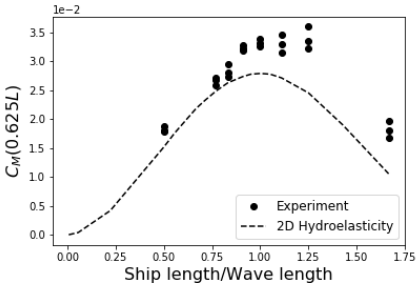

(d) 0.625L

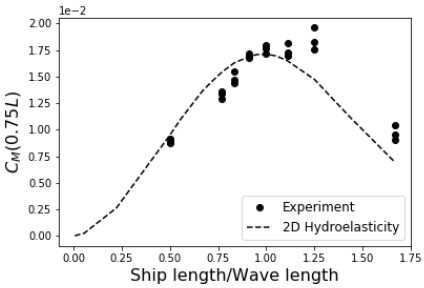

(e) 0.75L

Figure 6.7: Bending moment RAOs at zero forward speed agree well with linear strip theory, especially towards the aft part of the vessel.

6.8 Strain distribution throughout the vessel

Static tests indicated an almost linear material behaviour. A significant change in the load-strain slope around 20 kg in all sections can be attributed to material non-linearity, which was expected as stress-strain curves for ABS are of sigmoidal shape. The responses of the vessel in waves should not be affected as they were found to be well below that region. Both static tests and towing tank tests revealed limited asymmetry between the responses at port and starboard side of the vessel. The difference was, in most cases, of the order of 3% and could be a result of the manufacturing process and material uncertainty (also observed in the mechanical tests). Some asymmetry was also observed in the hammer tests (Figure 6.3) but the differences were within the accuracy of the instrumented hammer ($\pm$ 15%)

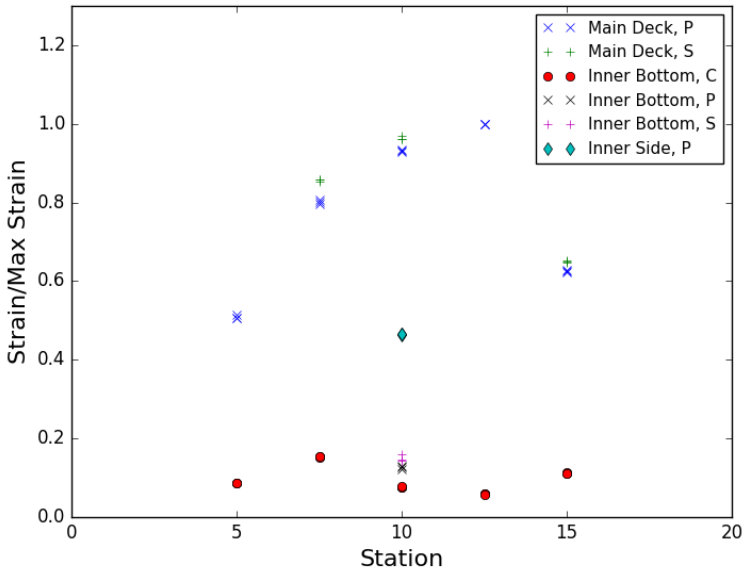

Figure 6.8: Strain distribution reveals limited asymmetry in the responses as well as locally increased stiffness at the inner bottom, around the tow post attachment.

Interestingly, the strain distribution revealed significantly reduced values for inner bottom centreline gauges at stations 10 and 12. Figure 6.8 includes measurements for no forward speed and a wave length equal to ship length, although similar measurements were observed for other frequencies. This phenomenon was also observed in static tests and was attributed to locally increased stiffness because of the presence of the plywood piece and tow post attached to it (Figure 6.4a). This would mean that the responses

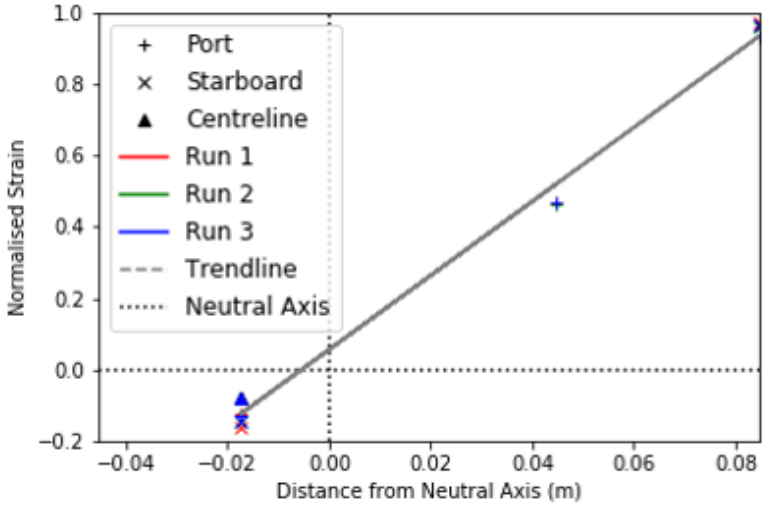

Figure 6.9: Strain distribution amidships indicated linear distribution of stress as a function of distance from the neutral axis, agreeing with beam theory.

measured in those areas no longer correspond to the global responses of a free-free beam idealisation. This effect was not evident in measurements from the main deck, although comparison with linear strip theory results showed better agreement for the aft stations, possibly resulting from the same added stiffness (Figure 6.7).

While the stiffness originating from the plywood piece was undesirable, it is probably unavoidable unless a completely free-running model were to be used in an ocean basin. Nevertheless, it demonstrated how the local arrangement of the structure can cause the responses to deviate from beam theory although they result from global loading. Consequently, these measurements could not be produced by extrapolation from a segmented model, which would be a further source of uncertainty if they were related to the ship's structural arrangement.

The strains within the cross section of the model (in this case, amidships) are depicted in Figure 6.9 as a function of the distance from the cross-section's neutral axis. These measurements are based on the same condition as Figure 6.8. It was observed that the strain distribution has a linear relationship with the aforementioned distance, with the strain being approximately zero at the neutral axis. This reinforced the argument that the model's behaviour can be approximated well using Timoshenko beam theory.

6.9 Non-linear responses in head waves

Significant excitation of higher order harmonic responses was observed. An example of the relevant isolated signals (obtained by use of a band-pass 1st order Butterworth filter) is depicted in Figure 6.10. These harmonics were partly the result of higher frequency components in the wave itself (see also Figure 6.5b), which also explains the fact that the 3rd harmonic response had a higher amplitude than the 2nd harmonic response (same pattern observed in the waves). It can be easily observed, however, that harmonic components of much higher order (e.g. 5th), were of similar magnitude to the second harmonic component. The same applied for much higher-order components, with the 15th harmonic being of similar magnitude to the 6th. Components of the response beyond 6th order were omitted from the figure to avoid making it illegible by overcrowding it.

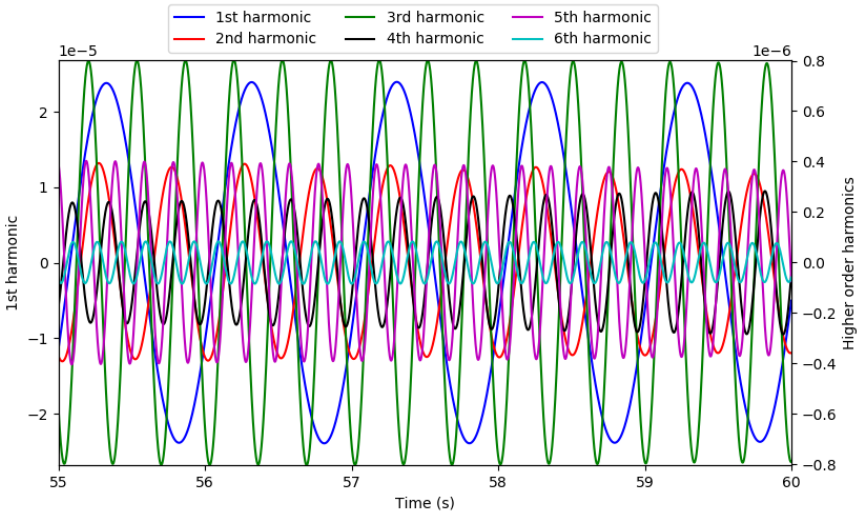

Figure 6.10: Isolated time signal of the components of the response, including 1st order and higher order harmonics. The nominal wave frequency, in this case, was 1.01 Hz, corresponding to wave-ship matching.

The 2-node vertical bending and 3-node vertical bending components were also present in the FFT of the response. It was demonstrated, however, that, even in still water and with a stationary carriage (a testing condition used as a baseline), the 3-node bending mode was excited to a similar extent and the 2-node bending mode was also excited significantly. These responses were, consequently, partly excited by some type of interference, although its source was not identified with certainty. It was confirmed, however, that while testing the model in a different facility (both in static condition and in a few wave cases at zero forward speed) these components of the response disappeared. In the cases of slamming, approximately half

of the magnitude of the 2-node bending response seemed to result from slamming but it was impossible to isolate one component from the other. Consequently, no definite conclusions regarding the magnitude of whipping responses could be drawn.

The non-dimensionalised 2nd and 3rd order harmonic components were found to be of similar magnitude to what has been observed in the literature (e.g. by [5]). The measured amplitudes for different wave frequencies are summarised in Figure 6.11. The results seem less organised than what was previously witnessed in most investigations and feature similarities and differences regarding the patterns. Firstly, the responses were found to have a local maximum around the wave-ship matching area. This was more pronounced for the 3rd harmonic and particularly at the fore part of the vessel. The most significant inconsistencies with previous experience were the large magnitude of the 2nd harmonic component for a wave frequency corresponding to L/λ=0.5 and, similarly, for the 3rd harmonic component and a wave frequency corresponding to L/λ=0.77. Although there is currently no certain explanation for these quite pronounced peaks, it should be emphasised that uncertainties were increased not only because of the 2nd and 3rd harmonic components being present in the wave (as mentioned earlier) but also because the vessel was stationary, resulting in tank wall effect.

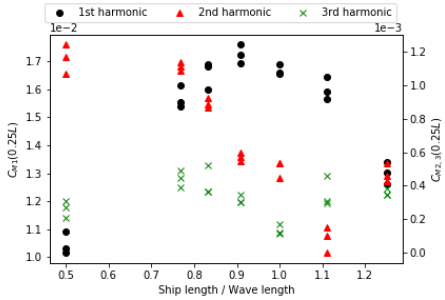

(a) 0.25L

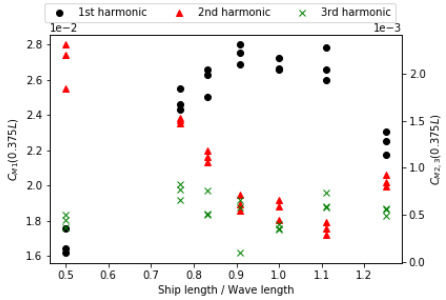

(b) 0.375L

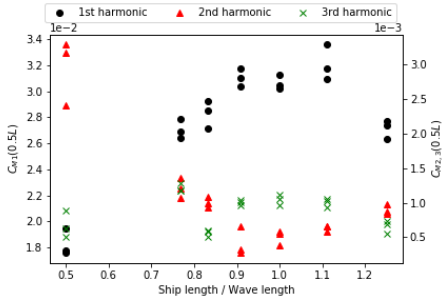

(c) 0.5L

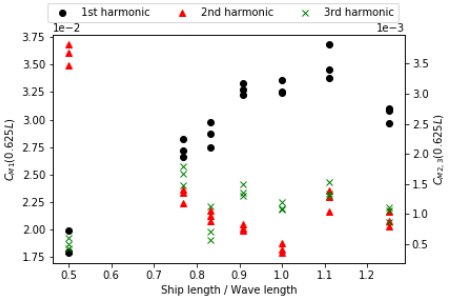

(d) 0.625L

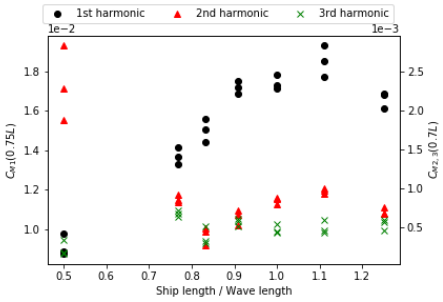

(e) 0.75L

Figure 6.11: Non-dimensional bending moments at zero forward speed, corresponding to the 1st, 2nd and 3rd harmonic components.

6.10 Experiments in beam and oblique waves

Although wet antisymmetric responses were not the focus of this investigation, a small number of experiments in beam and oblique seas were performed to determine whether these responses would be measurable on a 3D printed elastic model. As has been discussed in previous chapters, antisymmetric responses are one of the most likely areas to apply this concept. A continuous model with an internal structure resembling a ship can depict the correct distribution of torsional stiffness as well as location of shear centre. These two combined ensure not only appropriate coupling of horizontal bending and torsion but also accurately scaled mode shapes (and as has been demonstrated in the previous chapter, accurately scaled natural frequencies as well).

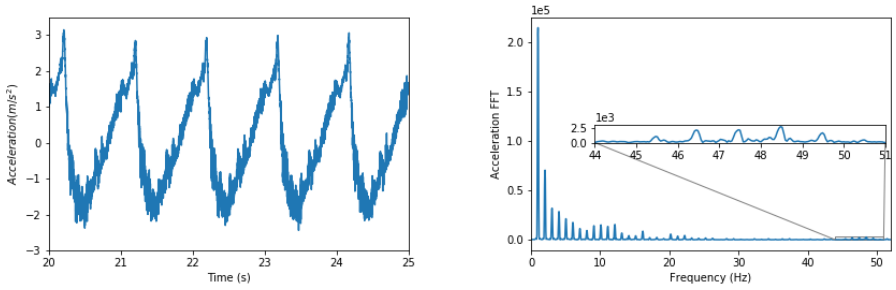

(a) Time signal (b) FFT

Figure 6.12: Extract of the acceleration time signal and the corresponding FFT, for tests of the model at a wave angle of 112°.

A number of limitations in the set-up of the experiments affected the measurements obtained. Firstly, due to the model being tested in a towing tank rather than an ocean basin, the experiments could only be performed at zero forward speed. Secondly, restrictions in the angle of the tow post did not allow for the usual 30° and 60° oblique wave angle cases to be tested. Wave angles of 112° and 156° were tested instead (in addition to beam seas). The fact that the oblique waves were not approaching the vessel from the the stern was not a problem, in this case, as the geometry of the model's bow and stern were identical and there was no forward speed.

The last limitation was due to the fact that no shear strain gauges were installed on the model. Antisymmetric responses tend to be twist-dominated and direct strains (caused by horizontal bending and warping) are difficult to measure. In the absence of such sensors, an accelerometer was installed near the stern of the model (station 1), measuring in the transverse direction, so as to capture twisting and horizontal bending but not vertical bending. The accelerometer was installed on the inner side of

the hull, just below main deck level.

Due to time constraints only one wave frequency was tested and this was arbitrarily selected to correspond to ship-wave matching and a wave height of 0.05 m.

Table 6.6: Mean values and standard deviation of the root mean square values of measured acceleration for various wave headings.

Angle (°)	Acceleration RMS (m/s^2)	
	Mean	SD
90	9.027E-02	5.665E-04
112	1.341E-01	5.347E-03
156	7.589E-02	4.490E-03

A summary of the root mean square values of acceleration for each of the heading angles is presented in Table 6.6. The 1-node twisting - 1- node horizontal bending mode was excited in all cases. Figure 6.12 depicts the time signal and the FFT for one of the test repetitions of the 112° case. The frequency content of the response contains significant high frequency components, mostly resulting from higher-order harmonics of the wave frequency. Nevertheless, the excitation of the first antisymmetric mode is clearly visible in the FFT of the signal, even if the magnitude of the relevant peaks is much smaller than, for example, that corresponding to the first harmonic. It should be emphasised, at this point, that part of the lower-frequency components of the signal originates from roll motions that can increase the relevant magnitude remarkably.

6.11 Summary of findings

The container ship-inspired cellular barge was instrumented with a series of strain gauges and tested in a variety of environments. Static tests demonstrated that the structural responses within this investigation fall within the linear range of the material. The modal properties of the model were also measured, and comparison was made between the dry and wet natural frequencies and damping coefficients. The first harmonic component of the bending moments in waves was found to agree reasonably well with existing theory and literature. The strain distribution within the cross-section of the vessel indicated beam-like behaviour. Consequently, it was demonstrated that a 3D printed elastic ship model is able to appropriately depict the global responses of a ship. Furthermore, it was found to be capable of capturing local responses, such as in the case of the tow post attachment.

Several higher-order components of the wave frequency were observed in the vertical bending moment response. The 2-node bending and 3-node

bending modes were excited, among others, by interference in the measurements. The 2nd and 3rd order bending moment components were found to be of similar amplitude to what has been previously observed in the literature. Finallly, it was demonstrated that the antisymmetric modes of the model can be excited in oblique seas to a measurable magnitude.

Chapter 7

A design procedure for 3D printed elastic ship models

7.1 Overview

As was demonstrated in the previous chapters, elastic models of ships can be manufactured and used for hydroelastic testing. Their behaviour mostly follows the existing theory, with some 3-dimensional structural effects (e.g. effects on stiffness and damping of objects placed inside/attached to the hull) being introduced due to the nature of the model. One of the main challenges encountered was the accurate prediction, during the design stage, of the modal properties of the vessel. With this in mind, a design procedure, including specimen testing, is introduced and outlined in this chapter for use in future investigations. Each of the following sections describes a stage in this procedure and the order in which the steps are presented should be followed.

7.2 Stage 1: Selection of details to be included, scale and material

- Given a specific ship to be modelled, a range of scaling can be crudely defined based on the capabilities of the towing tank (model length and forward speed restrictions).

- This range is further limited by the maximum build volume of the printer, which can vary significantly depending on whether a desktop printer or an industrial printer is used - the latter often being larger.

- With current printer capabilities, it is almost certain that the minimum thickness the printer can achieve will be used. In most cases,

this will be approximately twice the extrusion diameter. This will determine the plate thickness.

- It is recommended that only main structural elements (e.g. decks, sides, longitudinal stiffeners, bottom etc.) with a thickness of the same order as the main plating are included. The remaining details should be omitted/absorbed in an equivalent plate thickness, as they would otherwise be too thin (when scaled down) to be printed. Depending on the extrusion diameter of the printer and the scaling used, it may be possible to slightly vary the thickness throughout the cross-section to depict the corresponding variation on the full-scale vessel.

- A list of potential materials should be compiled. At this stage, the only information necessary is an approximate flexural modulus and the behaviour of the material in water.

- At this point, both the geometric details that will be included and the wall thickness have been selected. An iterative process (using material properties from the list compiled above) should be used to finalise the model scale. The criterion should be appropriate scaling of the 2-node bending natural frequency. The material is also decided at the same time, as each of the options is a combination of material and scale.

7.3 Stage 2: Material testing and prediction of model properties

- Specimens should be 3D printed using the same printer, material and printing parameters as will be used for the model. It is advised that these specimens are of cellular cross-section (not necessarily square). This way the thickness of the specimens can be the same as the one to be used in the model walls, while having a sufficiently large cross section to allow modal testing.

- The length of the specimens should be as long as possible to ensure that the natural frequencies are of the same order as those of the model. Analytical calculations assuming beam theory can help in defining the necessary length. In turn, minimum length relates to the need for beam behaviour and can be defined by running FEA simulations with beam and shell elements (as described in Chapter 5) and ensuring the differences between the two are small. A rule of thumb that can be used alternatively is to use a length at least ten times the largest dimension of the cross-section, which should produce accurate results with Timoshenko beam elements.

- The specimens will most probably have to be manufactured in segments along the length and the same joining technique as the one intended for the model should be used, although the latter is not expected to affect the results significantly. Bulkheads in the specimens can be omitted as they do not improve the accuracy of results and they slightly complicate modelling of the specimens (see Chapter 5).

- The specimens should be subjected to symmetric and antisymmetric modal testing to define the values of E, G and ν. Although the procedure is quite similar to those described by the standard, there are some small changes that are discussed in detail in Chapter 5.

- The frequency response functions from the specimen tests can also be curve-fitted to calculate structural damping. Data from the 2-node vertical bending mode will be the most reliable and is expected to give a reasonably good estimation of the damping of the equivalent model mode.

- The FEA simulations for the model should then be repeated, using the acquired values for E, G and ν and shell elements, unless a reliable way of calculating the sectional properties (particularly related to torsion) is available, in which case beam elements can be used as well. The FEA simulation does not have to include damping as this will not affect the natural frequencies.

- At this stage, the extent to which the desired modal properties are expected to be achieved should be evaluated. If the results are unsatisfactory, an iterative process involving changes in the sizing of the model and/or the material used might be necessary to improve the design. Further specimen testing might be necessary if there are drastic changes in material and/or thickness.

7.4 Notes on quality control

It is important to ensure that all printed components are of high quality and the printer is suffering from no issues or poorly selected parameters. Unfortunately, 3D printing can perform in varied ways based on the combination of application, printer, material and parameters. There is no such thing as a universal set of printing parameters that performs well every time.

Furthermore, due to the cellular and layered nature of the process, non-destructive testing techniques are not much help in the determination of printing quality. The only tool available to the investigator is visual inspection. Both the identification (through visual means) of potential

issues in the printed components and the selection of the right measures to eliminate them rely on the 3D printing experience of the investigator. Hence, it is highly recommended that sufficient time is spent training and practising to improve in these areas prior to starting the design procedure described above.

Finally, it is imperative that extensive dimensional measurements are taken throughout the process. Measurements during specimen production stage ensure accurate calculation of the material properties and also indicate the thickness uncertainty to be expected during model production. Measurements during the model production stage facilitate the estimation of bending stiffness and mass/unit length of the model and can be used to predict the model's modal properties before it is joined. Further measurements after joining (e.g. length) provide further information on the experimental uncertainties.

Chapter 8

Conclusions and recommendations

8.1 Summary

A review of the literature relevant to hydroelastic experiments demonstrated the reluctance of the scientific community to produce elastic models. Segmented models were manufactured in the vast majority of cases, due to the simplicity of their design and the capability to be modified after manufacturing. 3D printing was proposed as a potential solution to the problem, offering a relatively cheap and uncomplicated way to produce elastic models with accurate internal structure.

The principles used in the design of hydroelastic models were analysed. The 3D printing process was presented, along with the available material range, its parametric sensitivity and its limitations. The design of three different vessels (namely a rectangular barge, a Leander-class frigate and an S-175 containership) as elastic models was investigated, clearly demonstrating the complexity of the process. It was found that the feasibility of the project depends on the existence of a ship structure-scale-material combination, which is not always ensured. The necessity of the produced structure to resemble that of the full-scale ship limits the range of options even further. The containership was identified as the most promising option. A material investigation was performed, subjecting 3D printed coupons, made of ABS and T-glase, to flexural tests and demonstrating that the flexural modulus of these materials was higher than would be desired.

The design process was reiterated to produce a uniform cross-section cellular barge inspired by the S-175 container ship. The barge was 3D printed using ABS in 11 sections longitudinally, which were then joined using ABS paste. Transverse bulkheads were added and the vessel was instrumented with 16 strain gauges in various locations of the hull and accelerometer. Static testing was performed for sensor calibration, followed by hammer testing to define the modal properties and, finally, towing tank tests (in regular and irregular waves, with and without forward speed).

The uncertainties related to the manufacturing process and the various test procedures were discussed.

The model was found to have a higher 2-node bending natural frequency than initially expected. The issue was investigated further by producing specimens of various lengths with a cellular (box-shaped) cross section and subjecting them to modal testing and 3-poind bending tests. It was demonstrated that the dynamic flexural modulus of 3D printed plastics can be quite different from its static counterpart and the former needs to be used to assess the dynamic responses of 3D printed structures Furthermore, that the results from such specimen-scale experiments can be used to very accurately predict the natural frequencies of a cellular 3D printed structure, such as one resembling a container ship. Finally, it was shown that specimen-scale tests can also provide a reasonably good estimation of the damping properties of such a structure.

The model was subjected to towing tank tests at zero forward speed in regular head waves. The measured rigid body motion & bending moment RAOs compared reasonably well with 2D hydroelasticity. The stiffness of the model was found to locally increase around the area where the tow post was attached. The strain distribution throughout the cross section was found to be linear, agreeing with beam theory. Higher-order harmonic responses were also measured and both the magnitude of the 1st harmonic of the bending moment and the relative amplitudes of the 2nd and 3rd harmonic were found to agree reasonably well with existing literature. It was also demonstrated that at least the first antisymmetric mode can be excited when testing in oblique seas.

8.2 Main conclusions

8.2.1 Design and production of an 3D printed elastic ship model

Design of a 3D printed elastic ship model was found to be quite challenging. This stemmed, to some extent, from the complex nature of scaling the hydrodynamic and structural aspects of the model concurrently, combined with practical limitations on size and wall thickness of the model. More importantly, it was found that inadequate information is available on the mechanical properties of 3D printed components, partly because manufacturers do not provide all the necessary data and partly because, even when they do, the properties often correspond to the material before printing - not accounting for the anisotropic effects of the manufacturing process.

In addition to the above, it was demonstrated that traditional material testing methods, such as 3-point bending tests of coupons, are inappropriate to determine the vibratory properties of 3D printed polymers. It was established that flexural modulus of such materials can be significantly

different in static and dynamic conditions, the latter being relevant to vibratory responses. An alternative methodology was developed, which combined modal testing of specimens with a cellular (box-shaped) cross section with FEA modelling to identify the flexural modulus, shear modulus and Poisson's ratio. Crucially, the specimens were designed with the same wall thickness as the model so as to replicate part of the structure. Beam modelling and shell modelling produced almost identical results in most cases, with limited discrepancies observed for short specimens.

It was shown that, using the material properties obtained from the aforementioned specimen tests, the natural frequencies of the model can be accurately predicted using FEA modelling with shell elements. Structural damping could also be estimated from the same tests. No significant effects on the dynamic behaviour of the model due to joining along the longitudinal axis were evident. The above procedures and observations were summarised in the form of a step-by-step method for the design and production of 3D printed elastic ship models.

8.2.2 Responses of a 3D printed elastic ship model

Towing tank tests in head seas were performed to establish the validity of the concept of a 3D printed elastic ship model. In terms of the global response of the vessel, the first three harmonics of measured vertical bending moment in head waves agreed with existing theory and previous examples in the literature. Furthermore, strain distribution within the cross section increased linearly with distance from the neutral axis. Both observations above indicate beam-like behaviour, as is expected for ships, thus verifying the concept. Additionally, locally increased stiffness due to the tow post attachment demonstrated the capability of the model to capture local responses, which are absent in segmented models, and highlighted the need for the method of attachment to be reconsidered.

Despite the complex geometry of the model, the natural frequencies of the vessel were accurately predicted for the first four antisymmetric modes. Therefore, the method developed can be used for the design of a model replicating higher-order antisymmetric modes and accurately scaling the corresponding natural frequencies of a ship, unlike segmented models. Finally, excitation of the first antisymmetric mode was observed in acceleration data while testing in beam and oblique seas, indicating that measurement of the relevant shear strain responses would be feasible with use of appropriate sensors.

8.3 Future work

- A ship-shaped model should be produced and tested. This would allow investigation of phenomena that rely on a ship's shape as, for example, flare slamming responses. Improvements on the current design procedure and/or 3D printer capabilities might be necessary to concurrently scale the external geometry of the ship and its natural frequencies.

- Use of 3D printing could allow investigators to embed sensors and improve, in that way, the way responses are measured. For instance, strain gauges or miniature pressure sensors could be embedded in the structure to measure structural loads and slamming pressures, respectively.

- Antisymmetric responses of elastic models are of particular interest, due to the more appropriate representation of the torsional stiffness and shear centre location these models provide. Such experiments would require the use of shear strain gauges to measure strains caused by torsion.

- Investigation of the effect on stiffness and damping of items placed inside/attached to the hull could not only improve experimental procedure but also provide further information on similar effects (e.g. due to cargo-induced damping or presence of engine room) on full-scale ships.

- An elastic model with both global and local similarity could be particularly useful for the investigation of loading conditions where local structural damage is common.

References

[1] S. Peng, P. Temarel, S. S. Bennett, W. Wu, Z. Liu, and Y. Wang, "Symmetric response of a hydroelastic scaled container ship in regular and irregular waves," in *Proceedings of the ASME 2014 33rd International Conference on Ocean, Offshore and Arctic Engineering OMAE2014*, (San Francisco, California, USA), pp. 1–10, ASME, jun 2014.

[2] J. Lavroff, M. R. Davis, D. S. Holloway, and G. A. Thomas, "The Whipping Vibratory Response of a Hydroelastic Segmented Catamaran Model," in *Ninth International Conference on Fast Sea Transportation*, (Shanhai, China), 2007.

[3] D. Dessi and E. Ciappi, "Slamming clustering on fast ships: From impact dynamics to global response analysis," *Ocean Engineering*, vol. 62, pp. 110–122, 2013.

[4] I. Watanabe, M. Ueno, and H. Sawada, "Effects of Bow Flare Shape to the Wave Loads of a container ship," *Journal of the Society of Naval Architects of Japan*, vol. 1989, no. 166, pp. 259–266, 1989.

[5] R.-Z. Chen, S.-X. Du, Y.-S. Wu, J.-R. Lin, J.-J. Hu, and Y.-L. Yue, "Experiment on extreme wave loads of a flexible ship model," in *Practical Design of Ships and Other Floating Structures. Proceedings of the Eighth International Symposium on Practical Design of Ships and Other Floating Structures*, vol. 2, pp. 871–878, 2001.

[6] D. E. Hudson, "Scale model principles," *Shock and Vibration Handbook*, 1967.

[7] A. Castoldi and M. Casirati, "Experimental techniques for the dynamic analysis of complex structures," in *The Anti-Seismic Design of Nuclear Installations*, pp. 326–337, 1975.

[8] H. G. Harris and G. Sabnis, *Structural modelling and experimental techniques*. CRC Press, second ed., 1999.

[9] S. K. Chakrabarti, *Offshore Structure Modeling.* World Scientific, 1994.

[10] A. Lloyd, *Seakeeping : Ship Behaviour in Rough Weather.* Gosport: A.R.J.M. Lloyd, 1998.

[11] R. E. D. Bishop and W. G. Price, *Hydroelasticity of ships.* Cambridge University Press, 1979.

[12] D. J. Ewins, "Modal Testing: Theory, Practice and Application," p. 562, 2000.

[13] E. Ciappi, D. Dessi, and R. Mariani, "Slamming and whipping response analysis of a fast monohull via segmented model tests," in *Proceedings of the 3rd International Conference on Hydroelasticity in Marine Technology*, pp. 143–155, 2003.

[14] S. S. Denchfield, C. Wood, D. A. Hudson, M. Tan, and P. Temarel, "Comparisons between CFD predictions and experiments for rogue wave-ship interactions," in *11th International Symposium on Practical Design of Ships and Other Floating Structures*, (Rio de Janeiro), sep 2010.

[15] E. Dudson, H. J. Rambech, and M. Wu, "Determination of Wave Bending Loads on a 40 Knot , Long Slender Open Topped Containership Through Model Tests and Hydrodynamic Calculations With Particular Reference To the Effects of Hull Flexibility on Fatigue Life," *FAST 2001 The 6th International Conference on Fast Sea Transportation*, no. September, 2001.

[16] T. Zhu, A. Kumano, T. Shigemi, and R. Matsumani, "A consideration of wave-induced loads for direct strength calculation under extreme waves," *NK Tech Bulletin*, pp. 69–80, 2002.

[17] K. Iijima, T. Shigemi, R. Miyake, and A. Kumano, "A practical method for torsional strength assessment of container ship structures," *Marine Structures*, vol. 17, no. 5, pp. 355–384, 2004.

[18] E. Korkut, M. Atlar, and A. İncecik, *An experimental study of global loads acting on an intact and damaged Ro–Ro ship model*, vol. 32. 2005.

[19] Y. Takaoka, A. Murakami, T. Yoshida, R. Miyake, N. Yamamoto, K. Terai, and T. Kensaku, "An Experimental Study on the whipping response of large container carriers," in *Proceedings of the 6th International Conference on Hydroelasticity in Marine Technology*, (Tokyo, Japan), pp. 145–152, 2012.

[20] M. Oka, S. Oka, and Y. Ogawa, "An experimental study on wave loads of a large container ship and its hydroelastic vibration," in *Proceedings of the 5th International Conference on Hydroelasticity in Marine Technology*, 2009.

[21] M. Wu, E. Lehn, and T. Moan, "Design of a segmented model for ship seakeeping tests with hydroelastic effects," in *Proceedings of the 6th International Conference on Hydroelasticity in Marine Technology*, (Tokyo, Japan), pp. 135–144, 2012.

[22] G. A. Thomas, M. R. Davis, D. S. Holloway, and T. Roberts, "The whipping vibration of large high speed catamarans," oct 2003.

[23] Y.-S. Wu, R.-Z. Chen, and J.-R. Lin, "Experimental technique of hydroelastic ship model," in *Proceedings of the Third International Conference on Hydroelasticity, Oxford, UK, September*, pp. 15–17, 2003.

[24] K. Iijima, Y. Suzaki, and M. Fujikubo, "Scaled model tests for the post-ultimate strength collapse behaviour of a ship's hull girder under whipping loads," *Ships and Offshore Structures*, vol. 10, no. 1, pp. 31–38, 2015.

[25] T. Kinoshita, J.-s. Shi, S. Nakasumi, H. Kameoka, K. Suzuki, T. Waseda, K. Tanizawa, and T. Yuhara, "Longitudinal loads on a container ship in extreme regular sea and freak wave," *Proceedings of the 4th International Conference on Hydroelasticity in Marine Technology*, vol. 1, pp. 103–110, 2006.

[26] R. Miyake, T. Matsumoto, T. Zhu, A. Usami, and H. Dobashi, "Experimental studies on the hydroelastic response using a flexible Mega-Container ship model," in *Proceedings of the 5th International Conference on Hydroelasticity in Marine Technology*, (Southampton, United Kingdom), pp. 161–171, 2009.

[27] Š. Malenica, B. Molin, F. Remy, and I. Senjanović, "Hydroelastic response of a barge to impulsive and non-impulsive wave loads," in *Proceedings of the 3rd International Conference on Hydroelasticity in Marine Technology*, sep 2003.

[28] K. Iijima, O. A. Hermundstad, S. Zhu, and T. Moan, "Symmetric and antisymmetric vibrations of a hydroelastically scaled model," in *Proceedings of the 5th International Conference on Hydroelasticity in Marine Technology*, vol. 1213796053, 2009.

[29] S. Zhu, M. Wu, and T. Moan, "Experimental investigation of hull girder vibrations of a flexible backbone model in bending and torsion," *Applied Ocean Research*, vol. 33, no. 4, pp. 252–274, 2011.

[30] A. Marón and G. K. Kapsenberg, "Design of a ship model for hydroelastic experiments in waves," *International Journal of Naval Architecture and Ocean Engineering*, vol. 6, pp. 1130–1147, jan 2014.

[31] F. Remy, B. Molin, and A. Ledoux, "Experimental and numerical study of the wave response of a flexible barge," 2006.

[32] S.-X. Du, D. A. Hudson, G. W. Price, P. Temarel, R.-Z. Chen, and Y.-S. Wu, "Wavelet Analysis of Loads on a Flexible Ship Model Traveling in Large-Amplitude Waves," *Journal of Ship Research*, vol. 52, no. 4, pp. 249–262, 2008.

[33] H. Houtani, Y. Komoriyama, S. Matsui, M. Oka, H. Sawada, Y. Tanaka, and K. Tanizawa, "Designing a hydro-structural model ship to experimentally measure its vertical-bending and torsional vibrations," in *8th International Conference on Hydroelasticity in Marine Technology*, (Seoul, Korea), 2018.

[34] G. Coppotelli, D. Dessi, R. Mariani, and M. Rimondi, "Output-Only Analysis for Modal Parameters Estimation of an Elastically Scaled Ship," *Journal of Ship Research*, vol. 52, no. 1, pp. 45–56, 2008.

[35] D. Dessi and R. Mariani, "Structure and load identification using wave excitation in seakeeping tests," *20th IWWWFB, Spitsbergen, Norway*, pp. 6–9, 2005.

[36] D. Dessi, A. Engle, X. Gu, T. Ha, and T. Hodgson, "Impulsive Pressure Loading and Response Assessment," in *Proceedings of the 17th Ship and Offshore Structures Congress*, vol. 2, pp. 367–432, 2009.

[37] J. Lavroff, M. R. Davis, D. S. Holloway, and G. A. Thomas, "The Vibratory Response of High-Speed Catamarans to Slamming Investigated by Hydroelastic Segmented Model Experiments," *International Journal of Maritime Engineering*, vol. 151, pp. 1–13, nov 2009.

[38] M. R. Davis, G. A. Thomas, D. S. Holloway, J. Lavroff, W. Amin, S. Matsubara, and T. Roberts, "Slamming and Whipping of Wave-Piercing Catamarans," in *Proceedings of the 5th International Conference on Hydroelasticity in Marine Technology*, (Southampton, United Kingdom), pp. 223–232, oct 2009.

[39] S. Matsubara, G. A. Thomas, M. R. Davis, D. S. Holloway, and T. Roberts, "Influence of Centrebow on Motions and Loads of High-Speed Catamarans," *FAST 2011 11th International Conference on Fast Sea Transportation*, no. September, pp. 661–668, 2011.

[40] G. A. Thomas, S. Winkler, M. R. Davis, D. S. Holloway, S. Matsubara, J. Lavroff, and B. J. French, "Slam events of high-speed catamarans in irregular waves," *Journal of Marine Science and Technology*, vol. 16, pp. 8–21, aug 2011.

[41] J. Lavroff, M. R. Davis, D. S. Holloway, and G. A. Thomas, "Determination of wave slamming loads on high-speed catamarans by hydroelastic segmented model experiments," feb 2011.

[42] G. A. Thomas, S. Matsubara, M. R. Davis, B. J. French, J. Lavroff, and W. Amin, "Lessons learnt through the design, construction and testing of a hydroelastic model for determining motions, loads and slamming behavior in severe sea states," in *Proceedings of the 6th International Conference on Hydroelasticity in Marine Technology*, (Tokyo, Japan), pp. 163–172, nov 2012.

[43] J. Lavroff, M. R. Davis, D. S. Holloway, and G. A. Thomas, "Wave slamming loads on wave-piercer catamarans operating at high-speed determined by hydro-elastic segmented model experiments," *Marine Structures*, vol. 33, pp. 120–142, 2013.

[44] B. J. French, G. A. Thomas, and M. R. Davis, "Slam characteristics of a high-speed wave piercing catamaran in irregular waves," *Royal Institution of Naval Architects. Transactions. Part A. International Journal of Maritime Engineering*, vol. 156, no. Part A1, pp. A25–A36, 2014.

[45] C. Ge, O. M. Faltinsen, and T. Moan, "Global Hydroelastic Response of Catamarans Due to Wetdeck Slamming," *Journal of Ship Research*, vol. 49, no. 1, pp. 24–42, 2005.

[46] G. Cusano, S. Monti, and A. Velasco, "Full scale and model test investigation of slamming effects on fast monohull vessels," *Proceedings of the 3rd International Conference on Hydroelasticity in Marine Technology*, pp. 163–173, 2003.

[47] D. Dessi, R. Mariani, and G. Coppotelli, "Experimental investigation of the bending vibrations of a fast vessel," *Australian Journal of Mechanical Engineering*, vol. 4, no. 2, p. 125, 2007.

[48] D. Dessi and R. Mariani, "Analysis and Prediction of Slamming-Induced Loads of a High-Speed Monohull in Regular Waves," *Journal of Ship Research*, vol. 52, no. 1, pp. 71–86, 2008.

[49] D. Dessi, "Whipping-based criterion for the identification of slamming events," *International Journal of Naval Architecture and Ocean Engineering*, vol. 6, no. 4, pp. 1082–1095, 2014.

[50] H. H. Sun and C. Guedes Soares, "An experimental study of ultimate torsional strength of a ship-type hull girder with a large deck opening," *Marine Structures*, vol. 16, no. 1, pp. 51–67, 2003.

[51] S. Zhu, M. Wu, and T. Moan, "Experimental and Numerical Study of Wave-Induced Load Effects of Open Ships in Oblique Seas," *Journal of Ship Research*, vol. 55, no. 2, pp. 100–123, 2011.

[52] G. Storhaug and T. Moan, "Springing/whipping response of a large ocean-going vessel investigated by an experimental method," *Proceedings of the 4th International Conference on Hydroelasticity in Marine Technology*, vol. 1, pp. 89–102, jan 2006.

[53] C. Guedes Soares, N. Fonseca, R. Pascoal, G. Clauss, C. E. Schmittner, and J. Hennig, "Analysis of wave induced loads on a FPSO due to abnormal waves," *... & Offloading (FPSO) ...*, pp. 1–8, 2004.

[54] G. Storhaug, E. Moe, and G. Holtsmark, "Measurements of Wave Induced Hull Girder Vibrations of an Ore Carrier in Different Trades," *Journal of Offshore Mechanics and Arctic Engineering*, vol. 129, no. 4, p. 279, 2007.

[55] S. Zhu and T. Moan, "A comparative study of the influence of bow shape on hull girder vibrations through two backbone models," in *Proceedings of the 6th International Conference on Hydroelasticity in Marine Technology*, no. 1251, (Tokyo, Japan), pp. 153–162, 2012.

[56] I. Drummen, M. Wu, and T. Moan, "Experimental and numerical study of containership responses in severe head seas," *Marine Structures*, vol. 22, no. 2, pp. 172–193, 2009.

[57] S. Zhu and T. Moan, "Investigation into the nonlinear hydroelastic response of an 8600-TEU containership model advancing in regular waves," *Ships and Offshore Structures*, vol. 9, no. 1, pp. 74–87, 2014.

[58] S. Zhu and T. Moan, "New insight into the wave-induced nonlinear vertical load effects of ultra-large container ships based on experiments," *Journal of Marine Science and Technology*, vol. 18, no. 1, pp. 87–114, 2013.

[59] S. Zhu and T. Moan, "Nonlinear effects from wave-induced maximum vertical bending moment on a flexible ultra-large containership model in severe head and oblique seas," *Marine Structures*, vol. 35, pp. 1–25, jan 2014.

[60] N. Fonseca and C. Guedes Soares, "Comparison of numerical and experimental results of nonlinear wave-induced vertical ship motions

and loads," *Journal of Marine Science and Technology*, vol. 6, no. 4, pp. 193–204, 2002.

[61] N. Fonseca and C. Guedes Soares, "Experimental investigation of the nonlinear effects on the vertical motions and loads of a containership in regular waves," *Journal of Ship Research*, vol. 48, no. 2, pp. 118–147, 2004.

[62] N. Fonseca and C. Guedes Soares, "Experimental Investigation of the Shipping of Water on the Bow of a Containership," *Journal of Offshore Mechanics and Arctic Engineering*, vol. 127, no. 4, p. 322, 2005.

[63] S. S. Denchfield, D. A. Hudson, P. Temarel, W. Bateman, and S. E. Hirdaris, "Evaluation of rogue wave induced loads using 2D hydroelasticity analysis," in *Proceedings of the 5th International Conference on Hydroelasticity in Marine Technology*, (Southampton, United Kingdom), University of Southampton, sep 2009.

[64] S. S. Bennett, D. A. Hudson, and P. Temarel, "The influence of forward speed on ship motions in abnormal waves: Experimental measurements and numerical predictions," *Journal of Fluids and Structures*, vol. 39, pp. 154–172, 2013.

[65] S. S. Bennett, D. A. Hudson, and P. Temarel, "Global wave-induced loads in abnormal waves: Comparison between experimental results and classification society rules," *Journal of Fluids and Structures*, vol. 49, pp. 498–515, 2014.

[66] G. Clauss, C. E. Schmittner, J. Hennig, C. Guedes Soares, N. Fonseca, and R. Pascoal, "Bending moments of an FPSO in rogue waves," in *Proceeding of the 23rd International Conference on Offshore Mechanics and Arctic Engineering (OMAE 2004)*, pp. 1–8, 2004.

[67] G. Clauss, A. Kauffeldt, and K. Jacobsen, "Longitudinal forces and bending moments of a FPSO," in *Proceeding of the 26rd International Conference on Offshore Mechanics and Arctic Engineering (OMAE 2007)*, pp. 1–10, 2007.

[68] I. Drummen, G. Storhaug, and T. Moan, "Experimental and numerical investigation of fatigue damage due to wave-induced vibrations in a containership in head seas," *Journal of Marine Science and Technology*, vol. 13, no. 4, pp. 428–445, 2008.

[69] G. Storhaug, Š. Malenica, B.-K. Choi, S. Zhu, and O. A. Hermundstad, "Consequence of whipping and springing on fatigue and extreme loading for a 13000TEU container vessel based on model tests," in

11th International Symposium on practical design of ships and other floating structures, (Rio de Janeiro), pp. 1201–1209, 2010.

[70] G. Storhaug, Q. Derbanne, B.-K. Choi, T. Moan, and O. A. Hermundstad, "Effect of Whipping on Fatigue and Extreme Loading of a 13000Teu Container Vessel in Bow Quartering Seas Based on Model Tests," in *Proceedings of the 30th International Conference on Ocean, Offshore and Arctic Engineering*, (Rotterdam, The Netherlands), pp. 1–10, 2011.

[71] G. Storhaug, "The measured contribution of whipping and springing on the fatigue and extreme loading of container vessels," *International Journal of Naval Architecture and Ocean Engineering*, vol. 6, pp. 1096–1110, 2014.

[72] S. S. Bennett, J. Downes, T. Dickson, A. B. Phillips, and S. Turnock, "Rapid Prototyping of Flexible Models – A New Method for Model Testing ?," in *7th International Conference on Hydroelasticity in Marine Technology*, (Split, Croatia), 2015.

[73] X. Yan and P. Gu, "A review of rapid prototyping technologies and systems," *CAD Computer Aided Design*, vol. 28, no. 4, pp. 307–318, 1996.

[74] L. Hieu, N. Zlatov, J. V. Sloten, E. Bohez, L. Khanh, P. Binh, P. Oris, and Y. Toshev, "Medical rapid prototyping applications and methods," *Assembly Automation*, vol. 25, no. 4, pp. 284–292, 2005.

[75] S. J. Leigh, R. J. Bradley, C. P. Purssell, D. R. Billson, and D. a. Hutchins, "A Simple, Low-Cost Conductive Composite Material for 3D Printing of Electronic Sensors," *PLoS ONE*, vol. 7, no. 11, pp. 1–6, 2012.

[76] 3Dsystems, "3D Printer Buyer ' s Guide For Professional and Production Applications," 2015.

[77] T. Plunkett, "SLA vs SLS: Which to Use for a Functional Prototype? - TCT - 3D Printing, Additive Manufacturing and Product Development Technology," 2015.

[78] 3Dprintingindustry.com, *The Free Beginner's Guide to 3D Printing.* 2014.

[79] J. P. Moore and C. B. Williams, "Fatigue Characterization of 3D Printed Elastomer Material," *Solid Freeform Fabrication Symposium*, pp. 641–655, 2008.

[80] A. Sebert, "What is the influence of infill %, layer height and infill pattern on my 3D prints?," 2015.

[81] J. F. Rodríguez, J. P. Thomas, and J. E. Renaud, "Mechanical behavior of acrylonitrile butadiene styrene (ABS) fused deposition materials modeling," *Rapid Prototyping Journal*, vol. 9, no. 4, pp. 219–230, 2003.

[82] H. Nance, "Stress Testing Injected Hot Glue for Solid, Fast, Cheap 3D Prints — Make: DIY Projects, How-Tos, Electronics, Crafts and Ideas for Makers," 2014.

[83] S.-H. Ahn, M. Montero, D. Odell, S. Roundy, and P. K. Wright, "Anisotropic material properties of fused deposition modeling ABS," *Rapid Prototyping Journal*, vol. 8, no. 4, pp. 248–257, 2002.

[84] O. S. Es-Said, J. Foyos, R. Noorani, M. Mendelson, R. Marloth, and B. A. Pregger, "Effect of Layer Orientation on Mechanical Properties of Rapid Prototyped Samples," *Materials and Manufacturing Processes*, vol. 15, no. 1, pp. 107–122, 2000.

[85] J. F. Rodríguez, J. P. Thomas, and J. E. Renaud, "Design of Fused-Deposition ABS Components for Stiffness and Strength," *Journal of Mechanical Design*, vol. 125, no. 3, p. 545, 2003.

[86] A. Sebert, "What is the influence of color, printing speed, extrusion temperature and ageing on my 3D prints?," 2015.

[87] B. M. Tymrak, M. Kreiger, and J. M. Pearce, "Mechanical properties of components fabricated with open-source 3-D printers under realistic environmental conditions," *Materials and Design*, vol. 58, pp. 242–246, 2014.

[88] G. D. Kim and Y. T. Oh, "A benchmark study on rapid prototyping processes and machines: quantitative comparisons of mechanical properties, accuracy, roughness, speed, and material cost.," *Proceedings of the Institution of Mechanical Engineers – Part B – Engineering Manufacture (Professional Engineering Publishing)*, vol. 222, no. 2, pp. 201–215, 2008.

[89] C. Lee, S. Kim, H. Kim, and S.-H. Ahn, "Measurement of anisotropic compressive strength of rapid prototyping parts," *Journal of Materials Processing Technology*, vol. 187-188, pp. 627–630, 2007.

[90] L. J. Gibson and M. F. Ashby, *Cellular solids: Structure and properties*. Cambridge University Press, second ed., 1999.

[91] T. G. Carne, D. T. Griffith, and M. E. Cassias, "Support Conditions for Free Boundary-Condition Modal Testing," *IMAC-XXV: A Conference & Exposition on Structural Dynamics*, no. January 2015, 2007.

[92] "ISO 178:2001: Plastics-Determination of flexural properties," 2003.

[93] "ASTM E1876-15: Standard Test Method for Dynamic Young's Modulus, Shear Modulus, and Poisson's Ratio by Impulse Excitation of Vibration," 2015.

[94] C. Betts, R. E. D. Bishop, and W. G. Price, "A Survey of Internal Hull Damping," *RINA Supplementary Papers*, no. 119, pp. 125–142, 1976.

[95] I. Senjanović, Š. Malenica, and S. Tomašević, "Investigation of ship hydroelasticity," *Ocean Engineering*, vol. 35, no. 5-6, pp. 523–535, 2008.

[96] E. Korkut, M. Atlar, and A. İncecik, "An experimental study of motion behaviour with an intact and damaged Ro-Ro ship model," *Ocean Engineering*, vol. 31, pp. 483–512, feb 2004.

[97] B. J. French, G. A. Thomas, and M. R. Davis, "Slam occurrences and loads of a high-speed wave piercer catamaran in irregular seas," *Proceedings of the Institution of Mechanical Engineers, Part M: Journal of Engineering for the Maritime Environment*, vol. 229, no. 1, pp. 45–57, 2013.

[98] G. Jacobi, G. A. Thomas, M. R. Davis, and G. Davidson, "An insight into the slamming behaviour of large high-speed catamarans through full-scale measurements," *Journal of Marine Science and Technology*, vol. 19, no. 1, pp. 15–32, 2014.

[99] S. S. Denchfield, *An Investigation into the Influence of Rogue Waves on a Traveling Ship*. PhD thesis, Faculty of Engineering, Science and Mathematics School of Engineering Sciences, 2011.

[100] S. S. Denchfield, B. Winden, C. Brooks, S. Turnock, D. A. Hudson, A. Forrester, and D. Taunton, "Wireless sensor network for determining boat motions and hydroelastic responses .," *Advanced Measurement Technology*, pp. 1–14, 2011.

[101] S. S. Bennett, C. Brooks, B. Winden, D. Taunton, A. Forrester, S. Turnock, and D. A. Hudson, "Measurement of ship hydroelastic response using multiple wireless sensor nodes," *Ocean Engineering*, vol. 79, pp. 67–80, 2014.

Appendices

Appendix A

Model comparison table

Table A.1: Summary of hydroelastic models used

#	Vessel type	Manufacturer	Publications	Segments	Stiffness	Connection	Backbone Geometry	Position
1	Container ship, S-175	Watanabe (1989)	[4, 60]	1	Variable	Elastic		
2	Container ship, S-175	Chen (2001)	[5, 23, 32]	1	Variable	Elastic		
3	Container ship, pentamaran	Dudson (2001)	[15]	4	Uniform	Force transducers		
4	Blunt ship	Zhu (2002)	[16]	2	Uniform	Force transducers		
5	Fast ferry, MDV3000	Ciappi (2003)	[3, 13, 34, 35, 46–49]	6	Variable	Aluminium backbone	Rectangular, hollow	Neutral axis
6	Barge	Malenica (2003)	[27, 31, 95]	12	Uniform	Two steel backbones	Rectangular plates	Main deck
7	Container ship, S-175	Fonseca (2004)	[61]	3	Uniform	Steel backbone	Rectangular, hollow	Main deck
8	FPSO	Clauss(2004)	[53, 66, 67]	3	Uniform	Connecting elements	Steel plates	Sides at WL height
9	Container ship	Iijima(2004)	[17]	4	Uniform	Force transducers		
10	Container ship	Fonseca(2005)	[62]	4	Uniform	Steel backbone	Rectangular, hollow	Main deck

#	Vessel type	Manufacturer	Publications	Segments	Stiffness	Connection	Backbone Geometry	Position
11	Ro-Ro	Korkut (2004)	[18, 96]	2	Uniform	Force gauge		
12	Catamaran	Ge (2005)	[45]	3	Uniform	Force transducers		
13	Container ship	Kinoshita (2006)	[25]	10	Uniform	Aluminium backbone	Pipe	Neutral axis
14	Bulk carrier	Storhaug (2006)	[52]	4	Uniform	Steel frame		
15	Catamaran, INCAT112	Lavroff (2007)	[2, 37–44, 97, 98]	3	Both	Torsion springs		
16	Container ship, large	Drummen (2008)	[56, 68]	4	Uniform	Rotational springs		
17	Frigate, Leander class	Denchfield (2010)	[14, 64, 65, 72, 99–101]	5	Uniform	Aluminium backbone	Rectangular, hollow	Neutral axis
18	Container ship, large	Iijima (2009)	[28, 29, 51, 55]	17	Uniform	Aluminium backbone	Rect.-hollow, transverse cuts	Main deck
19	Container ship, 12,000-TEU	Miyake (2009)	[26]	8	Uniform	Steel backbone	N/A	Neutral axis
20	Container ship, 12,000-TEU	Oka (2009)	[20]	4	Variable	Aluminium backbone	Two C-beams	Neutral axis
21	Container ship, 13,000-TEU	Storhaug (2010)	[21, 57, 58, 69–71]	4	Uniform	Rotational springs		

#	Vessel type	Manufacturer	Publications	Segments	Stiffness	Connection	Backbone Geometry	Position
22	Container ship, 5,000-TEU	Takaoka (2012)	[19]	8	Both	Two steel backbones	Rectangular	Bottom
23	Container ship, 8,600-TEU	Zhu (2013)	[58]	4	Uniform	Rotational springs		
24	Container ship, river-sea link	Peng (2014)	[1]	6	Uniform	Aluminium backbone	Circular, hollow	VCG
25	Container ship, 9,000-TEU	Marón (2014)	[30]	4	Uniform	Aluminium backbone	Rect.-hollow, upper side cuts	Bottom
26	Barge	Iijima (2015)	[24]	2	Uniform	Flexible joints		
27	Container ship, 6,600-TEU	Houtani (2018)	[33]	1	Variable	Elastic		

Appendix B

Graphs regarding preliminary design iterations

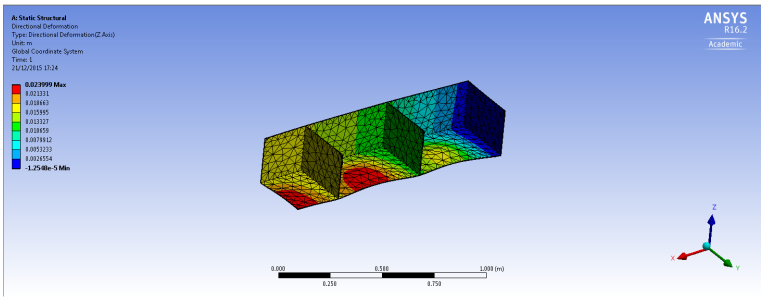

Figure B.1: Deflections of the ballasted barge under hydrostatic pressure

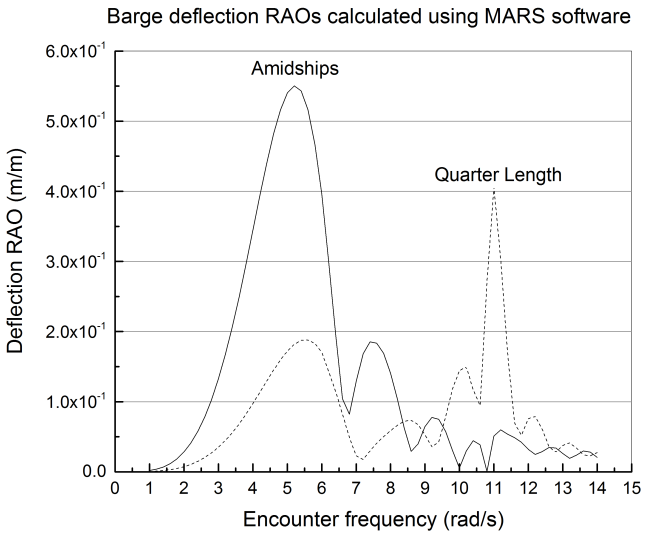

Figure B.2: Deflection RAOs of the barge amidships and at quarter length

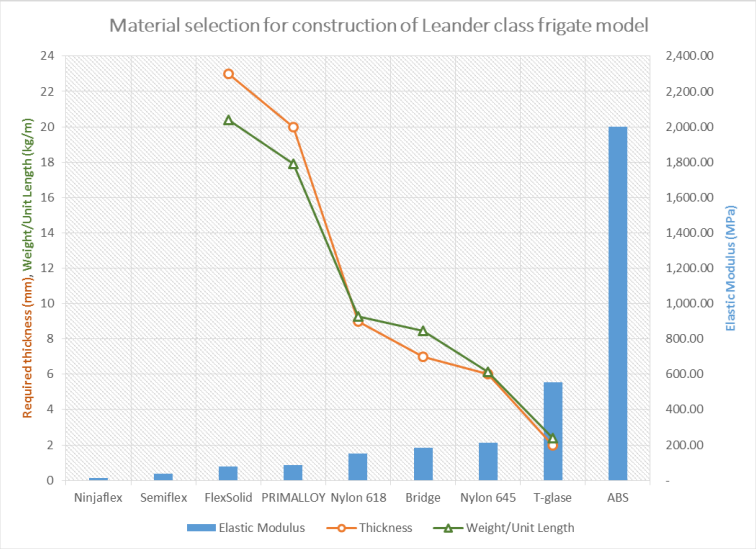

Figure B.3: Effect of material selection on required wall thickness and mass per unit length for the frigate

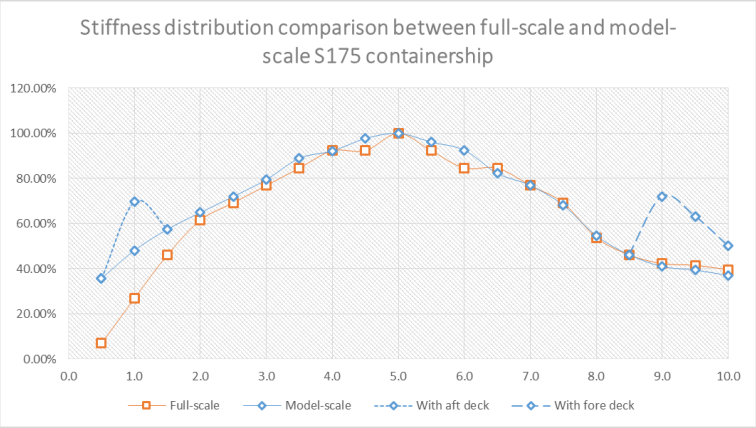

Figure B.4: Stiffness distribution comparison between full-scale and model-scale vessel

Appendix C

Coupon dimension measurements and test result graphs

Table C.1: Summary of coupon dimension measurements for ABS and layering direction along the z-axis of the coupon

Design	coupon	Infill	Measured Dimensions												
			h mm					b mm					l mm		L mm	
			1	2	3	avg	err	1	2	3	avg	err	-	/h_{avg}	-	/h_{avg}
1	101	1	3.98	3.98	3.99	3.98	0.08%	9.97	9.96	9.96	9.96	0.03%	80.07	20.10	63.95	16.05
1	102	1	3.98	4.00	4.02	4.00	0.00%	9.99	10.00	9.96	9.98	0.17%	80.07	20.02	63.95	15.99
1	103	1	3.99	4.00	4.00	4.00	0.08%	9.98	9.97	9.96	9.97	0.00%	80.05	20.03	63.95	16.00
1	104	1	3.99	4.00	4.00	4.00	0.08%	9.94	9.94	9.95	9.94	0.03%	80.03	20.02	63.95	16.00
1	105	1	3.97	4.01	3.99	3.99	0.50%	9.98	9.98	9.97	9.98	0.03%	80.06	20.07	63.95	16.03
1	106	1	3.99	4.01	4.00	4.00	0.25%	9.99	10.00	9.98	9.99	0.10%	80.03	20.01	63.95	15.99
2	201	2	4.00	4.01	4.01	4.01	0.08%	9.95	9.95	9.94	9.95	0.03%	80.07	19.98	63.95	15.96
2	202	2	4.00	4.03	4.01	4.01	0.42%	9.98	10.00	9.98	9.99	0.13%	80.01	19.94	63.95	15.93
2	203	2	4.00	4.02	4.00	4.01	0.33%	10.00	10.04	10.00	10.01	0.27%	80.02	19.97	63.95	15.96
2	204	2	4.00	4.01	4.00	4.00	0.17%	9.99	9.97	9.94	9.97	0.03%	80.04	19.99	63.95	15.97
2	205	2	4.00	4.01	3.99	4.00	0.25%	9.96	9.96	9.95	9.96	0.03%	80.11	20.03	63.95	15.99
2	206	2	4.00	4.01	4.01	4.01	0.08%	10.01	10.00	9.96	9.99	0.10%	80.10	19.99	63.95	15.96
3	301	3	3.98	3.99	3.99	3.99	0.08%	9.97	9.94	9.97	9.96	0.20%	80.08	20.09	63.95	16.04
3	302	3	4.01	4.02	4.00	4.01	0.25%	9.98	9.97	10.01	9.99	0.17%	80.02	19.96	63.95	15.95
3	303	3	4.00	4.02	4.00	4.01	0.33%	9.98	9.96	9.98	9.97	0.13%	80.01	19.97	63.95	15.96
3	304	3	3.99	4.02	4.00	4.00	0.42%	9.95	9.95	9.96	9.95	0.03%	80.09	20.01	63.95	15.97
3	305	3	4.01	4.02	4.02	4.02	0.08%	9.97	9.97	9.96	9.97	0.03%	80.06	19.93	63.95	15.92
3	306	3	4.01	4.00	4.00	4.00	0.08%	9.94	9.94	9.94	9.94	0.00%	80.06	20.00	63.95	15.97
4	401	4	3.98	4.00	3.99	3.99	0.25%	9.97	9.96	9.96	9.96	0.03%	80.11	20.08	63.95	16.03
4	402	4	3.97	3.99	3.99	3.98	0.17%	9.96	9.95	9.97	9.96	0.10%	80.09	20.11	63.95	16.05
4	403	4	3.99	4.00	3.99	3.99	0.17%	9.99	10.00	9.98	9.99	0.10%	80.08	20.05	63.95	16.01
4	404	4	3.99	3.99	3.99	3.99	0.00%	10.02	9.99	10.00	10.00	0.13%	80.07	20.07	63.95	16.03
4	405	4	3.97	3.98	3.95	3.97	0.34%	10.00	9.98	9.99	9.99	0.10%	80.12	20.20	63.95	16.12
4	406	4	4.00	4.01	4.00	4.00	0.17%	9.99	9.99	9.98	9.99	0.03%	80.08	20.00	63.95	15.97

Table C.2: Summary of coupon dimension measurements for ABS and layering direction along the y-axis and x-axis of the coupon

Design	coupon	Infill	Measured Dimensions												
			h mm					b mm					l mm		L mm	
			1	2	3	avg	err	1	2	3	avg	err	-	/h_{avg}	-	/h_{avg}
5	501	3	4.12	4.19	4.19	4.17	0.56%	10.08	10.05	10.09	10.07	0.23%	80.01	19.20	63.95	15.35
5	502	3	4.21	4.27	4.25	4.24	0.63%	10.03	10.05	10.00	10.03	0.23%	79.99	18.85	63.95	15.07
5	503	3	4.29	4.30	4.27	4.29	0.31%	10.04	10.08	10.07	10.06	0.17%	80.06	18.68	63.95	14.92
5	504	3	4.29	4.31	4.29	4.30	0.31%	10.08	10.08	10.08	10.08	0.00%	80.04	18.63	63.95	14.88
5	505	3	4.13	4.14	4.10	4.12	0.40%	10.07	10.08	10.10	10.08	0.03%	80.09	19.42	63.95	15.51
5	506	3	4.13	4.17	4.15	4.15	0.48%	10.13	10.09	10.17	10.13	0.39%	80.01	19.28	63.95	15.41
6	601	4	4.38	4.36	4.37	4.37	0.23%	10.15	10.06	10.22	10.14	0.82%	80.10	18.33	63.95	14.63
6	602	4	4.08	4.12	4.09	4.10	0.57%	10.06	10.01	10.00	10.02	0.13%	79.98	19.52	63.95	15.61
6	603	4	3.99	4.01	4.03	4.01	0.00%	10.02	10.05	10.04	10.04	0.13%	79.96	19.94	63.95	15.95
6	604	4	4.16	4.17	4.16	4.16	0.16%	10.00	10.10	10.10	10.07	0.33%	80.03	19.22	63.95	15.36
6	605	4	4.09	4.12	4.08	4.10	0.57%	10.11	10.05	10.02	10.06	0.10%	80.00	19.53	63.95	15.61
6	606	4	4.04	4.02	4.01	4.02	0.08%	10.05	10.07	10.08	10.07	0.03%	79.98	19.88	63.95	15.89
7	701	3	3.96	3.93	4.00	3.96	0.84%	9.94	9.94	9.97	9.95	0.10%	80.15	20.22	63.95	16.14
7	702	3	3.94	3.92	3.94	3.93	0.34%	9.91	9.91	9.92	9.91	0.03%	80.15	20.38	63.95	16.26
7	703	3	3.98	3.93	3.93	3.95	0.42%	9.95	9.91	9.93	9.93	0.20%	80.12	20.30	63.95	16.20
7	704	3	3.95	3.93	3.90	3.93	0.08%	9.94	9.91	9.90	9.92	0.07%	80.12	20.40	63.95	16.29
7	705	3	3.99	3.97	3.92	3.96	0.25%	9.96	9.93	9.94	9.94	0.13%	80.11	20.23	63.95	16.15
7	706	3	3.92	3.91	3.92	3.92	0.17%	9.95	9.88	8.90	9.91	0.24%	80.16	20.47	63.95	16.33
8	801	4	4.00	3.91	3.87	3.93	0.42%	9.93	9.91	9.87	9.90	0.07%	80.21	20.43	63.95	16.29
8	802	4	3.94	3.91	3.92	3.92	0.34%	10.06	9.76	9.74	9.85	0.95%	80.39	20.49	63.95	16.30
8	803	4	3.89	3.90	3.96	3.92	0.43%	9.91	9.95	9.94	9.93	0.17%	80.44	20.54	63.95	16.33
8	804	4	4.00	3.98	3.92	3.97	0.34%	9.76	9.69	9.88	9.78	0.89%	80.36	20.26	63.95	16.12
8	805	4	3.97	3.96	3.92	3.95	0.25%	9.67	9.74	9.96	9.79	0.51%	80.57	20.40	63.95	16.19
8	806	4	4.05	3.91	3.88	3.95	0.93%	9.98	9.97	9.87	9.94	0.30%	80.33	20.35	63.95	16.20

Table C.3: Summary of coupon dimension measurements for T-glase and layering direction along the z-axis of the coupon

Design	coupon	Infill	Measured Dimensions												
			h mm					b mm					l mm		L mm	
			1	2	3	avg	err	1	2	3	avg	err	-	/h_{avg}	-	/h_{avg}
1	101	1	4.00	4.01	3.99	4.00	0.25%	9.92	9.90	9.89	9.90	0.03%	79.88	19.97	63.95	15.99
1	102	1	3.95	4.00	4.09	4.01	0.33%	9.94	9.95	9.91	9.93	0.17%	80.01	19.94	63.95	15.93
1	103	1	3.97	4.00	4.09	4.02	0.50%	9.93	9.95	9.97	9.95	0.00%	80.01	19.90	63.95	15.91
1	104	1	4.00	4.02	4.05	4.02	0.08%	9.97	9.98	9.98	9.98	0.03%	80.11	19.91	63.95	15.89
1	105	1	4.04	4.02	4.00	4.02	0.00%	9.97	9.99	9.99	9.98	0.07%	80.03	19.91	63.95	15.91
1	106	1	3.99	4.00	3.98	3.99	0.25%	9.91	9.92	10.02	9.95	0.30%	80.06	20.07	63.95	16.03
2	201	2	4.09	4.08	4.10	4.09	0.24%	9.94	9.96	10.00	9.97	0.07%	80.03	19.57	63.95	15.64
2	202	2	4.13	4.18	4.16	4.16	0.56%	9.88	9.97	9.95	9.93	0.37%	80.04	19.26	63.95	15.38
2	203	2	4.01	4.04	4.07	4.04	0.00%	9.90	9.92	9.93	9.92	0.03%	80.02	19.81	63.95	15.83
2	204	2	4.04	4.09	4.09	4.07	0.41%	9.98	9.97	9.98	9.98	0.07%	80.03	19.65	63.95	15.70
2	205	2	4.03	4.05	4.04	4.04	0.25%	9.92	9.90	9.89	9.90	0.03%	80.06	19.82	63.95	15.83
2	206	2	4.03	4.02	4.07	4.04	0.50%	9.99	9.98	9.94	9.97	0.10%	80.02	19.81	63.95	15.83
3	301	3	4.03	4.03	4.10	4.05	0.58%	9.96	9.98	10.00	9.98	0.00%	80.01	19.74	63.95	15.78
3	302	3	3.99	4.03	4.06	4.03	0.08%	9.95	9.95	9.92	9.94	0.10%	79.98	19.86	63.95	15.88
3	303	3	3.99	3.99	3.99	3.99	0.00%	9.91	9.91	9.92	9.91	0.03%	79.90	20.03	63.95	16.03
3	304	3	4.00	4.00	4.11	4.04	0.91%	9.98	10.00	10.00	9.99	0.07%	80.07	19.84	63.95	15.84
3	305	3	4.01	4.00	3.99	4.00	0.00%	9.95	9.98	10.00	9.98	0.03%	80.02	20.01	63.95	15.99
3	306	3	3.99	4.00	4.02	4.00	0.08%	9.91	9.91	10.00	9.94	0.30%	80.00	19.98	63.95	15.97
3	307	3	4.00	4.01	4.03	4.01	0.08%	9.92	9.94	9.97	9.94	0.03%	79.94	19.92	63.95	15.93
4	401	4	4.02	4.03	4.02	4.02	0.17%	9.96	9.96	9.98	9.97	0.07%	79.99	19.88	63.95	15.89
4	402	4	4.04	4.05	4.02	4.04	0.33%	9.91	9.92	9.90	9.91	0.10%	80.05	19.83	63.95	15.84
4	403	4	3.99	4.03	4.01	4.01	0.50%	9.88	9.89	9.98	9.92	0.27%	80.00	19.95	63.95	15.95
4	404	4	4.01	4.05	4.05	4.04	0.33%	9.96	9.99	9.97	9.97	0.17%	80.01	19.82	63.95	15.84
4	405	4	4.02	4.04	4.04	4.03	0.17%	9.88	9.89	9.92	9.90	0.07%	80.00	19.83	63.95	15.86
4	406	4	4.01	4.06	4.03	4.03	0.66%	9.97	9.96	9.95	9.96	0.00%	80.14	19.87	63.95	15.86

Table C.4: Summary of coupon dimension measurements for T-glase and layering direction along the y-axis and x-axis of the coupon

Design	coupon	Infill	Measured Dimensions												
			h mm					b mm					l mm		L mm	
			1	2	3	avg	err	1	2	3	avg	err	-	/h_{avg}	-	/h_{avg}
5	501	3	3.93	3.93	3.92	3.93	0.08%	10.00	10.06	10.00	10.02	0.40%	80.02	20.38	63.95	16.29
5	502	3	3.97	3.97	3.96	3.97	0.08%	9.96	10.05	9.93	9.98	0.70%	80.06	20.18	63.95	16.12
5	503	3	3.96	3.96	3.98	3.97	0.17%	9.97	10.05	9.94	9.99	0.63%	79.98	20.16	63.95	16.12
5	504	3	3.94	3.93	3.92	3.93	0.00%	9.99	10.04	9.96	10.00	0.43%	80.01	20.36	63.95	16.27
5	505	3	3.95	3.96	3.95	3.95	0.17%	9.92	10.05	10.04	10.00	0.47%	80.01	20.24	63.95	16.18
5	506	3	3.97	3.96	3.95	3.96	0.00%	9.97	10.09	10.04	10.03	0.56%	79.96	20.19	63.95	16.15
6	601	4	3.95	3.95	3.94	3.95	0.08%	10.02	10.05	10.02	10.03	0.20%	79.94	20.26	63.95	16.20
6	602	4	3.94	3.94	3.94	3.94	0.00%	9.99	10.07	10.01	10.02	0.47%	80.00	20.30	63.95	16.23
6	603	4	3.95	3.95	3.94	3.95	0.08%	9.99	10.06	10.01	10.02	0.40%	80.01	20.27	63.95	16.20
6	604	4	3.95	3.96	3.96	3.96	0.08%	9.98	10.12	10.00	10.03	0.86%	80.02	20.22	63.95	16.16
6	605	4	3.96.	3.96	3.96	3.96	0.00%	10.10	10.12	9.95	10.06	0.63%	80.01	20.20	63.95	16.15
6	606	4	3.97	3.96	3.97	3.97	0.17%	9.99	10.09	10.00	10.03	0.63%	80.02	20.17	63.95	16.12
7	701	3	3.97	3.97	3.99	3.98	0.17%	9.77	9.80	9.74	9.77	0.31%	80.20	20.17	63.95	16.08
7	702	3	4.15	4.14	4.00	4.10	1.06%	9.66	9.67	9.80	9.71	0.41%	80.29	19.60	63.95	15.61
7	703	3	3.98	4.04	3.96	3.99	1.17%	9.79	9.72	9.75	9.75	0.34%	80.27	20.10	63.95	16.01
7	704	3	3.94	3.94	3.95	3.94	0.08%	9.75	9.69	9.70	9.71	0.24%	80.25	20.35	63.95	16.22
7	705	3	3.97	4.00	3.99	3.99	0.33%	9.75	9.81	9.73	9.76	0.48%	80.23	20.12	63.95	16.04
7	706	3	3.97	3.98	3.96	3.97	0.25%	9.74	9.71	9.78	9.74	0.34%	80.33	20.23	63.95	16.11
8	801	4	3.95	3.91	3.97	3.94	0.85%	9.64	9.64	9.78	9.69	0.48%	80.47	20.41	63.95	16.22
8	802	4	3.98	4.13	4.17	4.09	0.90%	9.83	9.73	9.72	9.76	0.31%	80.22	19.60	63.95	15.62
8	803	4	3.96	3.96	4.07	4.00	0.92%	9.79	9.74	9.68	9.74	0.03%	80.21	20.07	63.95	16.00
8	804	4	3.94	3.94	3.95	3.94	0.08%	9.75	9.81	9.80	9.79	0.24%	80.66	20.45	63.95	16.22
8	805	4	3.97	3.96	3.96	3.96	0.08%	9.77	9.81	9.78	9.79	0.24%	80.28	20.26	63.95	16.14
8	806	4	3.95	3.95	3.94	3.95	0.08%	9.74	9.73	9.74	9.74	0.07%	80.36	20.36	63.95	16.20

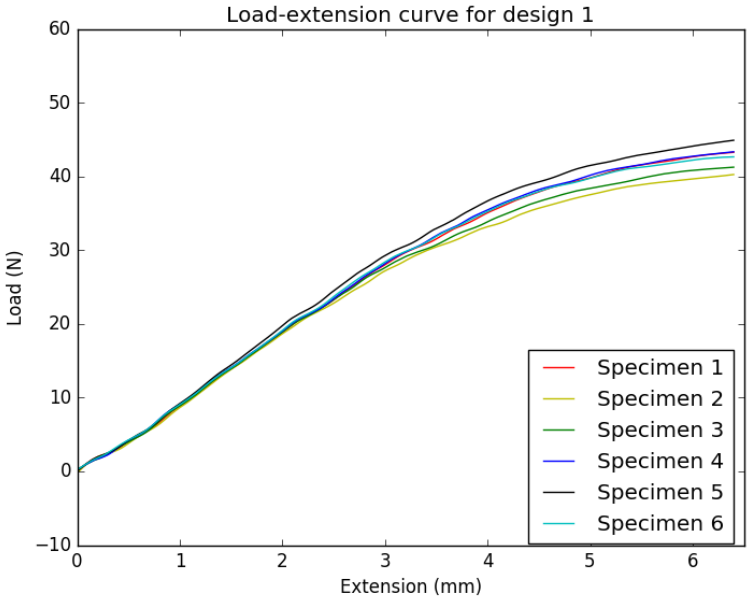

(a) Design 1

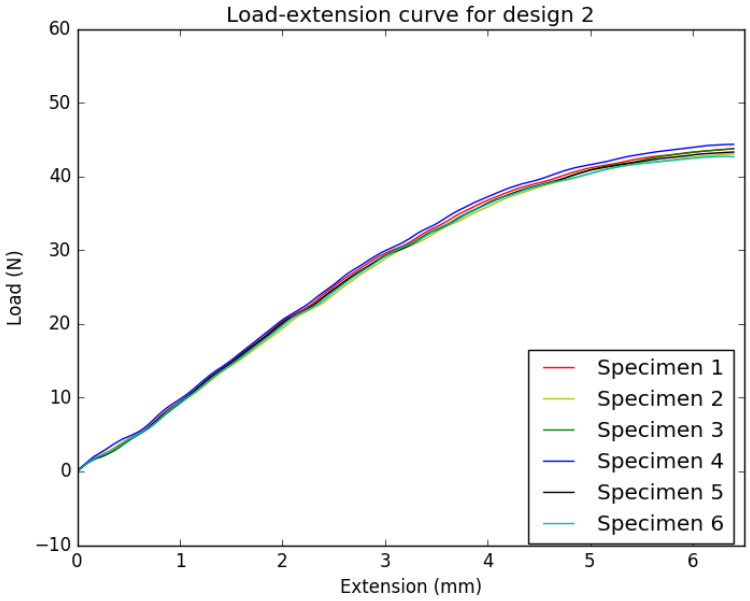

(b) Design 2

Figure C.1: Load-extension curves for ABS designs 1 & 2

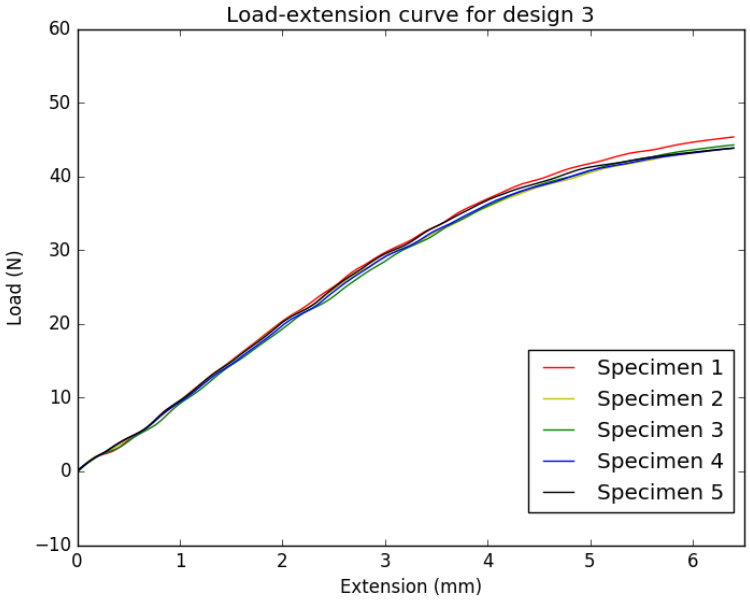

(a) Design 3

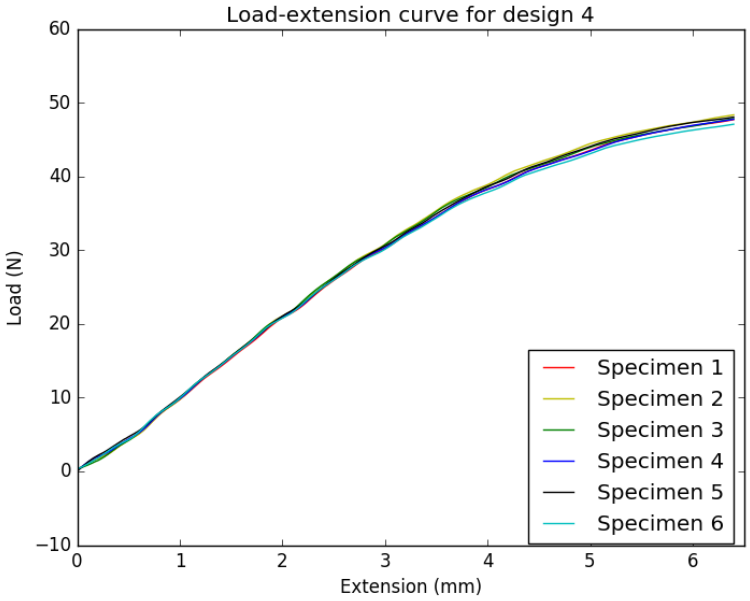

(b) Design 4

Figure C.2: Load-extension curves for ABS designs 3 & 4

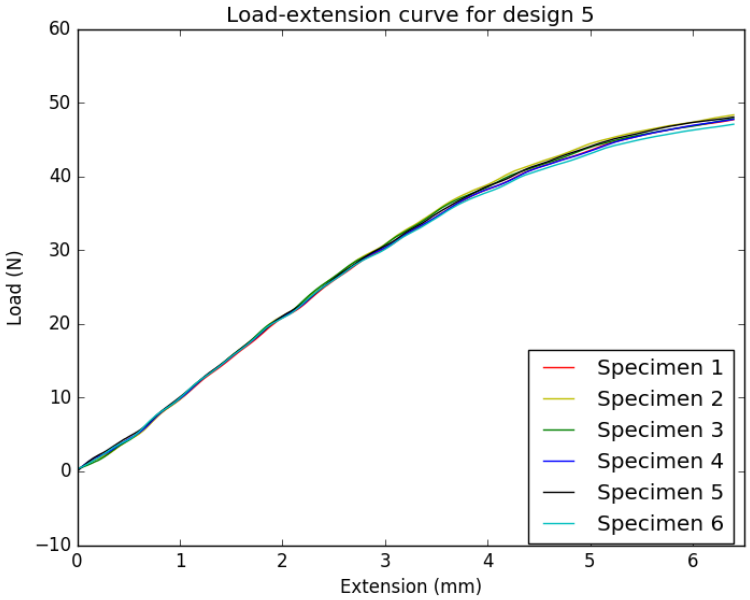

(a) Design 3

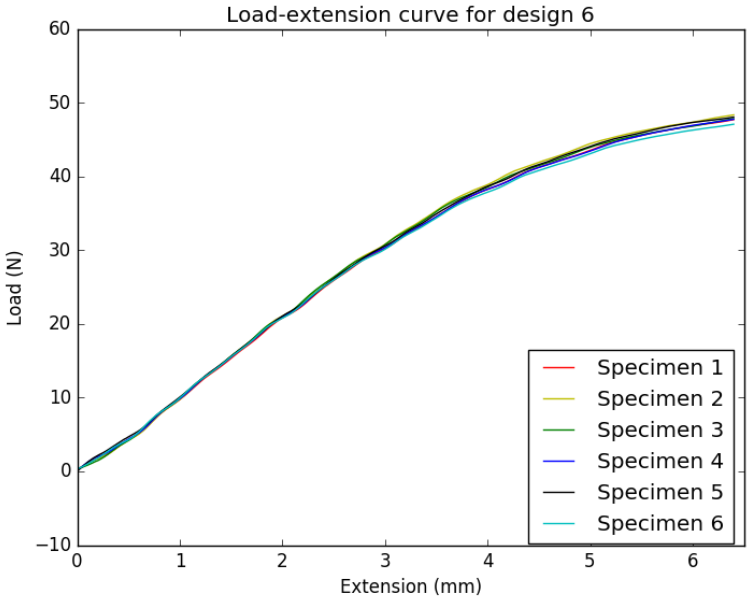

(b) Design 4

Figure C.3: Load-extension curves for ABS designs 5 & 6

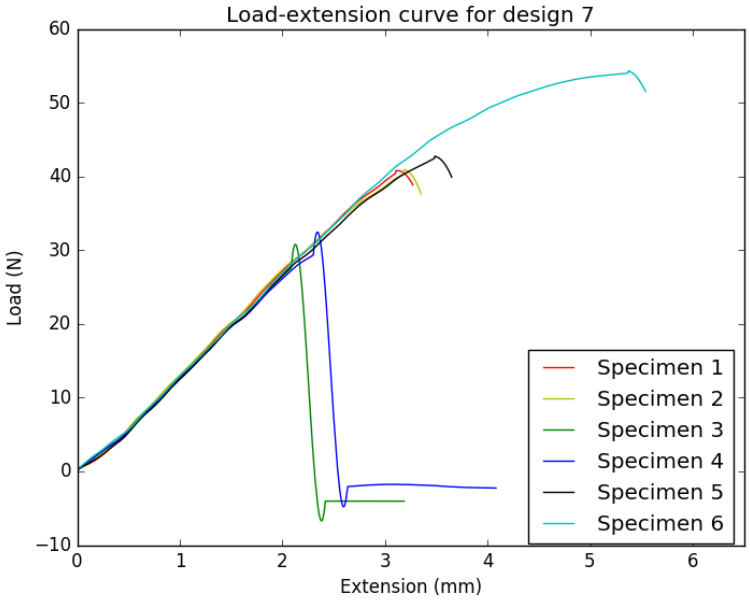

(a) Design 3

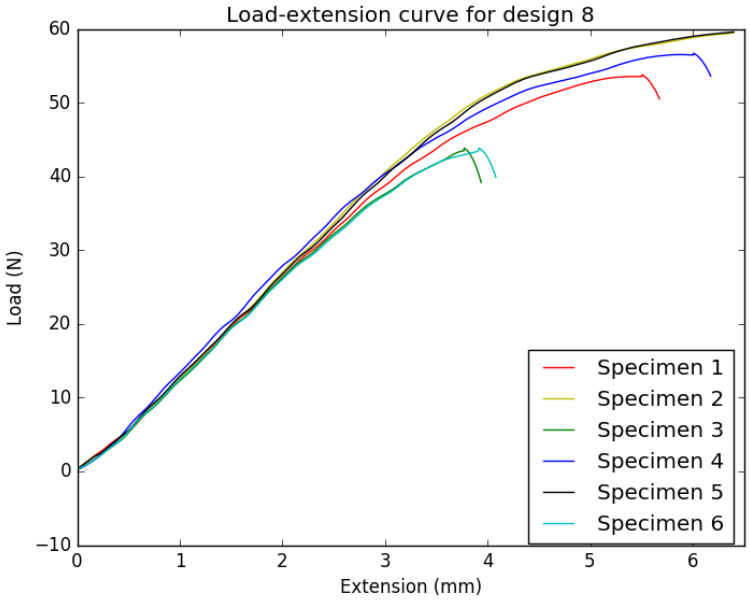

(b) Design 4

Figure C.4: Load-extension curves for ABS designs 7 & 8

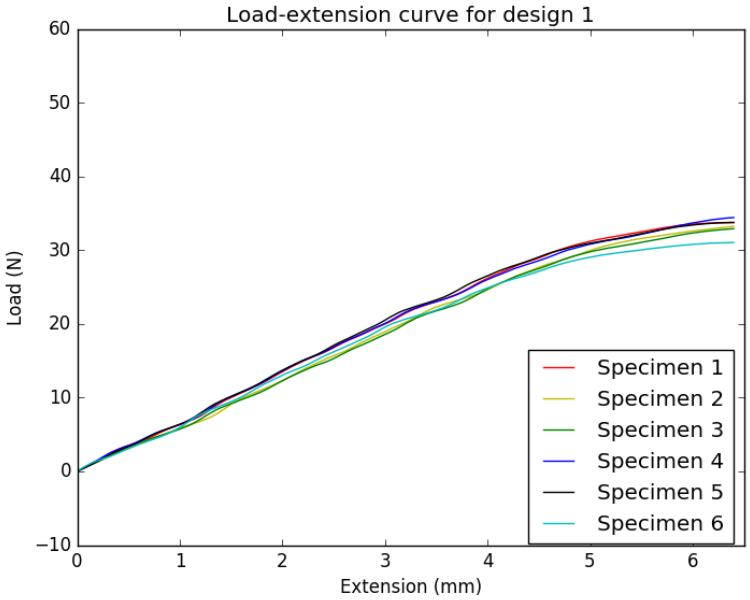

(a) Design 1

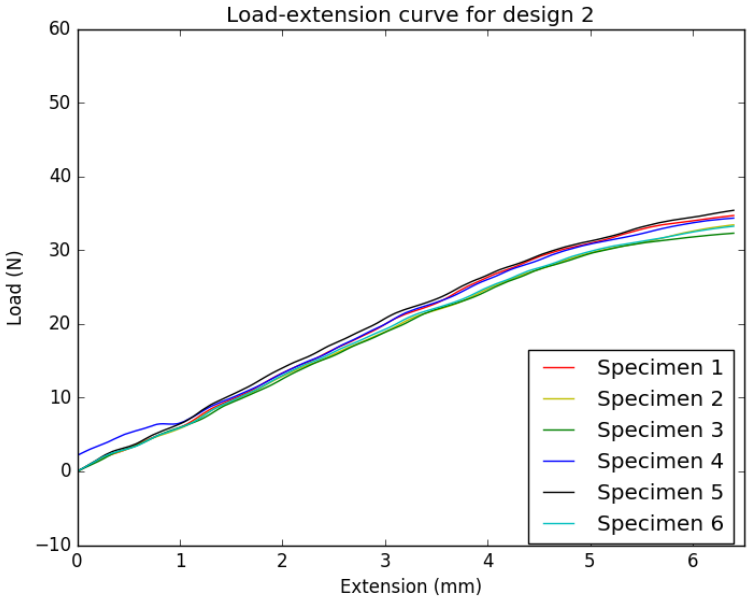

(b) Design 2

Figure C.5: Load-extension curves for T-glase designs 1 & 2

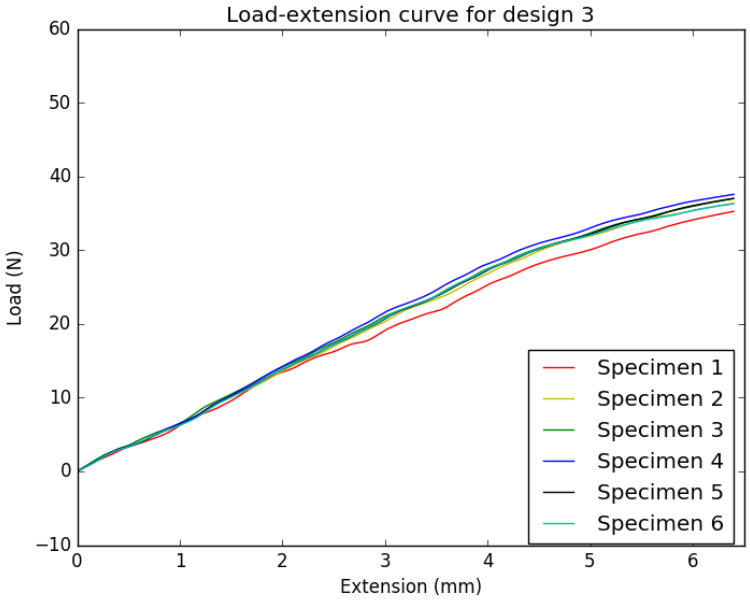

(a) Design 3

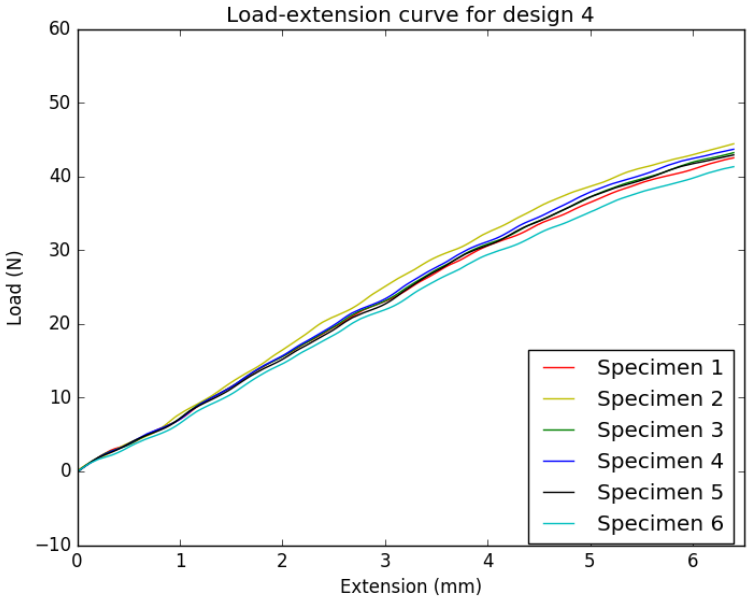

(b) Design 4

Figure C.6: Load-extension curves for T-glase designs 3 & 4

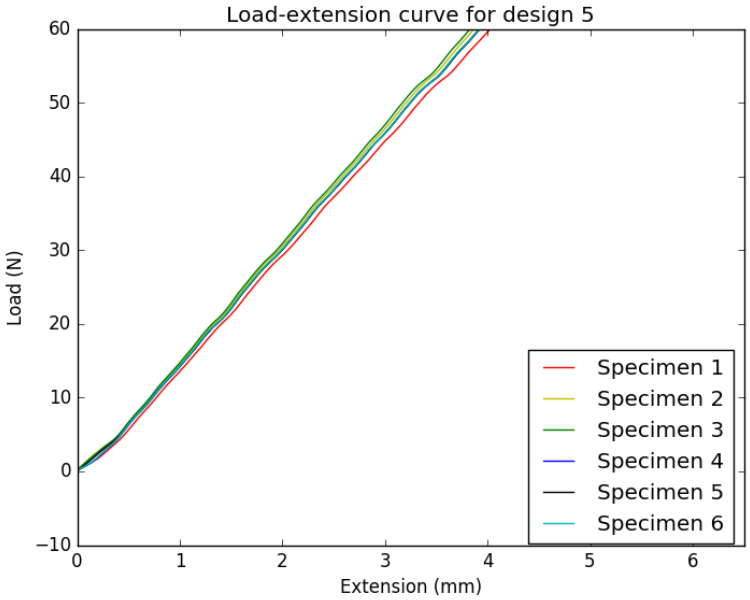

(a) Design 3

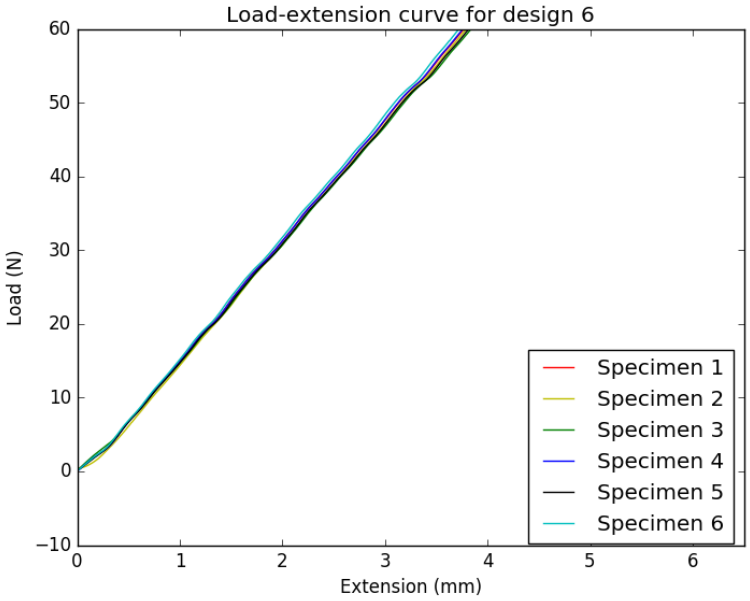

(b) Design 4

Figure C.7: Load-extension curves for T-glase designs 5 & 6

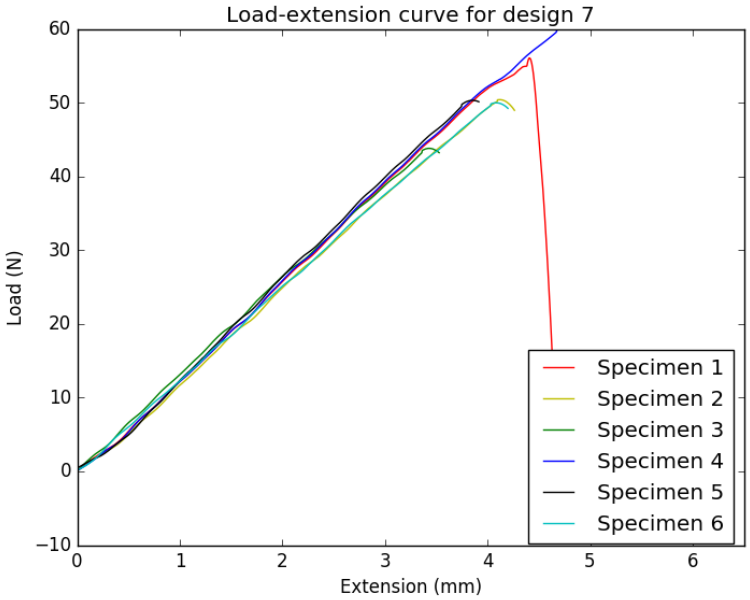

(a) Design 3

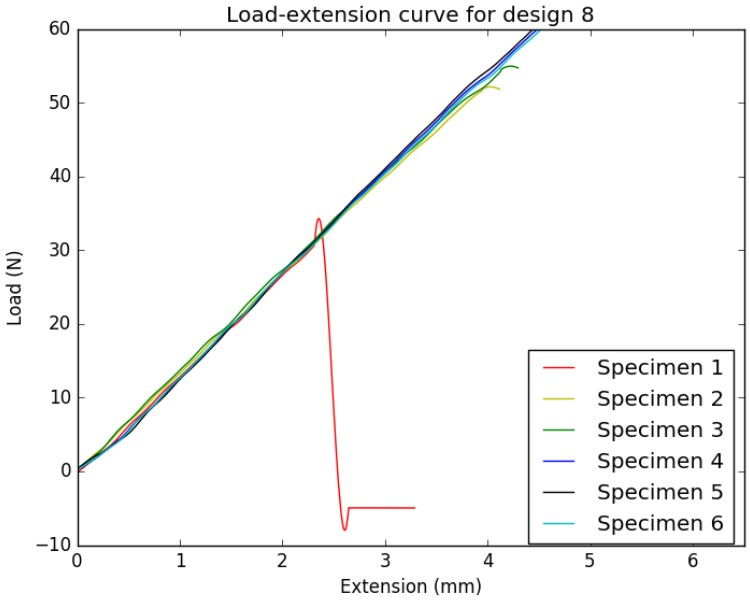

(b) Design 4

Figure C.8: Load-extension curves for T-glase designs 7 & 8

Appendix D

Model section measurements

	Location	Section											Average	Nominal	Error	STD	STD%avg	STD%nom
		1	2	3	4	5	6	7	8	9	10	11						
Thickness (mm)	Main deck P	2.68	2.76	2.84	2.79	2.67	2.84	2.83	2.70	2.76	2.66	2.69	2.75	2.50	9.891%	0.067297	2.450%	2.692%
	Main deck SB	2.95	2.99	3.02	3.02	2.91	3.18	2.99	2.82	2.93	2.78	2.83	2.95	2.50	17.891%	0.10788	3.660%	4.315%
	Side wall P	2.87	2.86	2.92	2.78	2.82	3.00	2.85	2.80	2.89	2.79	2.91	2.86	2.50	14.509%	0.062681	2.190%	2.507%
	Side wall SB	2.86	2.90	3.00	2.80	2.87	3.13	2.84	2.79	2.85	2.74	2.75	2.87	2.50	14.655%	0.108399	3.782%	4.336%
	Bottom	2.82	2.85	2.92	2.92	2.99	3.26	2.86	2.79	2.93	2.87	2.81	2.91	2.50	16.436%	0.124203	4.267%	4.968%
	Inner side P	2.92	2.89	2.99	2.99	2.79	2.85	2.94	2.84	2.90	2.88	2.85	2.89	2.50	15.782%	0.059599	2.059%	2.384%
	Inner side SB	3.01	3.09	3.14	2.99	3.05	3.06	3.11	3.07	3.14	3.01	3.13	3.07	2.50	22.909%	0.051714	1.683%	2.069%
	Inner bottom	2.92	2.99	3.05	2.94	2.81	2.80	2.84	2.82	2.92	2.74	2.80	2.88	2.50	15.018%	0.09049	3.147%	3.620%
	Stiffener P	2.99	2.92	2.99	2.95	2.86	2.89	2.93	2.88	2.92	2.88	2.87	2.92	2.50	16.655%	0.043542	1.493%	1.742%
	Stiffener DB	3.01	3.06	3.19	3.08	3.00	3.07	3.08	3.04	3.06	3.04	3.00	3.06	2.50	22.291%	0.050649	1.657%	2.026%
	Stiffener SB	2.89	3.00	3.02	2.97	2.78	2.93	2.88	2.81	2.97	2.82	2.86	2.90	2.50	16.109%	0.07747	2.669%	3.099%
Length (mm)	Length P	115.97	142.19	142.15	142.19	142.21	142.07	141.91	142.02	142.07	141.60	142.14	142.06	142.00	0.039%	0.175057	0.123%	0.123%
	Length SB	116.09	142.12	142.12	142.10	142.19	142.15	142.02	142.02	141.95	141.87	142.17	142.07	142.00	0.050%	0.098026	0.069%	0.069%
	Depth P	130.39	130.51	130.46	130.44	130.48	130.82	130.34	130.27	130.35	130.42	130.52	130.45	130.00	0.350%	0.136606	0.105%	0.105%
	Depth SB	130.56	130.53	130.61	130.49	130.48	130.67	130.44	130.44	130.48	130.62	130.47	130.53	130.00	0.405%	0.074623	0.057%	0.057%
	Depth DB	28.32	28.34	28.34	28.31	28.25	28.59	28.18	28.21	28.19	28.32	28.26	28.30	28.00	1.075%	0.107404	0.380%	0.384%
	Mid DB to P	111.86	112.00	111.95	111.93	111.84	112.02	111.92	111.83	112.06	112.03	112.00	111.95	111.25	0.628%	0.07645	0.068%	0.069%
	Mid DB to SB	111.80	111.86	111.87	111.91	111.74	112.03	111.80	111.79	111.79	111.82	111.73	111.83	111.25	0.522%	0.080955	0.072%	0.073%
	Breadth	220.65	220.80	220.63	220.76	220.58	220.98	220.64	220.58	220.79	220.81	220.73	220.72	220.00	0.329%	0.115687	0.052%	0.053%

Figure D.1: Measurements of the main dimensions and thicknesses of each section of the model

Appendix E

Specimen and vessel mesh convergence study

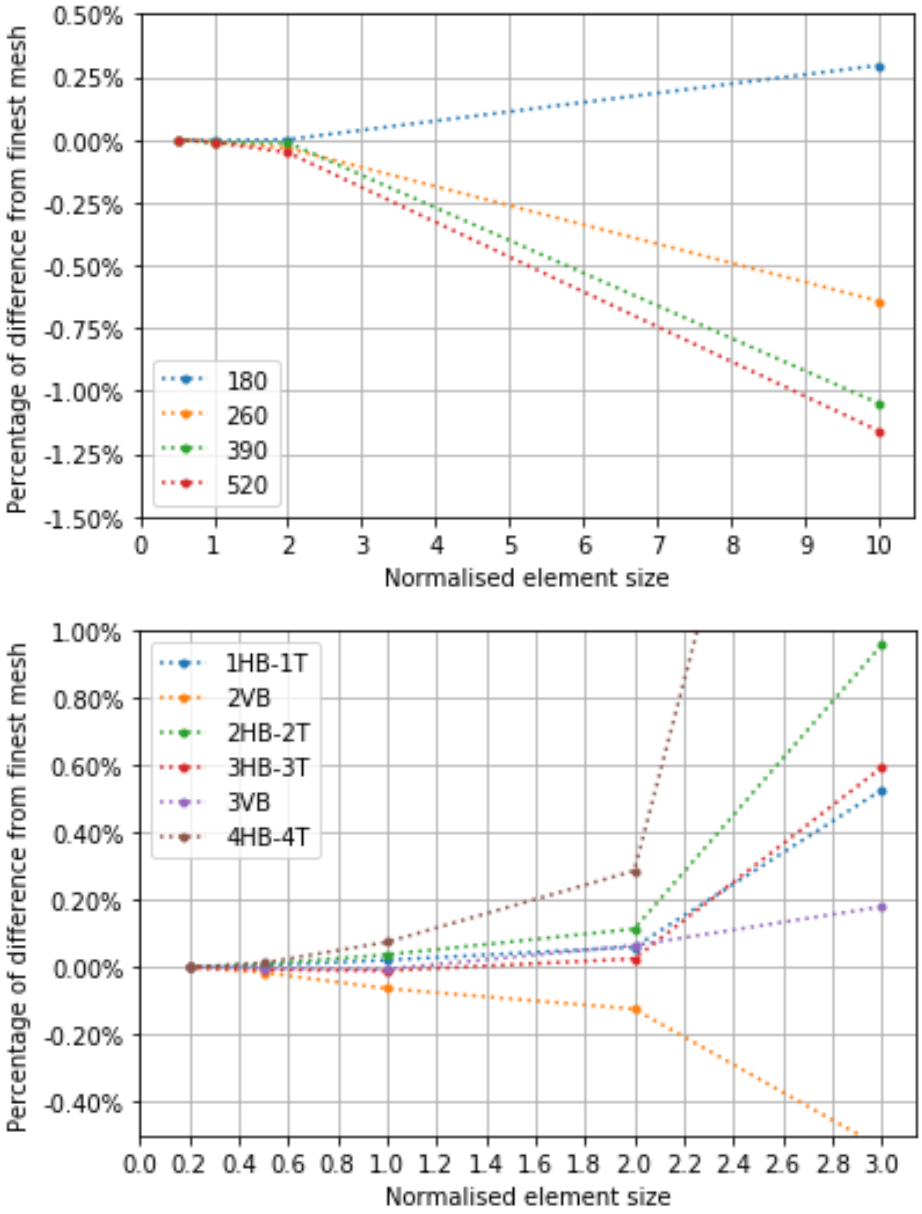

Figure E.1: Mesh convergence study for the specimens (top) and the vessel (bottom). The normalised element size corresponds to the element size over the element size actually used in the simulations. The percentage of difference is calculated by comparing to the results of the finest mesh. Specimen results correspond to the 2-node bending natural frequency for various specimen lengths. Vessel results correspond to the unballasted vessel.

Appendix F

Unballasted vessel frequency response functions

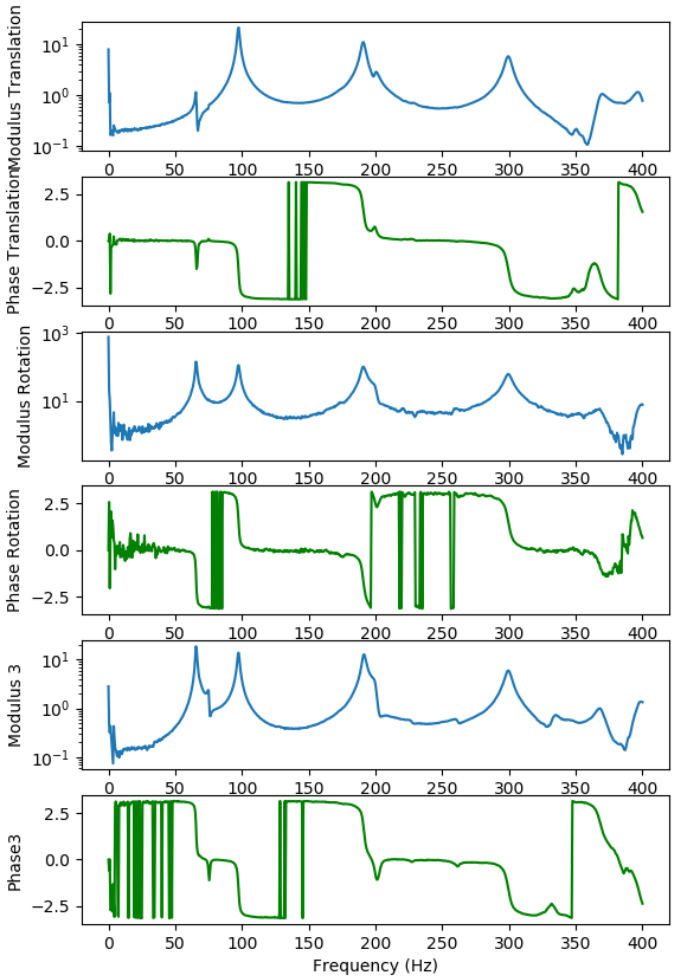

Figure F.1: The frequency response function of the vessel when excited at station 1 in the horizontal direction.

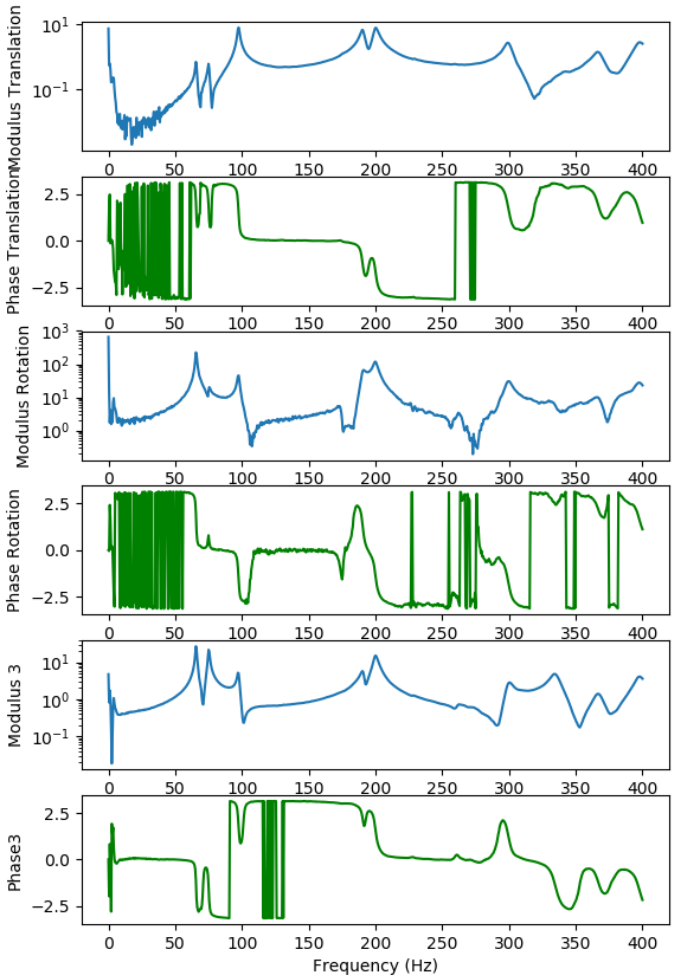

Figure F.2: The frequency response function of the vessel when excited at station 1 in the vertical direction.

Appendix G

Relevant publications

EXPERIMENTAL DYNAMIC PROPERTIES OF ABS CELLULAR BEAMS PRODUCED USING ADDITIVE MANUFACTURING

Apostolos Grammatikopoulos[1] , Joseph Banks[2] and Pandeli Temarel[3]

Fluid-Structure Interactions Group, University of Southampton
[1]Email: ag3e15@soton.ac.uk
[2]Email: J.Banks@soton.ac.uk
[3]Email: P.Temarel@soton.ac.uk

Keywords: additive manufacturing, cellular, flexural modulus, structural vibration, thin-walled girders

Abstract
Additive manufacturing is used increasingly for functional products and, consequently, the mechanical characterisation of the produced component has become a highly investigated topic. However, experimental routines consist mainly of tensile tests with standardised specimens and investigations focus on how process and design parameters, for example infill pattern, infill ratio, layering direction, affect the tensile modulus, ultimate elongation and strength.

In many cases, 3D printed components are subjected to static and/or dynamic bending operational loads and the flexural modulus should be identified. In polymers this can be significantly different, with an expected value between tensile and compressive moduli. Additionally, if the loading on the structure is dynamic (steady state or transient), dynamic (or vibratory) properties of the 3D printed structure become important. The present investigation focuses on methods for the experimental measurement of the flexural modulus under quasi-static and, more importantly, dynamic excitation. A range of structural approximations/numerical models are compared to identify the most suitable in providing the flexural modulus in a consistent manner.

1. Introduction

With additive manufacturing moving from being used solely for prototyping to production of experimental components and even end products, prediction of the mechanical properties becomes increasingly important. ABS and PLA are currently the most popular materials used for 3D printing, amongst others, due to ease of application and the industry's accumulated experience with such materials. Consequently, experimental research regarding 3D printed components revolves mainly around these two materials and, in some cases, the rapidly-emerging polycarbonates, the latter for enhanced mechanical properties and components subjected to higher loads.

Experimental investigations on the effect of design parameters on the mechanical properties of finished components have been quite extensive. Ahn et al [1] investigated the different infill patterns for ABS prints, as well as the relevant angles, and found significant effects on the tensile and compressive strengths of specimens. Rodríguez et al. [2] demonstrated the influence of the print meso-structure and infill ratio on the stress-strain response and particularly on the tensile modulus and strength. The results were compared to measurements from tensile testing of ABS filament and indicated reduction of mechanical properties through the filament deposition method. The measurements were then used to identify the printing parameters which optimize the mechanical behaviour of ABS components.

Es-Said et al. suggested that components produced with filament deposition resemble laminated materials in their orthotropic behaviour [3]. They also investigated how different layering directions affect yield strength and ultimate strength in tension, ultimate strength in bending and absorbed energy in impact. Although bending tests were performed in this case, no data was presented regarding the flexural modulus of the ABS specimens. Lee et al. [4], on the other hand, carried out experiments on the compressive strength of printed ABS components and demonstrated the anisotropic behaviour by applying loading in various directions. In this rare example of an investigation on the compressive properties of printed components, details regarding the compressive modulus were not provided.

As may be observed from the above, the focus of investigations is mainly set on failure modes and operational limits of the produced components. This can be explained by the fact that some applications only require the component to be sufficiently stiff and reliable and the precise value of the Young's modulus is not necessarily required. However, in the cases where a prediction of operational deflections and/or strains is critical, information in the literature only pertains to the tensile modulus. In the case of polymers, this can be quite different from the compressive modulus; in turn, the flexural modulus has a value between these two. It is recommended that, depending on the main loading direction (tensile/compressive/bending) on the structure under design, the relevant tests (tensile/compressive/flexural) are performed to calculate the appropriate modulus [5]. Moreover, due to the viscoelastic nature of polymers, the dynamic modulus in flexure can be different from the one observed under static or quasi-static loading.

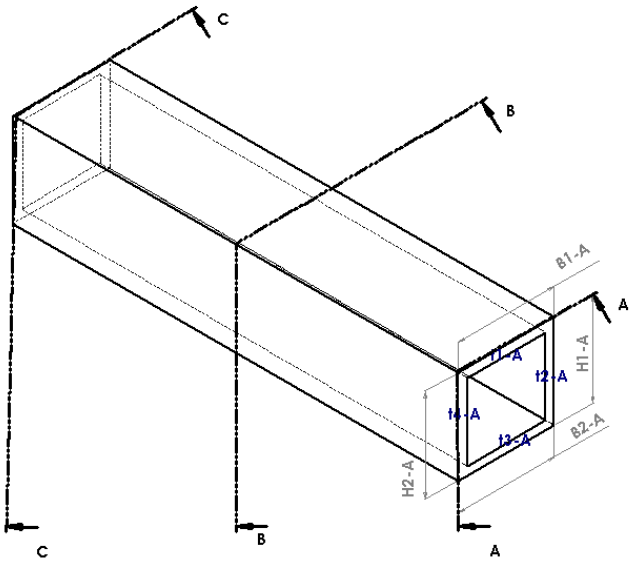

Figure 1: Depiction of the measurement points for each specimen segment. A, B and C denote the 3 sections where measurements were obtained. H, B and t represent measurements of height, breadth and thickness, respectively. No thickness measurements were obtained at the midpoint.

Our research is aimed at generating detailed elastic scaled models of ships, which requires prediction of the flexural modulus, to engineering accuracy standards, as it affects the natural frequency of the scaled ship model. The present investigation focuses on the vibratory responses of 3D printed hollow rectangular beams (see Figure 1) and the dynamic flexural modulus that is derived from them. Such components are part of the cellular arrangement of a container ship. To this end, a range of hollow rectangular uniform beams with various length/height ratios are tested using the modal testing (also known as impulse/impact excitation method [6]) and 3-point bending methods. Additional tests are carried out to examine the influence of transverse bulkheads in the middle and at the ends of the beam. The results are correlated using both Euler-Bernoulli and Timoshenko beam approximations and their

suitability is assessed by comparing against a shell structural model.

2. Methodology

2.1. Specimen production

Table 1: Specimen cross section details, with mean and standard deviation calculated for the entire population of specimens, rather than each specimen type separately (see Table 2).

Dimension	Symbol	Mean	SD
Breadth (m)	B	0.0280	9.88E-05
Height (m)	H	0.0273	7.62E-05
Thickness (m)	t	2.67E-03	6.31E-05
Cross-sectional Area (m^2)	A	2.68E-04	1.40E-06
2^{nd} Moment of Area (m^4)	I_{yy}	2.76E-08	1.52E-10
Mass/ Unit Length (kg/m)	μ	0.2622	0.0067

Table 2: Specimen type details, measured 2-node bending natural frequency (dynamic tests) and measured difference in load values corresponding to strains of 0.0025 and 0.0005 (3-point bending tests).

Specimen Type	L (m)		Number of Segments	Number of Specimens	Test Points	f_{2-node} (Hz)		$\Delta F_{\varepsilon=0.0005,0.0025}$ (N)	
	Mean	SD				Mean	SD	Mean	SD
A*	0.180		1	5	3	1372.47	22.43	124.82	6.75
B	0.180	1.21E-04	2	5	3	1381.53	9.52	93.51	17.67
C	0.256	1.00E-04	2	6	5	737.17	7.72	99.90	21.71
D†	0.260	9.77E-05	2	5	5	678.60	3.33	109.65	5.58
E	0.390	4.41E-04	3	5	8	340.46	2.93		
F	0.520	1.45E-04	4	3	11	194.33	0.90		

* Only nominal length available
† Including transverse bulkheads

For the purposes of this investigation, specimens of a constant, hollow rectangular cross section were manufactured using 3D printing. ABS was printed with an infill ratio of 99%, resulting in almost entirely solid structure. The layering direction was the same for all specimens and parallel to their longitudinal axis and the layer height used was 0.25 mm. Specimens of four different lengths were manufactured, namely 180 mm, 260 mm, 390 mm and 520 mm, in order to investigate the influence of beam-like behaviour. Details regarding the cross section may be found in Table 1.

In the case of 180 mm specimens, both a continuous version (A) and a version of two equal segments joined in the middle (B) were produced. The remaining specimens were all produced in segments of 130 mm. In all cases, the segments were joined together using a solution of the printing material (ABS) in acetone. The segments were constrained together using sash clamps while the acetone was evaporating to leave just ABS in the area of connection. An alternative version of the 260 mm specimens was produced, which included bulkheads at the ends and the middle of the specimen. A summary of all specimen types may be found in Table 2.

Extensive measurements were taken on each specimen segment prior to joining. Four thickness measurements, two breadth measurements and two height measurements were taken on each end of the segment. Two additional breadth and height measurements were taken at the midpoint of each segment. The measurement points are depicted in Figure 1. The measurements were used to calculate the cross-sectional

area and second moment of area at different points of each specimen (Table 1).

2.2. Experiments

The specimens were subjected to modal testing with both ends treated as free supports. They were tethered using flexible bands at the nodal locations of the 2-node bending mode, to minimise the influence of support on the aforementioned mode [7], which was the main focus of the investigation. The roving hammer setup used a PCB-086E80 instrumented hammer (sensitivity: ($\pm$20%) 22.5 mV/N) for the excitation measurement and a PCB-352C22 accelerometer (sensitivity: ($\pm$15%) 1.014 mV/m/s^2, frequency range: ($\pm$5%) 1.0 to 10000 Hz), located at one of the free ends of the specimen, for the response measurement. Both measurements were obtained using a DataPhysics Quattro Dynamic Signal Analyzer and SignalCalc software and the latter was also used for the calculation of the relevant frequency response functions.

5 specimens were tested for most specimen types (with two exceptions) and the number of measurement points increased with the length of the specimen. Details about numbers of specimens and measurement points,which were approximately evenly distributed along the length, may be found in Table 2. For each measurement point, the test was repeated thrice, the frequency response function was calculated for each repetition and an average was produced. The measured frequency range was between 0 and 2000 Hz (at a 0.5 Hz step), thus including the 2-node bending natural frequency for all lengths (see Table 2), and higher-order natural frequencies for the longer specimens.

The shorter specimen types (A, B, C, D) were also subjected to 3-point bending tests. A servo-mechanical INSTRON testing machine was used for this purpose. Specimen types E and F were not subjected to this type of testing due to maximum length restrictions. The specimens were supported by two circular rollers at 10% of the length from either end, emulating pinned-pinned boundary conditions. Both rollers had a diameter of 10 mm. A third roller of the same size applied a displacement at the midpoint of the specimen, descending at a speed of 2 mm/min. All the above parameters were based on the standard for the determination of flexural properties of plastics [8].

Both the experimental procedure and the post-processing method described above follow the relevant ASTM standard [6], with an increased number of measurement points. For static tests, this method was substituted by the procedure described in the relevant ISO Standard [8]. In this procedure, an Euler-Bernoulli beam approximation is assumed to calculate the modulus using the measurement points corresponding to strains of 0.0005 and 0.0025. In both types of tests, minor adjustments were made in the post-processing of results to account for differences in the specimen geometry compared to what is prescribed, as seen in the above equations.

2.3. Mathematical modelling

The specimen structure was then modelled using a number of different methods to investigate their validity for each specimen type. All values, including geometrical aspects, mass and experimental measurements (natural frequency, quasi-static extension & load) were averaged per specimen type for the purposes of these calculations.

As all the specimens, with the exception of specimen type D which included bulkheads, featured a uniform cross section and uniform mass distribution, the dynamic flexural modulus may be calculated with an Euler beam approximation, namely:

$$\omega_{2-node} = \frac{4.73^2}{L^2}\sqrt{\frac{EI}{\mu}} \tag{1}$$

where L is the specimen length, E the flexural modulus, I the 2^2 moment of area and μ the mass per unit length.

The second modelling method used a Timoshenko beam approach (element BEAM188 in ANSYS), whereas the third method employed a fully 3D FEA approach with shell elements including both membrane and bending loads (element SHELL181 in ANSYS). In all cases, an iterative process was followed to identify the flexural modulus E that resulted in the natural frequencies measured during the experiments. In all cases, lines were meshed with a maximum element length of 0.0009 m; that is to say, an element size of 0.0009 was used along all axes. The eigenvalue problem of the specimen with free-free boundary conditions was solved to compare to dynamic tests. The specimens were also modelled with roller support and a single applied deflection and the results were compared to the 3-point bending tests.

The range of different specimen types, combined with the aforementioned modelling techniques, was selected to allow a thorough understanding of their dynamic behaviour through the following process:

- establish (by comparing to shell modelling predictions) whether the vibrating specimens may be modelled using a beam approximation to derive the dynamic flexural modulus of the material from the 2-node bending natural frequency
- assess the suitability of the Euler beam method (as opposed to Timoshenko beam theory) depending on the length of the specimens and the importance of shear effects when calculating the aforementioned frequency
- investigate whether the inclusion of transverse bulkheads alters, in any way, the accuracy of these approximations.
- compare the produced values for the flexural modulus, from measured responses in quasi-static and dynamic conditions.

3. Results

3.1. Modal tests

The average 2-node vertical bending natural frequencies for the various specimen types are given in Table 2. Differences in natural frequencies between specimen types A and B (which have the same length and cross section) may be attributed to a larger thickness average on type A specimen, as well as the joining process for specimen type B. The more significant difference between specimen types C and D is due to the presence of transverse bulkheads in the latter which, although they don't affect the longitudinal stiffness, act as point masses at the local extrema of the 2-node bending mode shape (free ends and midpoint).

A summary of the dynamic flexural modulus estimations are shown in Figure 2. It may be observed that the shell element model provides us with with a consistent estimation of the dynamic flexural modulus (2.155 MPa with a standard deviation of 0.8%) over all specimen types. As this model includes both shear deformation effects in bending and section warping, it is considered the most general model and is used a baseline.

Estimations using the Timoshenko beam model are fairly close to the shell estimations (maximum difference of 3.5%) for most specimens, with the difference between the two increasing as specimens become shorter. This difference is attributed to warping of the cross section. Warping becomes less apparent in

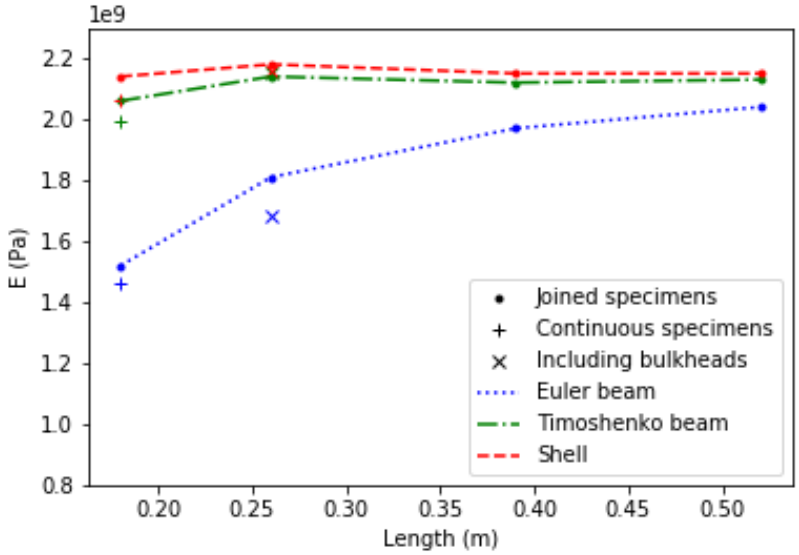

Figure 2: Dynamic flexural modulus of the specimens, derived from the 2-node bending natural frequency using three different structural models, as a function of specimen length. Lines (dot markers) depict specimens with no bulkheads, produced by joining a number of segments (see Table 2). + markers depict specimens without any joining, whereas x markers depict specimens including bulkheads.

longer specimens and from type C onwards the dynamic flexural modulus may be calculated using the Timoshenko beam approximation with difference from shell modelling of only 0.9%.

Estimations based on the Euler-Bernoulli beam approximation diverge much more significantly for shorter specimens. For the more slender specimens with a length of 520 mm the difference in calculated modulus from the shell element estimation is of the order of 5%. However, the difference rapidly increases with decreasing length, reaching 40% for the 180 mm specimens. It is evident that, for this scale of specimens, the 2-node bending natural frequency is significantly affected by shear deformation effects.Use of the Euler-Bernoulli beam approximation would only be recommended for the 520 mm specimens. This corresponds to a length/height ratio of 19, which is close to the ratio of 20 recommended by the standards (for beams with a rectangular rather than box-shaped cross section) [6, 8] to use the Euler beam approximation.

The continuous specimens (i.e. specimen type A) showed similar trends to the joined beams regarding the accuracy of the various approximations. When compared to specimen type B, comprising two segments, a slight increase in stiffness is observed caused by joining. The presence of bulkheads in specimen type D have two distinct effects. Firstly, the difference of the Euler beam results when compared to specimen type C signifies the importance of the mass distribution when calculating the natural frequency of these structures. Secondly, being the only specimen type where the Timoshenko beam and shell models coincide, it is emphasised that bulkheads prevent any deflection of the cross section and result in a structure that can be described just as well using a beam approximation.

3.2. 3-point bending tests

Results from the 3-point bending tests are shown in Figure 3. It can be observed that the trends for these quasi-static tests resembles the one previously discussed for the dynamic tests. The shell model suggests more consistent results for all specimen types tested, with the Timoshenko beam approximation slightly closer to these values for longer specimens and the Euler beam approximation having significantly larger

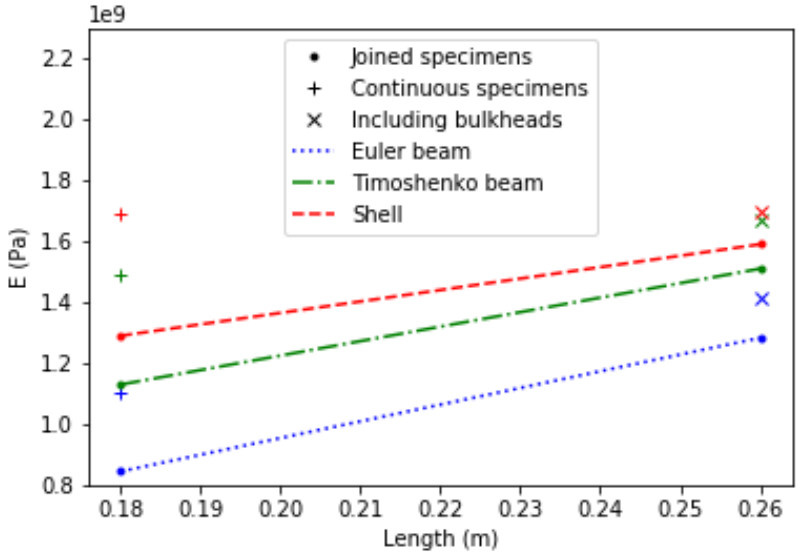

Figure 3: Quasi-static flexural modulus of the specimens, derived from the load-displacement curves using three different structural models, as a function of specimen length. Lines (dot markers) depict specimens with no bulkheads, produced by joining a number of segments (see Table 2). + markers depict specimens without any joining, whereas x markers depict specimens including bulkheads.

differences. It is also demonstrated that the quasi-static flexural modulus is approximately 35% lower than its dynamic counterpart. It may be concluded that identification of the quasi-static modulus would not be sufficient for the modelling of 3D printed structures which are subjected to dynamic loads.

The presence of bulkheads was found once more to restrict warping of the cross section and result in a specimen behaving more in a beam-like manner. As can be seen in Figure 3 the Timoshenko beam and shell approximations produced almost identical results (x-shaped markers). On the other hand, continuous specimens were found to produce responses indicating higher stiffness than the joined ones, contrary to what was found in vibration tests. Differences between the measured static and dynamic elastic modulus may be partly attributed to the viscoelastic nature of ABS. Furthermore, the experimental uncertainties associated with quasi-static and dynamic tests can be quite different, as illustrated by the mean and standard deviation values in Table 2, due to both the way the measurements are obtained and the nature of the physical problem investigated (load-deflection relationship or structural eigenvalue problem).

4. Conclusions

The present investigation examined the vibratory responses of 3D printed specimens with a thin-walled rectangular cross section. The main focus was the relationship between the 2-node bending natural frequency and the flexural modulus. The effects of joining specimens from segments and the effects of the presence of transverse bulkheads were also investigated. The specimens were subjected to modal testing, suspended using flexible bands at the 2-node bending nodes to emulate a free-free boundary condition. A range of different mathematical approximations were used to describe the dynamic behaviour and a dynamic flexural modulus was calculated based on the average measured 2-node bending natural frequency for each specimen type.

The shell element formulation was found to give consistent results for all specimen types and was used as a baseline. The Timoshenko beam approximation resulted in a flexural modulus estimation which

was very close to that of the shell approximation. A subtle increase in the difference between the two was observed for the very short specimens and was attributed to warping of the cross section. The Euler-Bernoulli beam approximation was found to produce more significant differences for this type of geometry, resulting in a difference from the shell model of the order of 5% for long specimens but increasing rapidly to 40% for the shortest specimens. Continuous specimens indicated that joining causes relatively small difference in the dynamic stiffness, whereas the presence of bulkheads resulted in a more beam-like behaviour.

Quasi-static 3-point bending tests demonstrated similar trends, whereas the quasi-static flexural modulus was found to be approximately 35% lower than the dynamic flexural modulus when using a shell approximation. The effects of joining on quasi-static responses appear to contradict the behaviour observed during dynamic tests, which may be attributed to the difference in nature between the two tests, resulting in different types of uncertainty. As observations on the continuous specimens and the ones including bulkheads were only based on one type of specimen, they should serve more as indicators and further investigation on these effects would be recommended.

Overall, dynamic tests and use of a Timoshenko beam approximation is recommended for the prediction of the dynamic properties of structures produced using additive manufacturing and materials similar to ABS. An elastic ship model with a cellular cross section resembling that of a container ship has been subjected to dynamic tests and it was established that 3-point bending tests are not appropriate for the prediction of its vibratory properties [9]. The flexural modulus of this model, obtained from the dynamic tests, was found to agree well with the Timoshenko beam and shell predictions in Figure 2.

Acknowledgements

The present investigation was funded by the Lloyd's Register Foundation University Technology Center on Ship Design for Enhanced Environmental Performance.

References

[1] S.-H. Ahn, M. Montero, D. Odell, S. Roundy, and P. K. Wright, "Anisotropic material properties of fused deposition modeling ABS," *Rapid Prototyping Journal*, vol. 8, no. 4, pp. 248–257, 2002.

[2] J. F. Rodríguez, J. P. Thomas, and J. E. Renaud, "Mechanical behavior of acrylonitrile butadiene styrene (ABS) fused deposition materials modeling," *Rapid Prototyping Journal*, vol. 9, no. 4, pp. 219–230, 2003.

[3] O. S. Es-Said, J. Foyos, R. Noorani, M. Mendelson, R. Marloth, and B. A. Pregger, "Effect of Layer Orientation on Mechanical Properties of Rapid Prototyped Samples," *Materials and Manufacturing Processes*, vol. 15, no. 1, pp. 107–122, 2000.

[4] C. Lee, S. Kim, H. Kim, and S.-H. Ahn, "Measurement of anisotropic compressive strength of rapid prototyping parts," *Journal of Materials Processing Technology*, vol. 187-188, pp. 627–630, 2007.

[5] H. G. Harris and G. Sabnis, *Structural modelling and experimental techniques*. CRC Press, second ed., 1999.

[6] "ASTM E1876-15: Standard Test Method for Dynamic Young's Modulus, Shear Modulus, and Poisson's Ratio by Impulse Excitation of Vibration," 2015.

[7] T. G. Carne, D. T. Griffith, and M. E. Cassias, "Support Conditions for Free Boundary-Condition Modal Testing," *IMAC-XXV: A Conference & Exposition on Structural Dynamics*, no. January 2015, 2007.

[8] "ISO 178:2001: Plastics-Determination of flexural properties," 2003.

[9] A. Grammatikopoulos, P. Temarel, and J. Banks, "Experimental hydroelastic responses of an elastic container ship-inspired barge model produced using additive manufacturing," in *8th International Conference on Hydroelasticity in Marine Technology*, (Seoul, Korea), 2018.

Experimental hydroelastic responses of an elastic container ship-inspired barge model produced using additive manufacturing

Grammatikopoulos, A.[1] , Banks, J.[2] and Temarel, P.[3*]

Fluid-Structure Interactions Group, University of Southampton
[1]Email: ag3e15@soton.ac.uk
[2]Email: J.Banks@soton.ac.uk
[3]Email: P.Temarel@soton.ac.uk

ABSTRACT

Despite significant advancements in the field of computational hydroelasticity, manufacturing methods for corresponding physical models have not changed beyond the flexible backbone concept in the past 20 years. Few researchers have attempted to produce continuous models with an accurate internal structure, the so-called elastic models, in order to obtain more detailed measurements of the structural responses. These investigations faced the limitations of the then available manufacturing methods, which did not allow for any internal details of the structure, apart from bulkheads, to be included in the design without significant increase in difficulty and cost. The resulting structures, although continuous, comprised of an external shell and the effects of cross-sectional shape could not be investigated.
In this investigation, manufacturing difficulties of the past are overcome by use of additive manufacturing to create a barge model with a container ship-inspired cross section. The design and manufacturing processes are presented, followed by vibration tests and towing tank tests in regular head waves. The measured vertical bending moment responses in various stations were found to correlate well with 2D hydroelasticity and the strain distribution along the cross section of the vessel indicated beam-like behaviour. A detailed discussion of the challenges and sources of uncertainty is included, along with suggestions for future work.

Keywords: Elastic model; Additive manufacturing; Container ship; Barge; Vertical bending

1. INTRODUCTION

While hydroelastic analyses have come a long way in the past 20 years, design and production processes for the corresponding experimental models have not changed significantly from the flexible backbone concept. Computational methods to model the effects of hydroelasticity have gradually evolved from 2D (Bishop and Price, 1979) to fully 3-dimensional codes,

*Correspondence to ag3e15@soton.ac.uk

either using potential flow methods (Kim et al., 2015) or computational fluid dynamics (Lakshmynarayanana et al., 2015). For the former, the hydrodynamic codes are coupled with finite element models, which can also be 3-dimensional (Hirdaris et al., 2003), to produce a coupled hydroelastic formulation.

On the other hand, it is common practice for models to be produced with the hydrodynamic and structural aspects segregated. The hull form is produced by slicing a conventional model into rigid segments. The appropriate stiffness is then introduced by means of either a flexible backbone (Peng et al., 2014) or a series of flexible joints (Lavroff et al., 2007). The design process is based on beam approximation and scaling of at least the two-node bending natural frequency. Bending stiffness distribution is, more often than not, ignored for manufacturing simplicity; few exceptions include the work by Dessi and Mariani (2008) who manufactured a non-uniform backbone depicting the bending stiffness distribution of a fast ferry. Use of flexible joints allows for easy tuning of the stiffness and its distribution (Wu et al., 2003). However, the structural properties are not modelled for a continuous structure, which can be considered a relative advantage of the backbone models. Even in the case of the latter, the cross sectional shape and shear area of the actual ship structure are ignored and only the 2nd moment of area is modelled. When investigations focus on the antisymmetric hydroelastic responses of the vessel, coupling between horizontal bending and twisting is usually provided by use of a U-shaped backbone (Kim et al., 2014) or a standard box-shaped one with deck openings cut into it (Zhu et al., 2011).

A number of investigations used continuous models with elastic material, to produce a more detailed structure, the so-called elastic models, in order to counteract the aforementioned issues as well as seek a more detailed structural response. Both Watanabe et al. (1989) and Chen et al. (2001) manufactured elastic models of the S175 container ship. The vessel was first introduced in the 15th and 16th International Towing Tank Conferences (ITTC) as a joint experimental and computational project involving several institutions for a comparative study of hydrodynamic and structural loads. While deflections were measured directly on the structure of these continuous models, their cross section did not resemble that of the full-scale vessel (Wu et al., 2003), with ensuing issues related to shear deflection, torsion of cellular structures etc. However, manufacturing limitations would otherwise render production almost impossibly complicated. Consequently, researchers were discouraged from using elastic models more extensively.

In this paper, additive manufacturing is proposed as a means to overcome the production difficulties faced in the past. Current technology allows for complex cross sections to be produced, with the end result closer to a real ship. A rectangular barge with a constant, container ship-inspired, cross section was produced using ABS, its main particulars approximately corresponding to a scaled-down version of the S175. The simple external geometry was selected to focus on structural issues. The barge was manufactured in segments, joined using solvents. Deep frames, transverse bulkheads and 16 strain gauges were installed throughout the vessel. Tests in regular waves are compared to 2D hydroelasticity predictions for verification. Hammer tests provide further understanding of the dynamic behaviour. Limitations of the method, mainly relating to material and manufacturing constraints and uncertainties are discussed together with possible solutions.

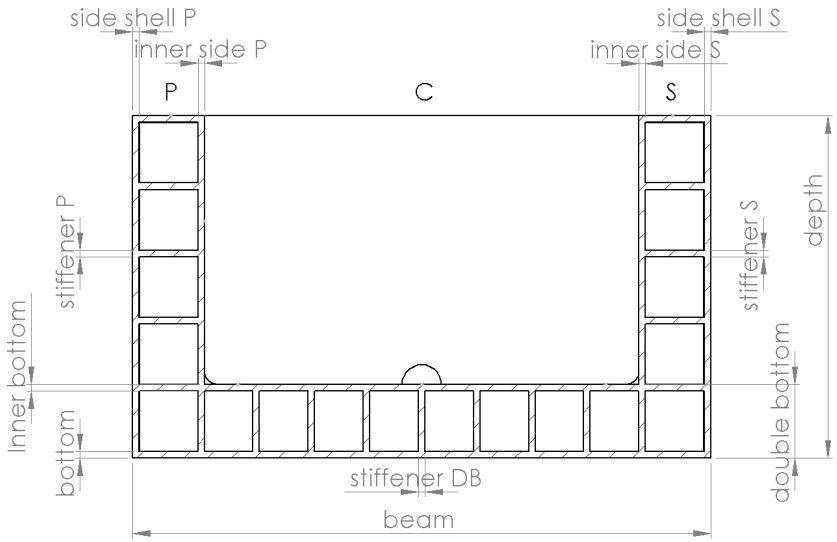

Figure 1: Cross section the uniform barge illustrating measurements taken to evaluate manufacturing uncertainties.

2. METHODOLOGY

2.1. Model design, production and instrumentation

The model produced for the purposes of this investigation was based on the S175 container ship. The scales previously used by Wu et al. (2003) and Watanabe et al. (1989) would result in a model too large for its cross section to fit in a conventional 3D printer. It was considered essential to avoid joining within the cross section as this would introduce additional uncertainties. As a result, the model was scaled down further to overcome this obstacle, with principal dimensions scaled uniformly. The model was designed with a uniform cross section (see Figure 1), for manufacturing simplicity purposes but also to allow for an easy first estimation of the EI needed to achieve the desired 2-node bending natural frequency.

It was decided to scale the displacement of the vessel rather than the draft, as the former would be more relevant to the dynamic properties and natural frequency. Consequently, the draft was smaller than if directly scaled, as the new model was barge-shaped. It should be emphasised, however, that the aim of this investigation was not to produce a scaled-down version of the S175 but rather a vessel with similar characteristics, allowing for qualitative comparison. A summary of the particulars of the vessel is shown in Table 1.

The walls of the model, shown in Figure 1, were designed with a thickness of 2.5 mm but were ultimately thicker (average thickness of 2.91 mm with a standard deviation of 0.12 mm) due to the thickness being close to the printer's limits of manufacturing accuracy. The 2nd moment of area of the cross section as per design would be equal to 5.2E-06 m^4. However, when calculated based on thickness measurements throughout the vessel, the average 2nd moment of area was found to be equal to 6.1E-06 m^4. The bending stiffness was predicted by combining the latter with with flexural modulus values obtained from 3-point bending tests of 3D-printed ABS coupons (average of 1124.69 MPa, with a standard deviation of 64.70 MPa). Using this bending stiffness and the non-uniform mass distribution in a non-uniform beam model (effective shear area equal to 1/3 of the cross-sectional area), the expected in vacuo 2-node bending natural frequency was found to be equal to 40 Hz. It was thus known, even before production had started, that the model would be stiffer than a scaled-down version of the S175, the natural

Table 1: Principal particulars of the cellular barge. The dry and wet 2-node bending natural frequencies are as measured from vibratory (hammer) tests, on the model and the EI derived from the measured dry natural frequency.

Dimension	Symbol	Value
Length between perpendiculars (m)	L	1.520
Beam (m)	B	0.220
Depth (m)	D	0.130
Draft (m)	T	0.047
Displacement (kg)	Δ	15.88
Block Coefficient	C_B	1.00
Bending stiffness (Nm^2)	EI	12078
Natural frequency in vacuo (Hz)	$f_{2\text{-node, vacuo}}$	53.0
Natural frequency in water (Hz)	$f_{2\text{-node, water}}$	31.0

frequency of which would have been 19 Hz in vacuo. As shown in Table 1, the measured 2-node bending natural frequency of the vessel in vacuo was found to be 53 Hz, for reasons that will be discussed in Section 3.

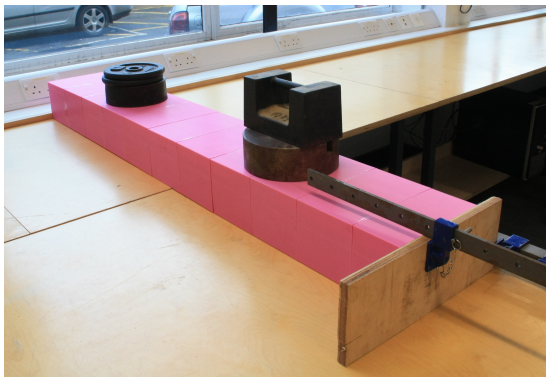

(a) Section joining

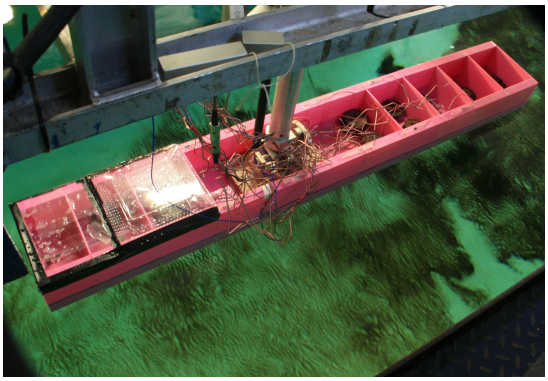

(b) Model in towing tank

Figure 2: Joining of the sections using ABS solution as adhesive and sash clamps as a constraint (a) and fully instrumented cellular barge model in the towing tank (b).

The model was made up of 11 sections, 10 sections of 140 mm length and the foremost section of 120 mm length to achieve the scaled length of the S175. All sections featured a deep frame at one end, namely the aft end. The sections were joined using a solution of the printing material (ABS) in acetone. The sections were constrained together using sash clamps while the acetone was evaporating to leave just ABS in the area of connection (Figure 2a). The vessel was then sanded using a power sander and coated with clear acrylic paint to improve resistance to water absorption. Bulkheads (4 mm thickn) were fitted on all deep frame locations, apart for the ones around the area of the tow post. The sections and bulkheads were produced using an UP Box printer and ABS filament, at a layer height of 0.25 mm.

16 strain gauges were installed, post 3D printing, in various locations of the hull: 5 on Main deck Port side, 3 on Main deck Starboard side, 5 on double bottom Centreline and, finally, an additional 3 strain gauges amidships, two near either corner of the double bottom and one on the inner side. Details of the locations of the strain gauges are shown in Table 2 and Figure 3. The strain gauges used were Micro-Measurements C2A-06-250LW-350 linear quarter-bridge strain gauges with a resistance of 350 Ω and a gauge factor of 2.150$\pm$0.5%.

Table 2: Positioning of strain gauges

#	Station	Transverse location	Vertical location
0	15.0	Port	Main Deck
1	12.5	Port	Main deck
2	10.0	Port	Main deck
3	7.5	Port	Main deck
4	5.0	Port	Main deck
5	15.0	Starboard	Main deck
6	10.0	Starboard	Main deck
7	7.5	Starboard	Main deck
8	15.0	Centreline	Inner bottom
9	12.5	Centreline	Inner bottom
10	10.0	Centreline	Inner bottom
11	7.5	Centreline	Inner bottom
12	5.0	Centreline	Inner bottom
13	10.0	Port	Inner side
14	10.0	Port	Inner bottom
15	10.0	Starboard	Inner bottom

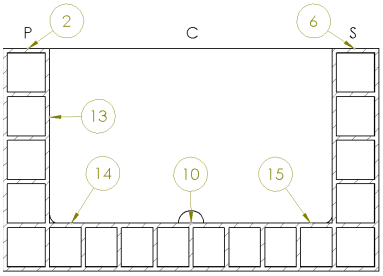

Figure 3: Locations of strain gauges amidships (i.e. Station 10.0). Main deck and Inner bottom locations same for other Stations (See also Table 2).

2.2. Static, modal & towing tank testing

The vessel was subjected to static tests to calibrate the sensors and identify the coefficients required to convert measured strains to bending moments. This calibration was carried out by incrementally increasing a weight applied on the unballasted simply supported hull in vacuo, resulting in the following conversion equation (Roark et al., 1976).

$$M = \frac{P(L-l_P)x}{L} - P\langle x - l_P\rangle \tag{1}$$

where M is the bending moment at location x for a simply supported beam of total length L when a vertical point load P is applied at location l_P. In this manner, the strains were converted to bending moments directly and without the need to assume an EI for the model.

The vessel was also subjected to modal analysis testing to identify its natural frequencies. The dynamic flexural modulus was derived from the 2-node bending natural frequency in vacuo. For the in vacuo modal analysis, the model was suspended using flexible bungee cords at the nodal locations of the 2-node bending mode, to minimise the influence of support on the aforementioned mode (Carne et al., 2007). The roving hammer setup used a PCB-086C03 instrumented hammer (sensitivity: ($\pm$15%) 2.25 mV/N) for the excitation measurement and a PCB-352C33 accelerometer (sensitivity: ($\pm$10%) 10.2 mV/m/s^2), located amidships (1cm off centreline to port), for the response measurement. Both measurements were obtained using a DataPhysics Quattro Dynamic Signal Analyzer and SignalCalc software and the latter was also used for the calculation of the relevant frequency response functions.

Measurements in both static (sensor calibration) and towing tank tests were obtained using a National Instruments cDAQ-9135 Data Logger and two National Instruments NI-9236 strain gauge modules. During towing tank tests, heave and pitch were measured using the tow post dynamometer and transferred from the amplifying unit to a NI-9205 Voltage module. All the above measurements were obtained using LabVIEW software. The wave probe measurements

during the tank tests were obtained through the Lasso software, developed by the Wolfson Unit.

The stationary model was tested in regular head waves in the Solent University towing tank (60m x 3.7m x 1.8m). The tow post was placed at Station 12, i.e. 10% forward of the midship section. A piece of plywood 250 mm long and 150 mm wide, connected to the model using captive nuts and threaded bars served as the base for the tow post (as shown in Figure 2b). The ballast distribution was designed to achieve an even-keel vessel.

Table 3: Wave/ship length ratios and frequencies for the tests in regular waves. A wave height of 0.05 m was used in all cases.

λ/L	ω (rad/s)	f (Hz)
0.6	8.22	1.31
0.8	7.12	1.13
0.9	6.71	1.07
1.0	6.37	1.01
1.1	6.07	0.97
1.2	5.81	0.93
1.3	5.59	0.89
2.0	4.50	0.72

The height of the regular waves was kept constant at 0.05 m, corresponding to H_{wave}/L_{BP} of 1/30. The wave frequencies were selected based on the λ/L used by Chen et al. (2001) and Wu et al. (2003) for the relevant wave height ratio (see Table 3). Each test condition was repeated three times.

A 2D hydroelasticity code based on linear strip theory and linear Timoshenko beam theory was used for comparison (Bishop and Price, 1979). The ship was divided into 50 sections along the length and the non-uniform mass was accounted for. A shear area coefficient of 1/3 was used, a selection based on experience. The flexural modulus used in this analysis was evaluated from the in vacuo 2-node bending natural frequency obtained from the vibratory tests.

3. RESULTS AND DISCUSSION OF UNCERTAINTIES

An iterative process, in conjunction with Timoshenko beam theory, is used, whereby the value of the flexural modulus E is varied until the in vacuo 2-node bending natural frequency matches the one from vibratory tests, namely 53 Hz. This iterative process results in E equal to 1.98 GPa. Thus it can be seen that the 2-node bending natural frequency of the vessel was under-predicted during the design stage (predicted natural frequency based on 3-point bending tests was 40 Hz). As the geometric characteristics of the vessel and the mass distribution were known with good accuracy, the discrepancy was attributed to a difference in the flexural modulus of the vessel compared with that obtained from 3-point bending tests of coupons.

Differences in the flexural modulus found by the 3-point bending tests could be attributed to two distinct causes. Firstly, the standardised coupon thickness used in the tests was higher than that of the vessel itself. As the thickness was reduced from 4 mm for the coupons to 2.5 mm for the vessel (wall thickness), the part of the wall that comprised the infill was reduced and, at the same time, printing close to the operational limits (minimum printable thickness) of the printer increased overlap of the infill. This resulted in an almost entirely solid cross section, which was bound to have a higher E than a specimen in which the modulus is calculated as an average over a cross section containing air gaps. A second cause of discrepancy was the fact that the flexural

modulus for polymers in dynamic conditions can be different than the static one. Indeed, an extensive study on the vibratory properties of 3D printed components (Grammatikopoulos et al., 2018) identified a dynamic flexural modulus which was significantly higher than the one predicted by 3-point bending. Specimens in this study comprised thin-walled rectangular cells of the same material and the predicted dynamic flexural modulus was 2.11 GPa.

Static tests (sensor calibration) revealed an apparent local increase of stiffness around the area of the tow post. The sensor primarily affected was strain gauge 9, which is located underneath the plywood piece, at Station 12.5. This locally increased stiffness was observed both in the static and dynamic responses of the vessel.

Responses in heave and pitch are shown in Figure 4, whereas bending moment responses are shown in Figure 5. The latter were based on strain measurements on the main deck of the vessel, Port side, on five Stations (5.0, 7.5, 10.0, 12.5 and 15.0). The strains were converted to bending moments using the bending moment/strain coefficients obtained from the static tests. The bending moments from the strain measurements and the 2D hydroelasticity predictions were then non-dimensionalised using the following equation:

$$C_M = \frac{M}{\rho g L^2 B A_{wave}} \tag{2}$$

where M is the bending moment, ρ is the water density, L and B are the length and beam of the vessel, respectively and A_{wave} is the wave amplitude.

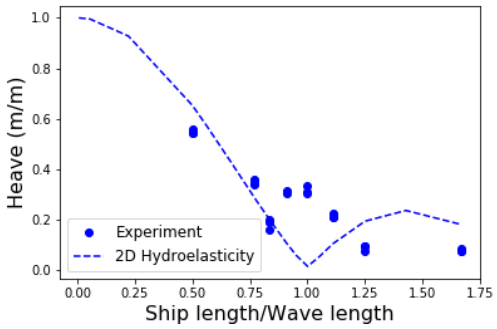

(a) Heave response

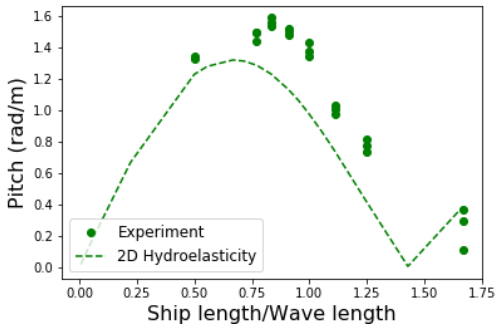

(b) Pitch response

Figure 4: Heave and pitch RAOs of the uniform barge.

Good agreement is observed between 2D Hydroelasticity and experimental measurements. Discrepancies between measured & predicted rigid body motion responses may be attributed to the use of Lewis sections for a vessel with rectangular cross sections and vertical bow and stern walls. Peak bending moment responses were measured, as would be expected, at the wave-ship matching region; bottom slamming was also observed in this region, particularly for λ/L equal to 1.0. Bending moments measurements were found to have slightly better agreement with 2D hydroelasticity for the aft half of the vessel (Stations 5.0, 7.5 and 10.0). Measurements were found to be less consistent between runs for shorter wave lengths and differences between measurements and 2D hydroelasticity predictions also increased for these cases. Green water was observed on the deck of the vessel for these higher frequencies, particularly during tests at λ/L=0.6. The bluff bow of the vessel would crash into these shorter waves and part of the wave would run over the fore deck. Overall, looking at the non-dimensionalised vertical bending moment coefficients, it was observed that the first harmonic component had similar values as

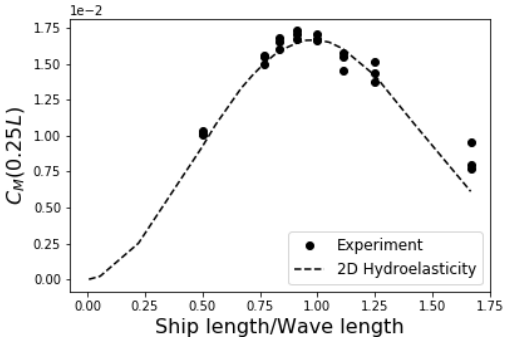

(a) Station 5

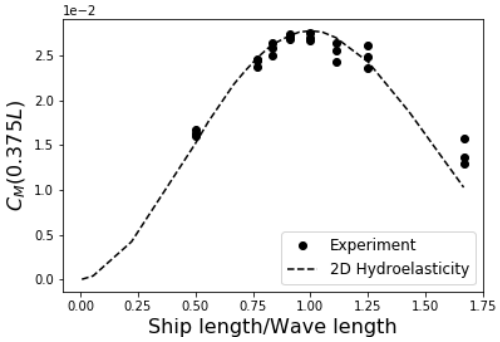

(b) Station 7.5

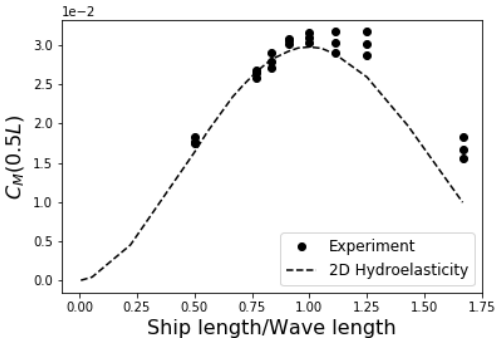

(c) Station 10

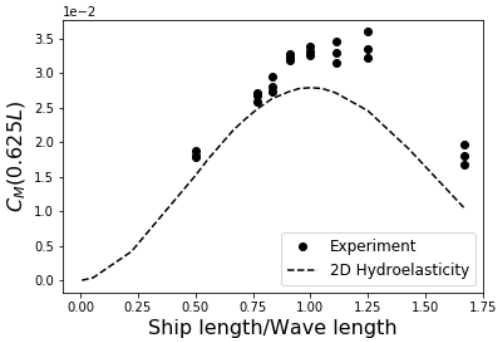

(d) Station 12.5

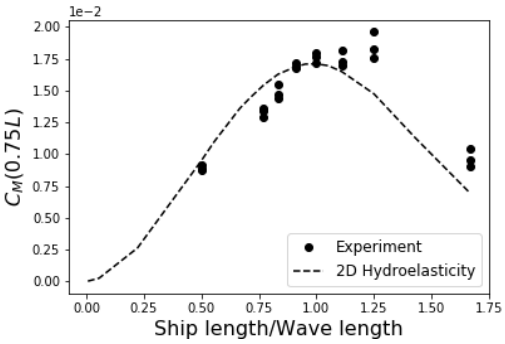

(e) Station 15.0

Figure 5: Bending moment measurements along the length of the vessel, based on strain measurements on Main deck Port side. 2D hydroelasticity results (based on linear strip theory and linear beam theory) are also presented for comparison. The loads were non-dimensionalised based on Eq. 2.

the ones measured by Chen et al. (2001) and the magnitude ratios between the first, second and third harmonics also featured comparable trends, as can be seen in Figure 6a.

As the 2-node bending natural frequency of the vessel was not even remotely close to the wave frequency range under investigation, no resonant behaviour due to linear springing was observed. Looking at a typical strain response in Figure 6a, a peak corresponding to the wet 2-node bending natural frequency is clearly visible at 31 Hz, caused by vessel slamming and consequent whipping responses, although these did not dominate the strain measurements. The amidships strain distribution from deck to bottom, shown in Figure 6b, is fairly linear, agreeing with beam theory.

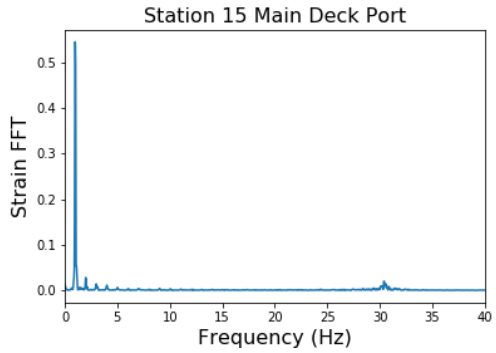

(a) Strain FFT

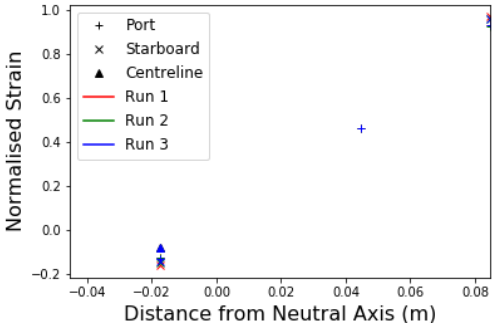

(b) Strain distribution

Figure 6: (a) Frequency content of the strain response in regular head waves at an excitation frequency of 1.01 Hz (λ/L=1.0) (b) Strain distribution throughout he midship section for the same excitation frequency.

4. CONCLUSION

In this investigation, an elastic ship model with a detailed cross section was designed, produced and tested for the first time. The vessel design was inspired by the S175 container ship particulars combined with the cross-sectional geometry of a realistic container ship. The vessel was subjected to static tests for calibration of the 16 strain gauges, vibration tests to determine its modal properties and, finally, towing tank tests in regular head waves at zero forward speed for a range of frequencies.

The qualitative, as well as quantitative, analysis of wave-induced motions and loads was verified using 2D hydroelasticity theory predictions. The bending moment RAO magnitudes are in line with those measured by Chen et al. (2001) for the S175 container ship. Furthermore, the frequency content of the strain (or bending moment) spectra show similar comparative magnitudes between first, second and third harmonic components as per Chen et al. (2001). These are all significant indicators for the validity of the model concept reported in this paper. It should also be noted that the uniform barge with cellular cross-sectional structure does behave as a Timoshenko beam.

The discrepancies observed for the rigid body motions can be attributed to the limitations of the applied method for bluff bodies. Unlike rigid and flexible backbone models, elastic models require careful consideration with reference to the attachment of the tow post. The recommendation is to aim for as reduced a footprint as possible. With the current tow post arrangement, it is important to model the local stiffening effects, which limits the applicability of beam-type idealisation and would require a 3D finite element model of the structure.

The additive manufacturing process introduced uncertainties in manufacturing tolerances which were particularly visible in the wall thickness of the model. Nevertheless, advances in the relevant hardware technology are rapidly improving these tolerances. The most important issue is the prediction of the dynamic flexural modulus of 3D printed polymers, such as ABS, which is essential in calculating the bending stiffness and corresponding 2-node natural frequency of the model. 3-point bending coupon tests of 3D printed polymer coupons, provide underestimated predictions for the dynamic flexural modulus of the structure in question. Further work on this subject indicated that a method involving vibration testing of specimens with a thin-walled cellular beam geometry provides an accurate prediction of the flexural modulus (Grammatikopoulos et al., 2018). Furthermore, as was previously discussed, the flexural

modulus for 3D printed polymer components can be quite different between static and dynamic loading conditions. It can be, thus, argued that converting strains to bending moments by use of static tests potentially introduces additional uncertainties.

ACKNOWLEDGEMENTS

The present investigation was funded by the Lloyds Register Foundation University Technology Center on Ship Design for Enhanced Environmental Performance.

REFERENCES

Bishop, R. E. D. and Price, W. (1979). *Hydroelasticity of ships*. Cambridge University Press.

Carne, T. G., Griffith, D. T., and Cassias, M. E. (2007). Support Conditions for Free Boundary-Condition Modal Testing. *IMAC-XXV: A Conference & Exposition on Structural Dynamics*, (January 2015).

Chen, R.-Z., Du, S.-X., Wu, Y.-S., Lin, J.-R., Hu, J.-J., and Yue, Y.-L. (2001). Experiment on extreme wave loads of a flexible ship model. In *Practical Design of Ships and Other Floating Structures. Proceedings of the Eighth International Symposium on Practical Design of Ships and Other Floating Structures*, volume 2, pages 871–878.

Dessi, D. and Mariani, R. (2008). Analysis and Prediction of Slamming-Induced Loads of a High-Speed Monohull in Regular Waves. *Journal of Ship Research*, 52(1):71–86.

Grammatikopoulos, A., Banks, J., and Temarel, P. (2018). Experimental dynamic properties of ABS cellular beams produced using additive manufacturing. In *ECCM18 - 18th European Conference on Composite Materials*, Athens, Greece.

Hirdaris, S. E., Price, G. W., and Temarel, P. (2003). Two- and three-dimensional hydroelastic modelling of a bulker in regular waves. *Marine Structures*, 16(8):627–658.

Kim, B. W., Kim, K.-H., Kim, Y. S., and Hong, S. Y. (2014). Torsion Moment Conversion Methods in Model Test With U-shape Backbone. 3:782–791.

Kim, J. H., Kim, Y., Yuck, R. H., and Lee, D. Y. (2015). Comparison of slamming and whipping loads by fully coupled hydroelastic analysis and experimental measurement. *Journal of Fluids and Structures*, 52:145–165.

Lakshmynarayanana, P., Temarel, P., and Chen, Z. (2015). Hydroelastic analysis of flexible barge in regular waves using coupled CFD-FEM modelling. *Marstruct-2015*, pages 95–103.

Lavroff, J., Davis, M. R., Holloway, D. S., and Thomas, G. A. (2007). The Whipping Vibratory Response of a Hydroelastic Segmented Catamaran Model. In *Ninth International Conference on Fast Sea Transportation*, Shanhai, China.

Peng, S., Temarel, P., Bennett, S. S., Wu, W., Liu, Z., and Wang, Y. (2014). Symmetric response of a hydroelastic scaled container ship in regular and irregular waves. In *Proceedings of the ASME 2014 33rd International Conference on Ocean, Offshore and Arctic Engineering OMAE2014*, pages 1–10, San Francisco, California, USA. ASME.

Roark, R. J., Young, W. C., and Plunkett, R. (1976). *Formulas for Stress and Strain*, volume 43.

Watanabe, I., Ueno, M., and Sawada, H. (1989). Effects of Bow Flare Shape to the Wave Loads of a container ship. *Journal of the Society of Naval Architects of Japan*, 1989(166):259–266.

Wu, Y.-S., Chen, R.-Z., and Lin, J.-R. (2003). Experimental technique of hydroelastic ship model. In *Proceedings of the Third International Conference on Hydroelasticity, Oxford, UK, September*, pages 15–17.

Zhu, S., Wu, M., and Moan, T. (2011). Experimental investigation of hull girder vibrations of a flexible backbone model in bending and torsion. *Applied Ocean Research*, 33(4):252–274.